

# Optimal Design Operation Strategies of a Hyperloop Transportation System

Présentée le 18 janvier 2023

Faculté des sciences et techniques de l'ingénieur  
Laboratoire des systèmes électriques distribués  
Programme doctoral en génie électrique

pour l'obtention du grade de Docteur ès Sciences

par

**Denis TUDOR**

Acceptée sur proposition du jury

Prof. F. Rachidi-Haeri, président du jury  
Prof. M. Paolone, directeur de thèse  
Prof. L. Vanfretti, rapporteur  
Prof. F. Foiadelli, rapporteuse  
Prof. A. Rufer, rapporteur



Our virtues and our failings are inseparable,  
like force and matter.  
When they separate,  
man is no more.  
— Nikola Tesla

To my parents, Lakme and Eugen...



# Acknowledgements

First of all, I would like to thank Mario, my close friend and my Ph.D. supervisor, for helping me grow as a person, for offering me an unique opportunity and for always being present, especially in the delicate moments. Mario is not just a reference for my research—keeping both knowledge and critical thinking in mind—but he has always been a person who encouraged and challenged me to improve and grow. Grazie, Mario! I also want to thank Cyril for his invaluable technical inputs, for his kindness and for his unconditional trust. Then, I want to thank André for his challenging approach and for his involvement since the beginning. Farhad, thank you for the great and inspiring discussions and for your kindness. Rachid, thank you for your kindness and humor!

I would like to then thank and recognize the great work that Swissmetro has accomplished in the past. Without you, the history of hyperloop would have been different. I also want to thank the entire EPFLoop team that we created with Mario and André in 2017, and especially to Nicolas, Antoine and Armin. I also want to thank my former colleagues at rLoop, Richard and Brent, for the unique moments. Then, I want to thank SpaceX for re-launching the hyperloop concept through the competition and for letting me participate in the 4 out of 5 editions of the competition, from 2015 to 2018.

I also want to thank all my DESL-EPFL colleagues that I have had since 2017. I must admit that I was privileged to have such passionate and curious colleagues. Being a student is the best of jobs! However, I want to especially thank Sherif, Vladimir, Guglielmo, Emil, Asja, Quanxin, Varad and Amir.

I thank the Swisspod team for being unconditionally supportive in every moment. I want to especially thank Michael, Vlad, Dario, Gila, Marc, Teodor, Robert K., Samet, Dmitry, Flo, Jaime, Giovanni, Leo, Soner, Stefan, Robert G. Thank you, everyone! Thank you for your unique energy, spirit, resiliency and passion!

I also thank my best friends who may not be that many, but they have been relevant throughout my journey. Luca, Ioana, Codruț, thank you for your advice and for always being supportive with all my initiatives. Thank you for making me open my mind, for letting me feel comfortable with who I am and for all the moments in Barcelona or elsewhere that cannot be written here. Thank you for your resiliency. Thank you for your appreciation and for your true and unconditional friendship. Razvan, Liviu, Radu, thank you for the same. Razvan, I will

never forget the moment in front of the rail station. Purdila, I know that lately we haven't interacted as much as we would have liked, but you know how much I miss our (sometimes) nonsensical but mostly full of substance conversations. Thank you for all your help, your true and unconditional friendship and, most importantly, all the unspeakable moments. I also want to thank Dragoş for all his emotional support, for encouraging me to apply to EPFL and for the moments we spent together in California. Then, I thank Marius for helping me to accommodate here and for always being full of energy. Alexis, thank you for your integrity. Emilia, Bogdan, thank you for your humbleness and neutrality. Thank you for all the funny moments and for welcoming us to your home. Radu, I remember when you came and said "hi" in College Station. I knew that I had gained a reliable new friend. Carmelita, Ioan, thank you for your strategic advice, for your welcoming and for your unconditional support.

I would like to especially thank Ioana for the unconditional support and for dealing with my goofy and moody side. Thank you for always being constructive and for your resiliency. Thank you for being unique.

Last, but not least, I want to thank my parents, Lakme and Eugen, and my grandmother, Nenica. Thank you for making my education a priority in your life. Thank you for always encouraging me and thank you for helping me realize that the sky is the limit. Thank you for the entire context!

*Lausanne, Switzerland, 13th of October, 2022*

D. T.

# Abstract

In the last decades, transportation demand growth has played a major role in the increase of global  $CO_2$  footprint. At the same time, a number of countries have scheduled measurable and substantial cutback of  $CO_2$  emissions by 2050. As the transportation sector has a significant carbon footprint, this process has triggered the need to develop new transportation alternatives. These can be split in two main categories: *low-speed* and *high-speed* transportation systems. While there are current sustainable alternatives for low-speed (or medium-speed) transportation systems (i.e., electric vehicles, electric trains, ships), the only high-speed transportation system that exists at this moment is aviation. In terms of  $CO_2$ , the emissions produced by the aviation sector are significant and, even though there are alternatives to aircrafts powered by fossil fuels (i.e., hydrogen), they are technologically in their infancy.

Hyperloop could potentially represent a freight or passenger alternative to existing aviation especially for intra-continental travels. It comprises a network of capsules traveling at subsonic speed in a low-pressure constrained environment (i.e., a tube) embedding a set of rails for propulsion, levitation (or suspension) and guidance. The main advantages of a Hyperloop system are the energy efficiency and the sustainability gains caused by the large reduction of the drag aerodynamic losses and the electric drivetrain.

One of the major challenges is the construction of a new infrastructure with its extensive phases comprising feasibility studies, land expropriations, permits and civil constructions. Regarding the capsule design, the main technical challenge is conceiving and developing a solution that would eventually reduce the price of the infrastructure and leverage low-maintenance procedures. A major role here is played by the drivetrain system (i.e., propulsion, levitation and battery energy storage system) and its constrained operation in a low-pressure environment.

Within this context, the thesis focuses on the development of various optimization frameworks to enhance the performance of the Hyperloop capsules propulsion with respect to its kinetics and link the capsules propulsion to its operations in the depressurized environment. Then, the thesis discusses how to optimally scale-down the hyperloop system in order to design reduced-scale mockups to be used in a fast-prototyping process of this new transportation system. The last part of the thesis illustrates an experimental testing facility in the EPFL campus.

More specifically, the thesis is split in 3 different main parts.

In the first part, it is proposed an optimal sizing method that answers the question whether the energy and power requirements of the Hyperloop propulsion system are compatible with available power-electronics and battery technologies. By knowing the payload and the trajectory, the proposed sizing method minimizes the total number of battery cells that supply the capsule's propulsion and maximizes its performance. The first part ends with the assessment of the equivalent circuit battery models influence on the optimal design of the propulsion system of an energy-autonomous Hyperloop capsule. Although the proposed optimization problem is non-convex due to the adopted discrete-time formulation, its constraints exhibit a good numerical tractability and are used to address the above research question with a positive reply.

In the second part, an operational-driven optimal-design framework of a Hyperloop system is presented. The novelty of the proposed framework is the problem formulation that links the operations of a network of Hyperloop capsules, the model of the Hyperloop infrastructure, and the model of the capsule's propulsion and kinematics. The objective function of the optimization is to minimize the global energy consumption sourcing from the energy-autonomous capsules network and the depressurization procedures.

The third part presents an optimal assessment of the scaling factor process to be used for the development of a reduced-scale Hyperloop model, starting from the knowledge of the technical characteristics of its full-scale counterpart. The objective of the framework is to minimize the difference between the normalized power profiles corresponding to the reduced-scale and full-scale models of a hyperloop capsule traveling along a pre-defined trajectory with a pre-determined speed profile. By making reference to the full-scale model, a set of equations is proposed in order to obtain the reduced-scale model of a hyperloop system. The obtained reduced-scale model could eventually be used to build fast prototypes of various components to study the critical phenomena of such a peculiar mode of transportation without the need of complex and expensive full-scale setups.

Furthermore, the last chapter of the thesis illustrates the application of the proposed scale-down process to design a reduced-scale hyperloop experiment under construction on the EPFL Lausanne campus.

Key words: hyperloop, transportation, mobility, high-speed, sustainability, energy efficiency, tube, tunnel, low-pressure environment, depressurization, optimization, operation, aerodynamics, levitation, electric sub-systems, propulsion, energy reservoir, battery energy storage system, drive-train, full-scale model, reduced-scale model, mockup, energy-autonomous vehicles, operational-driven design.



# Résumé

Au cours des dernières décennies, la croissance de la demande du secteur des transports a joué un rôle majeur dans l'augmentation de l'empreinte carbone mondiale. Dans le même temps, un certain nombre de pays ont prévu une réduction mesurable et substantielle des émissions de  $CO_2$  d'ici 2050. Le secteur des transports ayant une empreinte carbone importante, ce processus a déclenché la nécessité de développer de nouvelles alternatives de transport. Ceux-ci peuvent être divisés en deux catégories principales : les systèmes de transport à *basse vitesse* et à *grande vitesse*. Bien qu'il existe actuellement des alternatives durables pour les systèmes de transport à basse vitesse (ou à vitesse moyenne) (i.e., les véhicules électriques, les trains électriques, les navires), le seul système de transport à grande vitesse qui existe actuellement est l'aviation. En termes de  $CO_2$ , les émissions produites par le secteur de l'aviation sont importantes et, même s'il existe des alternatives aux avions propulsés par des carburants fossiles (i.e., l'hydrogène), ils en sont technologiquement à leurs balbutiements.

Hyperloop pourrait potentiellement représenter une alternative au transport de fret ou de passagers à l'aviation existante, en particulier pour les voyages intra-continentaux. Il comprend un réseau de capsules se déplaçant à une vitesse subsonique dans un environnement contraint à basse pression (i.e., un tube) intégrant un ensemble de rails pour la propulsion, la lévitation (ou la suspension) et le guidage. Les principaux avantages d'un système Hyperloop sont l'efficacité énergétique et les gains de durabilité causés par la forte réduction des pertes aérodynamiques et la propulsion électrique.

L'un des défis majeurs est la construction d'une nouvelle infrastructure avec ses phases étendues comprenant des études de faisabilité, des expropriations foncières, des permis de construire et le génie civil. En ce qui concerne la conception de la capsule, le principal défi technique consiste à concevoir et développer une solution qui permettrait de réduire le prix de l'infrastructure et de tirer parti des procédures à faible maintenance. Un rôle majeur ici est joué par le système de propulsion (i.e., la propulsion, la lévitation et le système de stockage d'énergie de la batterie) et son fonctionnement contraint dans un environnement à basse pression.

Dans ce contexte, cette thèse porte sur le développement de différents cadres d'optimisation pour améliorer les performances de la propulsion des capsules Hyperloop par rapport à sa cinématique et lier la propulsion des capsules à ses opérations dans l'environnement dépressurisé. Ensuite, la thèse examine comment réduire de manière optimale le système

hyperloop afin de concevoir des maquettes à échelle réduite à utiliser dans un processus de prototypage rapide de ce nouveau système de transport. La dernière partie de la thèse illustre une installation de test expérimentale sur le campus de l'EPFL.

Plus précisément, la thèse est divisée en 3 parties principales différentes.

Dans la première partie, il est proposé une méthode de dimensionnement optimal qui répond à la question de savoir si les besoins en énergie et en puissance du système de propulsion Hyperloop sont compatibles avec les technologies d'électronique de puissance et de batterie disponibles. En connaissant la charge utile et la trajectoire, la méthode de dimensionnement proposée minimise le nombre total de cellules de batterie qui alimentent la propulsion de la capsule et maximise ses performances. La première partie se termine par l'évaluation de l'influence des modèles de batterie à circuit équivalent sur la conception optimale du système de propulsion d'une capsule Hyperloop autonome en énergie. Bien que le problème d'optimisation proposé soit non convexe en raison de la formulation en temps discret adoptée, ses contraintes présentent une bonne traçabilité numérique et sont utilisées pour répondre à la question de recherche ci-dessus.

Dans la deuxième partie, un cadre de conception optimale axé sur les opérations d'un système Hyperloop est présenté. La nouveauté du cadre proposé est la formulation du problème qui relie les opérations d'un réseau de capsules Hyperloop, le modèle de l'infrastructure Hyperloop et le modèle de la propulsion et de la cinématique de la capsule. La fonction objectif de l'optimisation est de minimiser la consommation globale d'énergie provenant du réseau de capsules autonomes en énergie et des procédures de dépressurisation.

La troisième partie présente une évaluation optimale du processus de facteur d'échelle à utiliser pour le développement d'un modèle Hyperloop à échelle réduite, à partir de la connaissance des caractéristiques techniques de son homologue à grande échelle. L'objectif du cadre est de minimiser la différence entre les profils de puissance normalisés correspondant aux modèles à échelle réduite et à échelle réelle d'une capsule hyperloop se déplaçant le long d'une trajectoire prédéfinie avec un profil de vitesse prédéterminé. En faisant référence au modèle grandeur nature, un ensemble d'équations est proposé afin d'obtenir le modèle à échelle réduite d'un système hyperloop. Le modèle à échelle réduite obtenu pourrait éventuellement être utilisé pour construire rapidement des prototypes de divers composants afin d'étudier les phénomènes critiques d'un tel mode de transport spécifique sans avoir besoin de configurations complexes et coûteuses à grande échelle.

De plus, le dernier chapitre de la thèse illustre l'application du processus de réduction d'échelle proposé à la conception d'une infrastructure de test à échelle réduite sur le campus de l'EPFL à Lausanne.

Mots clefs : hyperloop, transport, mobilité, haut débit, durabilité, efficacité énergétique, tube, tunnel, environnement basse pression, dépressurisation, optimisation, exploitation, aérodynamique, lévitation, sous-systèmes électriques, propulsion, réservoir d'énergie, système de stockage d'énergie par batterie, propulsion électrique, modèle grandeur nature, modèle réduit, maquette, véhicules autonomes en énergie, conception axée sur l'exploitation.

# Contents

<b>Acknowledgements</b>	<b>i</b>
<b>Abstract (English/Français/Deutsch)</b>	<b>iii</b>
<b>List of figures</b>	<b>xi</b>
<b>List of tables</b>	<b>xv</b>
<b>1 Introduction</b>	<b>1</b>
1.1 Context and Motivation . . . . .	1
1.2 Thesis Outline . . . . .	3
1.3 Contributions . . . . .	3
<b>2 Optimal Design of the Propulsion System of a Hyperloop Capsule</b>	<b>7</b>
2.1 Introduction and Literature Review . . . . .	7
2.2 Hypotheses and problem statement . . . . .	9
2.2.1 Trajectory . . . . .	9
2.2.2 The Model of the Capsule Propulsion System . . . . .	11
2.2.3 Capsule Kinematic Model . . . . .	13
2.2.4 Formulation of the Optimization Problem . . . . .	15
2.3 Numerical results . . . . .	18
2.3.1 Assumptions on the Capsule Trajectory . . . . .	18
2.3.2 Assumptions on the Capsule and PS . . . . .	19
2.3.3 Results . . . . .	21
2.3.4 General Observations . . . . .	26
2.3.5 Dominant Solutions . . . . .	29
2.3.6 Sensitivity Analysis . . . . .	29
2.4 Extension with a different battery cell model . . . . .	30
2.4.1 Introduction . . . . .	30
2.4.2 Cell Models and Formulation of the Optimization Problems . . . . .	31
2.4.3 Numerical Assumptions and Results . . . . .	33
2.4.4 Discussions . . . . .	36
2.5 Conclusions . . . . .	38
	vii

<b>3</b>	<b>Operational-Driven Optimal-Design of a Hyperloop System</b>	<b>39</b>
3.1	Introduction and Literature Review . . . . .	39
3.2	Hypotheses and Models . . . . .	41
3.2.1	Model of the Hyperloop Infrastructure . . . . .	41
3.2.2	Model of the Hyperloop Capsule . . . . .	44
3.2.3	Accounting for the Kantrowitz Limit to determine the upper-bound of capsules' speed . . . . .	48
3.2.4	Hyperloop Infrastructure Operation . . . . .	48
3.3	Formulation of the Optimization Problem . . . . .	49
3.4	Numerical Assumptions . . . . .	52
3.4.1	Infrastructure Assumptions . . . . .	53
3.4.2	Capsule Assumptions . . . . .	53
3.4.3	Assumptions for the computation of the Kantrowitz Limit and associated capsules' maximum speed . . . . .	55
3.4.4	Hyperloop Infrastructure Operational Assumptions . . . . .	56
3.5	Results . . . . .	57
3.5.1	Main Numerical Assumptions . . . . .	57
3.5.2	General Observations . . . . .	57
3.5.3	Pressure vs. Masses . . . . .	61
3.5.4	Profiles of Speed, Travel Time, BESS SoC and Power . . . . .	61
3.5.5	Energy Needs and Infrastructure Operation . . . . .	64
3.5.6	Impact of the Levitation Drag . . . . .	64
3.5.7	Sensitivity Analysis . . . . .	67
3.5.8	Use of Compressor . . . . .	80
3.6	Conclusions . . . . .	82
<b>4</b>	<b>Design of a Hyperloop System MockUp</b>	<b>85</b>
4.1	Introduction and Literature Review . . . . .	85
4.2	Full-Scale Hyperloop System . . . . .	87
4.2.1	Hyperloop General Characteristics . . . . .	87
4.2.2	Aerodynamic Limitations of the Hyperloop System . . . . .	87
4.2.3	Model of the Capsule's Propulsion System . . . . .	89
4.3	Reduced-Scale Model of a Hyperloop System . . . . .	90
4.3.1	Scaling of the Capsule's Kinematic Model, Masses, Power Profiles, and Environment . . . . .	91
4.3.2	Scaling of the Capsule's Aerodynamics and Drag Coefficient . . . . .	92
4.4	Optimal Assessment of the Scaling Factor . . . . .	93
4.5	Application Example . . . . .	95
4.5.1	Full-Scale Model Assumptions . . . . .	95
4.5.2	Reduced-Scale Model Assumptions . . . . .	97
4.5.3	Results . . . . .	98
4.6	Conclusions . . . . .	103

---

<b>5</b>	<b>A Reduced-Scale Hyperloop Experiment</b>	<b>105</b>
5.1	Introduction . . . . .	105
5.2	Objectives . . . . .	107
5.3	Overview of the Reduced-Scale Hyperloop Infrastructure . . . . .	107
5.3.1	Tube Geometry and Characteristics . . . . .	107
5.3.2	Rail Geometry . . . . .	108
5.3.3	Sensing, Control and Telecommunication . . . . .	109
5.3.4	Depressurization System . . . . .	110
5.4	Characteristics of the Capsule Mockup . . . . .	110
5.4.1	General Characteristics of the Capsule . . . . .	111
5.4.2	Mechanical Components . . . . .	114
5.4.3	Propulsion System and Battery Energy Storage System . . . . .	115
5.5	First Experiment . . . . .	117
5.6	Conclusions . . . . .	117
<b>6</b>	<b>Conclusions</b>	<b>119</b>
	<b>Curriculum Vitae</b>	<b>133</b>



## List of Figures

2.1	The conceptual hyperloop diagram. . . . .	8
2.2	The generic trajectory of a hyperloop capsule. . . . .	10
2.3	Equivalent circuit of a cell adopted to derive the BESS constraints. . . . .	12
2.4	Behaviour of the problem objective for $L = 226\text{km}$ and $w = 100$ as a function of the initial values of $N_s N_{p,init}$ and $a_{init}$ . . . . .	22
2.5	Optimal-speed profile for $L = 226\text{km}$ , $w = 100$ , $a_{init} = 0.6 \frac{m}{s^2}$ , $N_s N_{p,init} = 2000\text{cells}$ . 23	
2.6	Optimal traction-power profile for $L = 226\text{km}$ , $w = 100$ , $a_{init} = 0.6 \frac{m}{s^2}$ , $N_s N_{p,init} = 2000\text{cells}$ . . . . .	23
2.7	Optimal cell-current profile for $L = 226\text{km}$ , $w = 100$ , $a_{init} = 0.6 \frac{m}{s^2}$ , $N_s N_{p,init} = 2000\text{cells}$ . . . . .	24
2.8	Total number of cells of the BESS. . . . .	25
2.9	Capsule and BESS masses. . . . .	25
2.10	Maximum speed along the trajectory. . . . .	25
2.11	Maximum acceleration along the trajectory (values in per-unit to $g$ ). . . . .	25
2.12	Maximum traction power provided by the capsule PS along the trajectory. . . . .	25
2.13	BESS SoC at the end of the trajectory. . . . .	25
2.14	Average time necessary to cover the trajectory. . . . .	26
2.15	The energy consumption per passenger per km. . . . .	26
2.16	Number of cells sensitivity analysis (for $w = 100$ ). . . . .	30
2.17	Trajectory traveling time sensitivity analysis (for $w = 100$ ). . . . .	31
2.18	Cell Model 2: second equivalent circuit of a cell used to derive the BESS constraints (in general, the TTC model can contain multiple RC series branches in order to improve its capability to model the charge diffusion). . . . .	32
2.19	Cell Model 2: second equivalent circuit of a cell adopted to derive the BESS constraints. . . . .	33
2.20	Capsule and BESS masses. . . . .	35
2.21	Maximum speed along the trajectory. . . . .	35
2.22	Maximum acceleration along the trajectory (values in per-unit to $g$ ). . . . .	35
2.23	Maximum traction power provided by the capsule propulsion system. . . . .	35
2.24	Time necessary to cover the trajectory. . . . .	35
2.25	The energy consumption per passenger per km. . . . .	36
2.26	BESS relative difference depending on the battery cell model. . . . .	37

3.1	Schematic view of the hyperloop infrastructure's depressurization system. . . .	42
3.2	Simplified geometry of the hyperloop tube (side view). . . . .	42
3.3	The generic trajectory of hyperloop capsules. Adapted from Fig.2.2 . . . . .	45
3.4	Operational scheme for the hyperloop infrastructure. . . . .	49
3.5	$C_d$ dependency with the Mach number, $Ma$ , adapted from [63]. . . . .	54
3.6	Assessment of the choked flow regime of the fluid around the hyperloop capsule. . . . .	56
3.7	Dependency of the optimal operational internal pressure of the tube, $p_{tube}$ , with $T_{depr}$ . . . . .	59
3.8	Dependency of the tube depressurization energy, $E_{depr}$ , with $T_{depr}$ . . . . .	59
3.9	Dependency of the air leaks compensation energy, $E_{pr}$ , with $T_{depr}$ . . . . .	60
3.10	Dependency of capsules network energy, $E_{caps}$ , with $T_{depr}$ . . . . .	60
3.11	Dependency of the capsule's BESS maximum power, $max(P_{BESS})$ , with $T_{depr}$ . . . . .	60
3.12	Dependency of capsule's maximum (or cruising) speed, $max(v)$ , with $T_{depr}$ . . . . .	60
3.13	The dependency of the masses ( $m$ , $m_{BESS}$ , $m_{PS}$ ) with $p_{tube}$ for every $L$ . . . . .	61
3.14	Capsule speed along its position for each $T_{depr}$ (profiles refers to $L = 226km$ ). . . . .	63
3.15	Capsule traveling time, $t_{Lk}$ , along its position for each $T_{depr}$ (profiles refers to $L = 226km$ ). . . . .	63
3.16	Capsule BESS SoC along its position for each $T_{depr}$ (profiles refers to $L = 226km$ ). . . . .	63
3.17	Capsule $P_{batt}$ along its position for each $T_{depr}$ (profiles refers to $L = 226km$ ). . . . .	63
3.18	Total energy need per number of passengers and per km, $E_r$ , as a function of $T_{depr}$ for each trajectory length. . . . .	64
3.19	$C_{lev}$ dependency with the speed of the capsule, $v$ , adapted from [74]. . . . .	65
3.20	Infrastructure $p_{tube}$ for each $T_{depr}$ (profiles refers to $L = 226km$ ) including the losses of the passive levitation. . . . .	66
3.21	Capsule $P_{batt}$ along its position for each $T_{depr}$ (profiles refers to $L = 226km$ ) including the losses of the passive levitation. . . . .	66
3.22	Speed $v$ along its position for each $T_{depr}$ (profiles refers to $L = 226km$ ) including the losses of the passive levitation. . . . .	66
3.23	The dependency of masses ( $m$ , $m_{BESS}$ , $m_{PS}$ ) with $p_{tube}$ for $L = 226km$ including the losses of the passive levitation. . . . .	66
3.24	Dependency of the optimal operational internal pressure of the tube, $p_{tube}$ , with $T_{depr}$ ( $r_{caps}$ sensitivity analysis). . . . .	69
3.25	Dependency of the tube depressurization energy, $E_{depr}$ , with $T_{depr}$ ( $r_{caps}$ sensitivity analysis). . . . .	69
3.26	Dependency of the air leaks compensation energy, $E_{pr}$ , with $T_{depr}$ ( $r_{caps}$ sensitivity analysis). . . . .	69
3.27	Dependency of capsules network energy, $E_{caps}$ , with $T_{depr}$ ( $r_{caps}$ sensitivity analysis). . . . .	69
3.28	Total energy need per number of passengers and per km, $E_r$ , as a function of $T_{depr}$ for each trajectory length ( $r_{caps}$ sensitivity analysis). . . . .	70
3.29	$C_d$ dependency with the Mach number, $Ma$ ( $C_d$ sensitivity analysis). . . . .	71



3.30	Dependency of the optimal operational internal pressure of the tube, $p_{tube}$ , with $T_{depr}$ ( $C_d$ sensitivity analysis).	71
3.31	Dependency of capsules network energy, $E_{caps}$ , with $T_{depr}$ ( $C_d$ sensitivity analysis).	71
3.32	Dependency of the tube depressurization energy, $E_{depr}$ , with $T_{depr}$ ( $C_d$ sensitivity analysis).	71
3.33	Dependency of the air leaks compensation energy, $E_{pr}$ , with $T_{depr}$ ( $C_d$ sensitivity analysis).	72
3.34	Total energy need per number of passengers and per km, $E_r$ , as a function of $T_{depr}$ for each trajectory length ( $C_d$ sensitivity analysis).	72
3.35	Dependency of the optimal operational internal pressure of the tube, $p_{tube}$ , with $T_{depr}$ ( $k_{perm}$ sensitivity analysis).	73
3.36	Dependency of the tube depressurization energy, $E_{depr}$ , with $T_{depr}$ ( $k_{perm}$ sensitivity analysis).	73
3.37	Dependency of the air leaks compensation energy, $E_{pr}$ , with $T_{depr}$ ( $k_{perm}$ sensitivity analysis).	74
3.38	Dependency of capsules network energy, $E_{caps}$ , with $T_{depr}$ ( $k_{perm}$ sensitivity analysis).	74
3.39	Total energy need per number of passengers and per km, $E_r$ , as a function of $T_{depr}$ for each trajectory length ( $k_{perm}$ sensitivity analysis).	74
3.40	Dependency of the optimal operational internal pressure of the tube, $p_{tube}$ , with $T_{depr}$ ( $m_0$ sensitivity analysis).	75
3.41	Dependency of capsules network energy, $E_{caps}$ , with $T_{depr}$ ( $m_0$ sensitivity analysis).	76
3.42	Dependency of the tube depressurization energy, $E_{depr}$ , with $T_{depr}$ ( $m_0$ sensitivity analysis).	76
3.43	Dependency of the air leaks compensation energy, $E_{pr}$ , with $T_{depr}$ ( $m_0$ sensitivity analysis).	76
3.44	Total energy need per number of passengers and per km, $E_r$ , as a function of $T_{depr}$ for each trajectory length ( $m_0$ sensitivity analysis).	76
3.45	Dependency of the LIM's efficiency, $\eta_{LIM}$ , with the speed of the capsule, $v$ .	77
3.46	Dependency of the VSI's power factor, $\cos(\phi)$ , with the speed of the capsule, $v$ .	78
3.47	Dependency of the optimal operational internal pressure of the tube, $p_{tube}$ , with $T_{depr}$ (propulsion sensitivity analysis).	79
3.48	Dependency of capsules network energy, $E_{caps}$ , with $T_{depr}$ (propulsion sensitivity analysis).	79
3.49	Dependency of the tube depressurization energy, $E_{depr}$ , with $T_{depr}$ (propulsion sensitivity analysis).	79
3.50	Dependency of the air leaks compensation energy, $E_{pr}$ , with $T_{depr}$ (propulsion sensitivity analysis).	79
3.51	Total energy need per number of passengers and per km, $E_r$ , as a function of $T_{depr}$ for each trajectory length (propulsion sensitivity analysis).	80

3.52 Gabrielli-Kármán diagram showing the comparison of hyperloop with electrical vehicles and electrical trains . . . . .	83
4.1 Schematic 2D representation of a hyperloop capsule traveling in a tube. . . . .	88
4.2 FS hyperloop model acceleration profile as a function of time, $a_{fs}(i)$ , adapted from Chapter 3 for a hyperloop trajectory length $L_{fs} = 500km$ . . . . .	96
4.3 FS hyperloop model speed profile as a function of time, $v_{fs}(i)$ , adapted from Chapter 3 for a hyperloop trajectory length $L_{fs} = 500km$ . . . . .	97
4.4 FS hyperloop model traction and BESS power profiles as functions of time, $P_{tr}^{fs}(i)$ and $P_{batt}^{fs}(i)$ . . . . .	97
4.5 Aeroshell model . . . . .	98
4.6 Interpolated values of $C_D^{rs}(k, \frac{v_{fs}^{max}}{k})$ for various values of the scaling factor, $k$ . . . . .	99
4.7 Values of the objective function of the problem (4.15) for various values of the scaling factor, $k$ . . . . .	99
4.8 Normalized power profiles as functions of time of both FS and RS hyperloop models for the considered values of the scaling factor $k$ . . . . .	100
4.9 The cross sections of the RS model, $S_{rs}^{capsule}$ , function of the scale factor, $k$ . . . . .	101
4.10 The lengths of trajectory, $L_{rs}$ , function of the scale factor, $k$ . . . . .	101
4.11 Speed profiles as functions of time of the hyperloop RS model for the various considered values of the scaling factor $k$ . . . . .	101
4.12 Acceleration profiles as functions of time of the hyperloop RS model for the various considered values of the scaling factor $k$ . . . . .	102
4.13 Power profiles as functions of time of the hyperloop RS model for the various considered values of the scaling factor $k$ . . . . .	102
5.1 Overview of the EPFL RS hyperloop test infrastructure. . . . .	108
5.2 Ribs of the tube of the EPFL RS hyperloop test infrastructure . . . . .	108
5.3 The rail design of the EPFL RS hyperloop test infrastructure. . . . .	109
5.4 Sensing, control and telecommunication flowchart of the RS infrastructure. . . . .	111
5.5 One pump connected to the RS infrastructure. . . . .	112
5.6 The block scheme of the RS capsule PS and its kinematics. . . . .	112
5.7 The RS capsule design. . . . .	113
5.8 The RS capsule design. . . . .	113
5.9 The inclination of the RS capsule. . . . .	114
5.10 The the mechanical fit check overview of the RS infrastructure and RS capsule design. . . . .	116
5.11 LIM position in the RS capsule. . . . .	116
5.12 Acceleration and thrust profiles of the RS capsule. . . . .	117

## List of Tables

3.1	Variables' information. . . . .	57
3.2	Initialization of the control variables. . . . .	58
4.1	CFD-determined values of $C_D^{rs}(k, \frac{v_{max}^{fs}}{k})$ . . . . .	98
4.2	RS mass values, $m_{rs}$ function of $k$ . . . . .	100
5.1	Mass distribution of $m_{rs}^{exp}$ . . . . .	114
5.2	Lengths of the various subsystems of the RS capsule. . . . .	115
5.3	Dimensions of the various subsystems in the pressure vessel. . . . .	115



# 1 Introduction

## 1.1 Context and Motivation

According to the European Environment Agency [1], in 2017 and 2018, approximately 27% of total EU-28 greenhouse gas emissions came from the transportation sector including the maritime, aviation, railroad and railway sectors. However, according to the same report and with respect to the EU's strategy 2050, emissions need to fall by 66% as stated in [2]. It is worth mentioning that the largest percentage increase in greenhouse gas emissions is given by the aviation sector. Therefore, as the transportation demand has been growing, hyperloop can represent a viable alternative transportation solution for intra-continental aviation and it can serve both for freight and passengers needs.

Historically, most transportation systems were designed considering different boundary conditions and deployment scenarios. The definition of the characteristics of the energy reservoir that a given transportation system uses is particularly important, because this element determines whether the carrier of the system is energy-autonomous or not. For instance, electric trains (ETs) and electric vehicles (EVs), even if sharing similar propulsion systems (PSs), exploit energy reservoirs with very different characteristics. ETs rely on the quasi-infinite energy reservoir of power grids that, compared to the usual power required by the train propulsion systems, can be considered as a quasi-infinite source of power. Conversely, EVs rely on energy reservoirs (i.e., battery energy storage systems - BESS) characterized by limited gravimetric and volumetric energy and power densities. Hence, the design of these two transportation systems is radically different. Indeed, for ETs the energy reservoir does not translate into physical constraints that, on the contrary, need to be well stated for the design of an EV in order to maximize its travel distance [3].

It is also worth noting that, compared to other transportation systems directly supplied by fossil fuels, ETs and EVs represent the best solution for intra-continental travel in terms of average energy usage per passenger per km, as well as for the  $CO_2$  emissions per passenger per km [4], [5] (EV:  $97 \frac{Wh}{passenger \cdot km}$  [6],  $45 \frac{gCO_2}{passenger \cdot km}$  [7]; ET:  $180 \frac{Wh}{passenger \cdot km}$  [8],  $20 \frac{gCO_2}{passenger \cdot km}$  [9]). The two aforementioned transportation systems merge their characteristics when translated into

the hyperloop concept. The hyperloop transportation system is composed of a constrained space characterized by a low-pressure environment (operated, in general, below  $100\text{ mbars}$ ), that is usually represented by tubes that also house a dedicated rail system responsible for the mechanical constraining of energy-autonomous vehicles, henceforth called capsules, carrying a given payload. Capsules should be self-propelled and can use the tube's rail for guidance, magnetic levitation and propulsion purposes. For an average speed way larger than one of EVs or ETs and a maximum speed in the order of the speed of sound, the hyperloop is expected to achieve average energy consumption in the range of:  $30\text{-}90 \frac{\text{Wh}}{\text{passenger}\cdot\text{km}}$  [10]. In view of the above, the hyperloop potentially presents the same advantages of ETs (high speed, low energy-consumption and  $\text{CO}_2$  emissions per passenger per km) while being at the same time an energy-autonomous system such as an EV.

Therefore, with respect to the above-stated elements, this Thesis answers to fundamental questions related to the design of a hyperloop transportation system such as: (i) are the current technologies on electric PS, power electronics and BESSs compatible with the energy and power needs of a hyperloop capsule? (ii) What is the optimal operating pressure inside of a hyperloop tube? (iii) What is an achievable total energy consumption of a hyperloop system? (iv) Is there a relevant dependency between the infrastructure operation and capsule's propulsion system design? (v) Which is the impact of a passive magnetic levitation system on the capsule's energy consumption? (vi) Can a front-compressor increase the energy efficiency of a hyperloop system? (vii) How does the Kantrowitz Limit affect the design of a hyperloop system? (viii) What is an optimal method to assess a reduced-scale factor of a hyperloop transportation system? (ix) Does this method create solutions that could be designed, manufactured and tested? (x) How does a reduced scale testing facility and a hyperloop capsule need designed such as they comply with theoretical models?

To reply to the above questions, the Thesis first presents an optimization framework to determine the main characteristics of the propulsion system of energy-autonomous hyperloop capsules considering two different cell models of the the BESS. Further, since the performance of the propulsion system of hyperloop capsules is related to the environmental and geometrical constraints of an enclosed space (i.e., tube or tunnel), an optimization framework that links these environmental conditions, operations, kinematics of the capsule and BESS size is proposed. It is worth mentioning that the full complexity of the subsystems is not entirely modelled since it was beyond the scope of this work. Finally, the Thesis presents a method to determine the scale-down process of a hyperloop system (with given full-scale characteristics) to be used for the design of suitable reduced-scale experiments, then, in accordance to the proposed scale-down process, an experimental facility under construction on the EPFL campus is described.

## 1.2 Thesis Outline

The Thesis is organized into six main chapters. The content of each chapter is summarized below.

Chapter 2 focuses on the assessment of the optimal design of the propulsion system of an energy-autonomous hyperloop capsule supplied by a BESS. Two models of the BESS are used and their influence on the design of the capsule propulsion system compared. The proposed framework quantitatively evaluates the energy and power requirements of the hyperloop propulsion system irrespectively of the geometry of the constrained environment (i.e., tube) and with a given operation pressure. In addition, a sensitivity analysis is conducted along with dominant solution analysis.

Chapter 3 proposes an operational-driven optimal-design framework of a hyperloop system. To fix ideas, this optimization framework is pursued in order to optimally link the operation of a network of hyperloop capsules, the model of the hyperloop infrastructure and its operational conditions, the model of the capsules PSs, BESSs and their kinematics. In addition, various sensitivity analyses have been carried out in order to determine how different parameters do influence the obtained solutions. The optimization problem is also adapted in the sensitivity analysis in order to consider a capsule passive levitation system (i.e., by adding a magnetic drag model).

Chapter 4 assesses the design of a reduced-scale hyperloop system. The purpose of this work is to develop a reduced scale hyperloop system to validate the findings of Chapter 3 and Chapter 2. With respect to this objective, a process for the optimal assessment of the scaling factor is presented, both for the infrastructure and capsule models. The objective function of this process is to minimize the difference between the normalized power profiles associated with the reduced-scale and full-scale models of a hyperloop capsule (i.e., using the results obtained in Chapter 3) traveling along a pre-defined trajectory and with a pre-determined speed profile.

Based on Chapter 4, Chapter 5 illustrates the characteristics of a reduced-scale hyperloop. The infrastructure is under construction on the Lausanne EPFL campus. An overview of the main characteristics at the system level infrastructure and capsule is given.

Chapter 6 contains a summary of the main outcomes of this Thesis.

## 1.3 Contributions

The original contributions of this Thesis are listed in the following.

- A model for the design of an energy-autonomous hyperloop capsule propulsion system integrated in a novel optimization framework is proposed. The results obtained by using this framework prove that the energy and power requirements of the hyperloop

propulsion system are compatible with the main characteristics of existing power electronics and battery technologies. The simulations show that, due to the low-pressure environment, hyperloop does not represent an energy-intensive application, but a power-intensive one. A quantitative comparison of the influence on the obtained results of different cell models is carried out, as well as various sensitivity analyses of different parameters on dominant solutions. To the best of the author's knowledge, such framework represents the first attempt towards the definition of the main characteristics of the propulsion system of a hyperloop capsule.

- A novel and more comprehensive optimization framework of a hyperloop system linking the operation of a network of hyperloop capsules, the model of the hyperloop infrastructure, and the model of the capsule's propulsion and kinematics is developed. This optimization framework answers to the following fundamental questions about the hyperloop system with respect to the minimization of its global energy consumption: (i) what is the optimal operating pressure inside a hyperloop tube? (ii) What is the achievable global energy consumption of a hyperloop system? (iii) Is there a strong dependency between the infrastructure operation and capsule's propulsion system design? (iv) Which is the impact of a passive magnetic levitation system on the energy consumption of the capsule? (v) Can a front-compressor increase the energy efficiency of a hyperloop system? (vi) How does the Kantrowitz Limit affect the design of a hyperloop system? Various sensitivity analysis are also carried out. To the best of the author's knowledge, such framework represents the first comprehensive attempt for the optimal definition of the main and complete model of a hyperloop system.
- A comparison of a hyperloop system with nowadays existing transportation systems through a Gabrielli-Kármán diagram is pursued. The diagram shows that compared to other electrical transportation modes, such as electrical vehicles and electrical trains, the obtained results have shown that hyperloop represents an energy-efficient and high-speed solution with very favorable values of energy need per-passenger-per-km vs. speed.
- A novel process to optimally assess the scale factor of a hyperloop system is proposed with the purpose of defining a reduced-scale hyperloop experiment. The objective of the process is the minimisation of the difference between the normalized energy consumption associated with the reduced-scale and full-scale models taking into account the constraints related to kinematics, BESS and PS, capsule's aerodynamics and the operating environmental conditions. A study of the scaled-down version of an application example is pursued.
- To the best of the author's knowledge, the proposed scale-down process has allowed to define the first reduced-scale hyperloop testing facility enabling experimental studies of long-distance trajectories of a hyperloop capsule in a low-pressure environment. The fast prototyping of various components and the study of critical phenomena that take place in this peculiar transportation system represent the main advantages of



initially using such a reduced-scale model, as it reduces the risk of building complex and expensive full-scale setups. The parameters of the experiments which are used in the actual experimental infrastructure are those derived from the results above-obtained through the assessment of the scaling factor in order to check the overall proposed hyperloop system model.



## 2 Optimal Design of the Propulsion System of a Hyperloop Capsule

©2019 IEEE

Reprinted, with permission, from: D. Tudor and M. Paolone, "Optimal Design of the Propulsion System of a hyperloop Capsule," in IEEE Transactions on Transportation Electrification, November 2019.

In this chapter, we focus on the assessment of the optimal design of the propulsion system of an energy-autonomous hyperloop capsule supplied by batteries. The novelty in this chapter is to propose a sizing method for this specific transportation system, and answer the question whether the energy and power requirements of the hyperloop propulsion are compatible with available power-electronics and battery technologies. By knowing the weight of a pre-determined payload to be transported along pre-determined trajectories, the proposed sizing method minimizes the total number of battery cells that supply the capsule's propulsion and maximizes its performance. The constraints embed numerically-tractable and discrete-time models of the main components of the electrical propulsion system and the battery, along with a kinematic model of the capsule. Although the optimization problem is non-convex due to the adopted discrete-time formulation, its constraints exhibit a good numerical tractability. After having determined multiple solutions, we identify the dominant ones by using specific metrics. These solutions identify propulsion systems characterized by energy reservoirs with an energy capacity in the order of 0.5 MWh and a power rating below 6.25 MW, and enable an energy consumption between 10-57.15 Wh/km/passenger depending on the length of the trajectory.

### 2.1 Introduction and Literature Review

To carry a payload of a few tons on a capsule travelling at a maximum speed higher than  $1000 \frac{km}{h}$ , along trajectories of hundreds of kilometers with an acceleration comparable with standard passenger air crafts, there are two fundamental questions that need to be addressed: (i) are today's batteries, power-electronic converters and electrical motors compatible with

the power and energy needs of this new transportation system? (ii) Are the hyperloop energy consumptions and emissions compatible with these expectations? In this chapter, we focus on providing quantitative replies to these two questions by proposing a specific optimal sizing framework.

Hyperloop capsules move between pre-determined point-to-point stations (Station A and Station B) and fixed trajectories in low-pressure tubes. As aforementioned, the pressure in hyperloop tubes is pumped down to values to the order of 50 mbar or below (i.e., [11]), a condition that reduces drag forces and increases efficiency and maximum achievable speed (see Fig. 2.1).

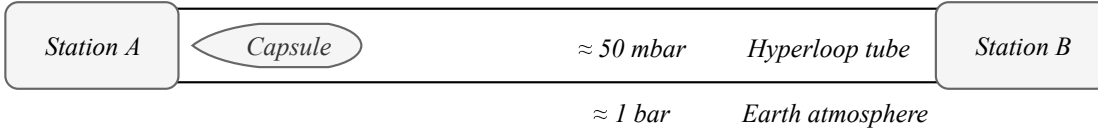


Figure 2.1: The conceptual hyperloop diagram.

This simple operational aspect substantially reduces the energy needs [12] of a hyperloop capsule yet increases its maximum achievable speed. Consequently, the PS of a hyperloop capsule can require a substantial amount of power (in the order of several MW per tens of tons of capsule mass [13]) to be extracted from an energy reservoir containing a relatively low amount of energy [5]. For this reason, the optimal sizing of the hyperloop capsule PS is a non-trivial problem, which is the core of this chapter.

The problem of the optimal sizing of energy-autonomous vehicles is studied in the existing literature, especially concerning EVs [3]. In [14], a modelling framework is proposed to study different aircraft-electric propulsion architectures by means of a platform that simulates power generation, distribution, and fuel consumption. Regarding the study of the behaviour of batteries in electric and hybrid vehicles, in [15], it is proposed a simulator specifically created in order to predict the state-of-charge (SoC) and dynamic behavior of different battery types. In [16], [17] and [18]–[21], optimization strategies and component sizing methods have been proposed to enhance the energy consumption of different energy autonomous vehicles. [19], [22]–[24] present optimization methods for electrical or hybrid vehicles; these methods especially involve BESSs.

However, none of the aforementioned papers focused on the specific problem of sizing the propulsion system of a hyperloop capsule. In this respect, the novelty of the chapter is set up by proving that, with current technologies on batteries, power electronics and electrical machines, an energy-autonomous hyperloop capsule is feasible, and more efficient in terms of energy consumption and  $CO_2$  emissions comparing with today's transportation systems.

By making use of numerically tractable models of electrical PSs and BESSs, we focus first on the formulation of a non-convex optimization problem that targets the optimal design of the PS of a hyperloop capsule. Our proposed optimization minimizes a bi-objective function where

the first term is represented by the total number of the BESS cells and the second term—the norm-2 of the discrete sampled accelerations along the capsule's trajectory. The constraints representing the capsule kinematic are also taken into account, as well as a regenerative braking of the PS. We provide a comprehensive analysis of the results for different weights of the terms in the objective function and identify dominant solutions by using specific metrics. We also present a sensitivity analysis of the identified dominant solution with respect to variations of parameters that can exhibit changes in the design stage of the capsule as well as for different lengths of the capsule trajectory.

The structure of the chapter is the following: in Section 2.2, we illustrate the hypotheses of the models adopted for representing elements of the capsule's PS and its kinematics. Then, we provide the formulation of the optimization problem to determine the fundamental characteristics of the capsule's PS. In Section III, we use the proposed optimization problem to design the PS of a capsule expected to travel along trajectories of different lengths and we discuss the results with a further sensitivity analysis with respect to parameters that can exhibit changes.

## 2.2 Hypotheses and problem statement

In this chapter, the aerodynamics of the capsule, and the infrastructure dimensions and operations are simplified. The impact on the energy consumption of capsule's auxiliary systems, such as heating, ventilation, and air conditioning (HVAC), passengers entertainment and safety systems is not considered. Furthermore, the energy consumption of the infrastructure is not taken into account since this aspect is treated in Chapter 3. Their detailed models are studied in Chapter 3, as well as the energy consumption on the infrastructure.

### 2.2.1 Trajectory

The closed and sealed path of a hyperloop is provided by an infrastructure composed of a tube or an underground tunnel. Indeed, confining the capsule into a sealed tunnel permits to lower the pressure to values to the order of 5% (50mbar) of the standard atmosphere pressure [11].

As shown in Fig. 2.2, the total length of the trajectory is  $L$  and it is split into  $n$  different zones:  $\{M_1, M_2, \dots, M_n\}$ , where  $j$  represents the generic position of the capsule and  $i$  the elapsed time relative to the generic discrete position,  $j$ . The capsule travels between  $[0, L]$  where the trajectory is sampled at regular intervals,  $\Delta j$ , such that the discrete capsule position is  $j = 0, 1, \dots, \frac{L}{\Delta j}$ . Since the capsule can move only in a single direction, forward, for each  $j$  we can associate a corresponding discrete time index,  $i$  ( $i = 0, \dots, t_{L_k}, \dots, t_L$  in correspondence of the zones  $M_1, \dots, M_k, \dots, M_n$ ).

The space budget of the trajectory for each of the  $n$  zones (2.1) is pre-established by the designer due to the different geographical constraints of the trajectory (see Fig. 2.2).

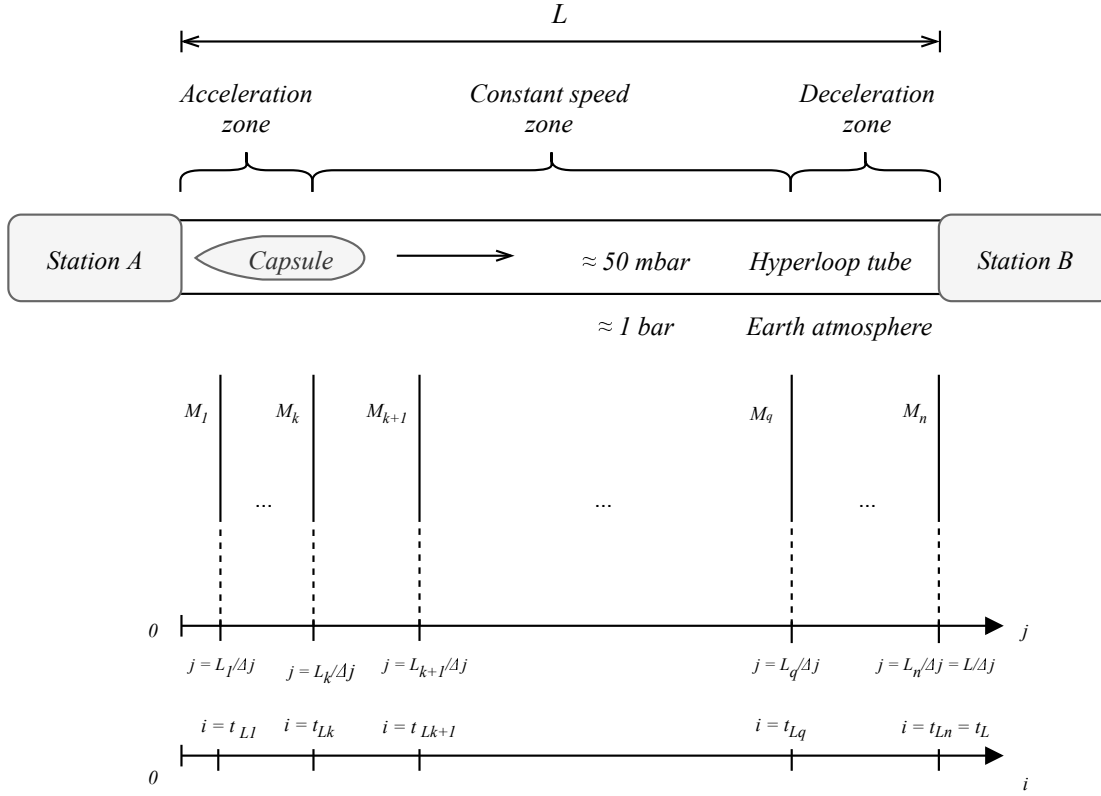


Figure 2.2: The generic trajectory of a hyperloop capsule.

$$\left\{ \begin{array}{l} M_1, \forall j = 0, 1, 2, \dots, \frac{L_1}{\Delta j} - 1 \\ M_2, \forall j = \frac{L_1}{\Delta j}, \frac{L_1}{\Delta j} + 1, \dots, \frac{L_2}{\Delta j} - 1 \\ \dots \\ M_k, \forall j = \frac{L_{k-1}}{\Delta j}, \dots, \frac{L_k}{\Delta j} - 1 \\ M_{k+1}, \forall j = \frac{L_k}{\Delta j}, \dots, \frac{L_{k+1}}{\Delta j} - 1 \\ \dots \\ M_n, \forall j = \frac{L_{n-1}}{\Delta j}, \dots, \frac{L}{\Delta j} \end{array} \right. \quad (2.1)$$

The trajectory is usually separated into typical zones such as: acceleration, constant speed and deceleration (see Fig. 2.2). The  $M_1, \dots, M_k$  zones are reserved for the acceleration, and zones  $M_{k+1}, \dots, M_q$  represent the constant speed ones (where the capsule achieves its maximum speed or the cruising speed). The last zones of the trajectory,  $M_{q+1}, \dots, M_n$ , are used to brake the capsule before reaching the destination.

### 2.2.2 The Model of the Capsule Propulsion System

The architecture of the hyperloop capsule PS is composed of three main components [21]: (i) an energy reservoir consisting of a BESS, (ii) a DC/AC power electronics converter and (iii) an electrical propulsion machine (e.g., a linear induction motor). In the following subsections, we present the models of these subsystems as they constitute some of the constraints of the targeted optimization problem.

#### Model of the capsule power source

There are different approaches to model the electric response of a battery cell, and the choice of the model depends on the complexity of the associated problem. In this respect, there are three main families of models [15], [26], [27]: (i) the so-called “bucket” models, where cells are represented as integral operators of charge/energy eventually by taking into account the associated charge/discharge efficiency, (ii) equivalent circuit models, where the voltage dynamics are simulated by means of an equivalent network of electric lumped components and where the *SoC* is still modeled via an integral operator, and (iii) electrochemical models, where the cell's internal dynamics associated with ion species diffusion and electrochemical reactions are fully modeled. Due to the numerical complexity and large number of state variables required by the third type of cell models, in general, they cannot be directly used into an optimization problem. In this work, we adopt a cell model belonging to the second family. This choice is preferred as it enables to derive a set of numerically tractable constraints capable of capturing the main cell's response especially for a system level design. Fig. 2.3 shows the possible equivalent circuit of a cell where the charge diffusion dynamics are not taken into account [28]<sup>1</sup>. Below, we describe the cell's quantities.

- $V_{OCV}^{cell}$ : represents the open-circuit voltage of the cell, and it is a known function of the cell *SoC* provided by the difference between the cells' electrodes' potentials [29].
- $I_{cell}$ : represents the current flowing through a single cell.
- $R_{cell}$ : represents the equivalent series resistance of the cell. It also encompasses the equivalent resistance of the cell's terminals' connections with the next cell.  $R_{cell}$  is assumed to be known and constant (e.g., we neglect its dependency on the cell's temperature) [30].
- $V_{cell}$ : corresponds to the voltage accessible in the correspondence of the cell's terminals; it is affected by the voltage drop produced by the  $R_{cell}$ .

<sup>1</sup>The adoption of a multiple time constant model of the cell does not affect significantly the results as the time constant of the charge redistribution (in order of hours) is larger than the time spent by the capsule to complete the trajectory (several tens of minutes). For this reason, we prefer the use of the cell model shown in Fig. 2.3. Nevertheless, a detailed analysis about this specific modeling aspect of battery cells is discussed in the Section 2.4 where a two-time constant model of the cell is adopted

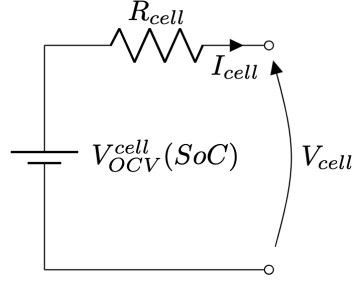


Figure 2.3: Equivalent circuit of a cell adopted to derive the BESS constraints.

In a first approximation, the model of an entire BESS pack composed by identical cells can mathematically be described by (2.2), where  $N_s$  and  $N_p$  represent the number of series cells and the number of parallel cells of the BESS, respectively.  $V_{OCV}^{batt}$  represents the open-circuit voltage, which is solely a function of the cells  $SoC$ ; whereas  $R_{batt}$  integrates the all the cells' and connectors' resistances.  $C_{batt}$  represents the capacity of the BESS.  $I_{batt}$  is the total current provided (or absorbed) by the BESS.<sup>II</sup>

$$\left\{ \begin{array}{l} V_{OCV}^{batt} = f(SoC) \\ V_{OCV}^{batt} = V_{OCV}^{cell} N_s \\ R_{batt} = R_{cell} \frac{N_s}{N_p} \\ I_{batt} = I_{cell} N_p \\ SoC = SoC(0) + \int_0^{t_L} \frac{I_{batt}}{C_{batt}} dt \end{array} \right. \quad (2.2)$$

Hence,  $V_{batt}$  and  $P_{batt}$ , are the accessible voltage and power of the BESS (2.3).

$$\left\{ \begin{array}{l} V_{batt} = N_s(V_{OCV}^{cell} - R_{cell} I_{cell}) \\ P_{batt} = I_{batt} V_{batt} \end{array} \right. \quad (2.3)$$

The function  $V_{OCV}^{batt}(SoC)$  is usually available from the cell's manufacturer.

### Propulsion

Speed and acceleration profiles are a function of the traction force provided by different types of electrical motors characterized by different performances.

For the ensemble of the electrical machine and converter, the most important parameters are

<sup>II</sup> A look-up table-based model of the BESS containing the cell temperature can be used to better model the behavior of the BESS.



- $\frac{P}{PS_{weight}}$  which represents the ratio between the total amount of power per unit mass.
- $V_{DC}^{max}$  which represents the maximum allowable DC voltage of the DC/AC converter.

### 2.2.3 Capsule Kinematic Model

We assume the capsule to be capable of carrying a payload mass defined by the designer,  $m_{payload}$ . In order to parametrize the total mass of the capsule as a function of the problem's decision variables (that define the PS), we divide the total mass in two: a passive mass,  $m_0$ , and an active mass,  $m_{active}$ .

$$m = m_0 + m_{active} \quad (2.4)$$

The passive mass represents the payload plus the mechanical sub-system masses,  $m_{mechanics}$ , such as the capsule's aeroshell, chassis, pressure vessels, stability mechanisms, braking mechanism and, if present, magnets for levitation.

$$m_0 = m_{payload} + m_{mechanics} \quad (2.5)$$

The active mass includes the mass of the BESS,  $m_{BESS}$ , plus the one of the motor and DC/AC converter,  $m_{PS}$ . The mass of the BESS is proportional to the product between  $N_s$  and  $N_p$  times the cell's mass,  $m_{cell}$  (we assume that the cell mass is associated with cells' unitary mass plus cells' wiring and packaging).

Henceforth, we explicitly refer to the case of linear induction motors (LIM) [31]–[34] as this specific electrical machine is considered to be among the best choices for energy-autonomous hyperloop capsules since it does not require the electrification of the rail. Another advantage of using a LIM in the architecture of a hyperloop capsule is the maintenance procedure. With a contactless solution, PS periodical mechanics-maintenance procedures may take place more rarely. Both aforementioned factors result in diminishing the price costs for the infrastructure and maintenance.

We assume that the LIM is characterized by a given weight per unit of input power density  $k_1$  (considering a passive cooling), and the voltage source inverter (VSI) to be characterized by a given weight per unit of input power density  $k_2$  (considering a passive cooling). The total mass of the PS,  $m_{PS}$ , can then be simply linked to the maximum electrical power to be delivered along the trajectory for the capsule,  $P_{max}$ , via (2.6) and (2.7) where  $P_{LIM}$  and  $P_{VSI}$  are the maximum powers of the LIM and VSI, respectively.

$$\begin{cases} m_{active} = m_{BESS} + m_{PS} \\ m_{BESS} = N_s N_p m_{cell} \\ m_{PS} = P_{max}(k_1 + k_2) \end{cases} \quad (2.6)$$

$$k_1 = \frac{m_{LIM}}{P_{LIM}}; k_2 = \frac{m_{VSI}}{P_{VSI}} \quad (2.7)$$

In order to express the mass of the PS as a function of the mechanical power provided to the capsule, we assume that the maximum power provided by the BESS is equal to the maximum power of the LIM and to the one of the VSI in order to optimize the performances of the PS [35]. In order to determine the mass of the PS, we should consider the maximum output PS power given by the peak output power of the BESS multiplied with the traction system efficiency. However, there is an important observation to be made regarding the cooling of the PS. Indeed, capsules are traveling in an environment where the reduced pressure drastically compromise the heat exchange. First, it is interesting to note that the time spent by the capsules to travel hundreds of kilometers at subsonic speeds it is in the range of tens of minutes. These two observations may justify the decision to accumulate all the heat losses of the VSI and LIM in their masses. This design option may largely simplify a complex cooling system that in any case will be inefficient for pressures below hundreds of mbars. For these reasons, the mass of the PS is considered to be inverse proportional to its efficiency: in order to have larger mass for lower efficiencies of the VSI and LIM. Therefore, by introducing the transfer efficiency of the capsule PS,  $\eta$ , the mass  $m_{PS}$  can be computed as in (2.8), where  $P_{maxCell}$  is the maximum power provided by a cell that can be computed using (2.3).

$$m_{PS} = \frac{1}{\eta} P_{maxCell} N_s N_p (k_1 + k_2) \quad (2.8)$$

Thus, the final expression of total mass is given by (2.9) where  $m \sim N_s N_p$ .

$$m = m_0 + N_s N_p m_{cell} + \frac{1}{\eta} P_{maxCell} N_s N_p (k_1 + k_2) \quad (2.9)$$

Throughout the trajectory, the capsule is represented by a kinematic model where the state variables are the acceleration,  $a$ , and speed,  $v$ , sampled along the trajectory (as shown in Fig. 2.2) with  $\Delta j$ , or time intervals  $\Delta i$  corresponding to  $\Delta j$ .  $\Delta i$  is computed with respect to  $\Delta j$  through solving the associated equation:  $\Delta j = v(j-1)\Delta i + \frac{1}{2}a(j)\Delta i^2$  required to have a uniform varied motion. The total length of the trajectory is  $L$  and is divided, as in (2.1), into three main parts: acceleration, constant speed, and braking. Thus, the total number of discrete analysis points along the trajectory is  $\lceil \frac{L}{\Delta j} \rceil$ . Subsequently, the links of the discretized state variables of the capsule as a function of the power provided by the PS are derived.

One of the most significant advantages of the hyperloop consists in the reduction of the drag force [36] as it is proportional to the fluid density ( $\rho$ ). Equation (2.10) provides the simplest expression of the drag force as a function of the generic position of the capsule along the trajectory, where  $C_d$  represents the drag coefficient of the capsule and  $S$  the cross section surface of the capsule.

$$F_{drag}(j) = \frac{1}{2} S C_d \rho v(j)^2 \quad (2.10)$$

The PS traction force and traction power as a function of the generic capsule position along the trajectory are given by (2.11) and (2.12), respectively.

$$F_{traction}(j) = ma(j) + F_{drag}(j) \quad (2.11)$$

$$P_{traction}(j) = F_{traction}(j) \cdot v(j) \quad (2.12)$$

By integrating (2.9), (2.10), (2.11) and (2.12), we obtain the following expression for the traction power,  $P_{traction}$ , as a function of  $m$ ,  $a$  and  $v$ .

$$P_{traction}(j) = (ma(j) + F_{drag}(j)) \cdot v(j) \quad (2.13)$$

Once reaching the maximum speed,  $v_{max}$  at  $x_{v_{max}}$ , the instantaneous power consumption of the capsule is minimal and flattened due to (2.11). This simple observation, supported by the numerical results of Section III, permits us to state that the hyperloop PS application is closer to a power-intensive application rather than an energy-intensive one. Still, due to the variation of  $V_{batt}$  associated with the variations of the  $SoC$  for a relatively long journey, the effect of depth-of-discharge ( $DoD$ ) on the  $V_{OCV}^{cell}$  represents an element that should be taken into account in the problem formulation.

#### 2.2.4 Formulation of the Optimization Problem

In view of the above-illustrated models of the capsule power-source, PS and kinematic model, we formulate the problem for the optimal design of the capsule PS as in (2.14).

$$\begin{aligned}
& \min_{N_s N_p, a} \quad N_s N_p - w \cdot \|a\|_2 \\
& \text{subject to} \quad j = 0, 1, 2, \dots, \frac{L_q}{\Delta j} - 1 \\
& \quad v(j) \leq v_{max} \\
& \quad a_{min_{M_1}} \leq a(j) \leq a_{max_{M_1}}, \forall j = 0, 1, 2, \dots, \frac{L_1}{\Delta j} - 1 \\
& \quad \dots \\
& \quad a_{min_{M_q}} \leq a(j) \leq a_{max_{M_q}}, \forall j = \frac{L_{q-1}}{\Delta j}, \dots, \frac{L_q}{\Delta j} - 1 \\
& \quad \frac{L^2}{\sum_{j=0}^{\frac{L}{\Delta j}} v(j) \cdot \Delta j} \leq T_{max_q} \\
& \quad P_{traction} \leq \eta P_{batt} \\
& \quad SoC_{min} \leq SoC \leq SoC_{max} \\
& \quad I_{cell}(j) \leq I_{cellMax} \\
& \quad V_{OCV}^{cell}(0) = V_{OCV}^{cell} |_{SoC=SoC_{max}} \\
& \quad V_{OCV}^{batt} = V_{OCV}^{cell} N_s \\
& \quad R_{batt} = R_{cell} \frac{N_s}{N_p} \\
& \quad I_{batt} = I_{cell} N_p \\
& \quad C_{batt} = N_p C_{cell} \\
& \quad SoC = SoC(0) + \sum_{i=1}^{t_L} \frac{I_{batt}}{C_{batt}} \Delta i \\
& \quad \Delta i = \frac{-v(j-1) + \sqrt{v^2(j-1) + 2a\Delta j}}{a} \\
& \quad V_{batt} = N_s (V_{OCV}^{cell} - R_{cell} I_{cell}) \\
& \quad P_{batt} = I_{batt} V_{batt} \\
& \quad m = m_0 + m_{active} \\
& \quad m_0 = m_{payload} + m_{mechanics} \\
& \quad m_{active} = m_{BESS} + m_{PS} \\
& \quad m_{BESS} = N_s N_p m_{cell}; \quad m_{PS} = P_{max}(k_1 + k_2) \\
& \quad k_1 = \frac{m_{LIM}}{P_{LIM}}; \quad k_2 = \frac{m_{VSI}}{P_{VSI}} \\
& \quad m_{PS} = \frac{1}{\eta} P_{maxCell} N_s N_p (k_1 + k_2) \\
& \quad m = m_0 + N_s N_p m_{cell} + \frac{1}{\eta} P_{maxCell} N_s N_p (k_1 + k_2) \\
& \quad F_{drag}(j) = \frac{1}{2} SC_d \rho v(j)^2 \\
& \quad F_{traction}(j) = ma(j) + F_{drag}(j) \\
& \quad P_{traction}(j) = (ma(j) + F_{drag}(j)) \cdot v(j)
\end{aligned} \tag{2.14}$$

The objective function is composed of two elements: the weight of the BESS and the performance of the capsule represented by the norm-2 of the array of the discrete accelerations sampled along the trajectory. We maximize  $\|a\|_2$  as this value can be directly linked to the traveling time to complete the trajectory. Indeed, for the acceleration and constant-speed zones (that represent the large part of the trajectory), we know that  $\frac{v(j+1)-v(j)}{\Delta i} \geq 0$ , which also implies  $\frac{v(j+1)-v(j)}{\Delta j} \geq 0, \forall j \leq \frac{L_q}{\Delta j} - 1$ . Therefore, we can say that

$$\min \left( \frac{L^2}{\sum_{j=0}^{\frac{L}{\Delta j}} v(j) \cdot \Delta j} \right) \iff \max(v_{max}). \quad (2.15)$$

As  $v_{max}$  can be expressed as

$$v_{max} = \int_{t_0}^{t_{L_k}} a(\tau) d\tau \simeq \sum_{i=0}^{t_{L_k}} a(i) \Delta i, \quad (2.16)$$

from (2.15) and (2.16), if we want to maximize  $v_{max}$ , we have to maximize  $\sum_{i=0}^{t_{L_k}} a(i) \Delta i$ , which implies maximizing  $\|a\|_1$ . We choose to maximize the  $\|a\|_2$  in order to give more weight to the higher values of the acceleration along the trajectory.

It is worth noting that, as  $N_s N_p$  and  $\|a\|_2$  in the objective function of (2.14) are different physical quantities, a weight factor,  $w$ , is necessary in order to normalize them.

It is worth observing that the constraints have explicitly considered that the maximum speed of the capsule cannot exceed a pre-determined value,  $v_{max}$ , and that the average traveling time cannot be longer than a certain given threshold,  $T_{max_q}$  depending on the length of trajectory,  $L$ . Furthermore, the acceleration in the zones  $M_1, M_2, \dots, M_k$  are upper bounded by values compatible with airplanes acceleration profiles. We also constrained the  $I_{cell}$  to be lower than the maximum admissible discharge rate of the considered cell. For the BESS, the  $V_{OCV}^{batt}$  is initially chosen with respect to the railway electrification system standard. Finally, the SoC should be in the safe range, bounded by  $SoC_{min}$  and  $SoC_{max}$  defined by the designer. The two boundary values are considered in the optimization problem, (2.14).

A final comment is about the deceleration stage performed in the zones  $M_{q+1}, \dots, M_n$ . In these zones, the capsule actuates the braking: a dominant part of the deceleration is assumed to be produced by a dissipative braking mechanism (i.e., a mechanical system producing friction force given by braking pads in contact with the infrastructure's rail) whereas a minimal part is

assumed to be produced by a regenerative one [37], [38]. As the regenerative braking enables us to recover a minimal part of the capsule's kinetic energy limited by the maximum charging rate of the considered cell,  $I_{cellMaxcharge}$ , it is not taken into account in the optimization problem. Therefore, in (2.14), the optimization problem is applied only for the acceleration and constant speed zones. However, in the numerical results, we charge the BESS in the zone  $M_{q+1}, \dots, M_n$  with  $I_{cellMaxcharge}$ . This enables us to compute the *SoC* at the end of the trajectory,  $SoC_{final}$ .

The problem (2.14) is non-convex due to the discrete nature of its equations as well as the *SoC* expression. Indeed, in equation (2.2), the denominator of the integrating function (i.e.  $C_{batt}$ ) is function of the control variable  $N_p$  ( $C_{batt} = N_p C_{cell}$ ). Since  $I_{batt}$  and the *SoC* are an internal and constrained variable of the problem, both dependent on the control variables, the constraint expressed through equation (2.2) is non-convex. The problem has been solved using a gradient-based method [39], [40], and we use first-order optimality conditions to determine whether a local minima has been identified. For the solution of a single problem corresponding to a given  $w$  and a single set of  $N_s N_p$  and  $a$  initializations, we have got an average computational time of approximately 35 to 37 seconds using a standard laptop (3.5 GHz Intel Core i7 with 16 GB 2133 MHz LPDDR3 memory).

## 2.3 Numerical results

### 2.3.1 Assumptions on the Capsule Trajectory

For a concrete example, the proposed optimization is applied to design the PS of a capsule expected to travel between the two largest cities in Switzerland: Geneva and Zürich<sup>III</sup>. The first length of the trajectory is  $L = 226km$ <sup>IV</sup>. In order to extensively validate the optimization process, other two lengths of the trajectory have been considered  $L = 500km$  and  $L = 1000km$ .

The considered trajectories have been segmented in the zones reported in (2.17) for  $L = 226km$ , (2.18) for  $L = 500km$  and (2.19) for  $L = 1000km$ , where  $M_1$  and  $M_2$  represent the acceleration zones,  $M_3$  is the constant speed zone, and  $M_4$  the deceleration one. The discrete sampling of the trajectory is  $\Delta j = 100m$ .  $\Delta j$  has been chosen with two characteristics: (i)  $\Delta j \ll \min(L_m), \forall m = 1, 2, \dots, n$  and (ii) determine an integer number of discrete points in order to have a coherent spatial sampling of the trajectory. To fix ideas, it results in a total number of 2260 discrete points for  $L = 226km$ , 5000 discrete points for  $L = 500km$  and 10000 discrete points for  $L = 1000km$ .

<sup>III</sup>The actual travel time between these two cities with the Swiss public train company is in the order of 2h30min, whereas time travel by plane is around 45 minutes (not including the boarding).

<sup>IV</sup>Although this parameter is expected to influence the results of the optimization, the value we selected enables us to deploy a fast-charging strategy between subsequent stops of the capsule along a longer journey.

$$\begin{cases} M_1, \forall j = 0, 1, 2, \dots, \frac{L_1}{\Delta_j} - 1, \text{ with } L_1 = 5km \\ M_2, \forall j = \frac{L_1}{\Delta_j}, \dots, \frac{L_2}{\Delta_j} - 1, \text{ with } L_2 = 26km \\ M_3, \forall j = \frac{L_2}{\Delta_j}, \dots, \frac{L_3}{\Delta_j} - 1, \text{ with } L_3 = 206km \\ M_4, \forall j = \frac{L_3}{\Delta_j}, \dots, \frac{L}{\Delta_j}, \text{ with } L = 226km \end{cases} \quad (2.17)$$

$$\begin{cases} M_1, \forall j = 0, 1, 2, \dots, \frac{L_1}{\Delta_j} - 1, \text{ with } L_1 = 5km \\ M_2, \forall j = \frac{L_1}{\Delta_j}, \dots, \frac{L_2}{\Delta_j} - 1, \text{ with } L_2 = 26km \\ M_3, \forall j = \frac{L_2}{\Delta_j}, \dots, \frac{L_3}{\Delta_j} - 1, \text{ with } L_3 = 480km \\ M_4, \forall j = \frac{L_3}{\Delta_j}, \dots, \frac{L}{\Delta_j}, \text{ with } L = 500km \end{cases} \quad (2.18)$$

$$\begin{cases} M_1, \forall j = 0, 1, 2, \dots, \frac{L_1}{\Delta_j} - 1, \text{ with } L_1 = 5km \\ M_2, \forall j = \frac{L_1}{\Delta_j}, \dots, \frac{L_2}{\Delta_j} - 1, \text{ with } L_2 = 26km \\ M_3, \forall j = \frac{L_2}{\Delta_j}, \dots, \frac{L_3}{\Delta_j} - 1, \text{ with } L_3 = 980km \\ M_4, \forall j = \frac{L_3}{\Delta_j}, \dots, \frac{L}{\Delta_j}, \text{ with } L = 1000km \end{cases} \quad (2.19)$$

### 2.3.2 Assumptions on the Capsule and PS

The capsule is assumed to carry a payload mass equivalent to 25 persons (this payload might be replaced by a cargo one). The average mass payload attributed for a single person is 80kg, which means  $m_{payload} = 2000kg$ .

#### Other general mechanical parameters

We assume the capsule to have a total mass of the mechanical sub-systems of 6000kg (therefore,  $m_0 = 8000kg$ ), a frontal cross-section surface  $S = 6m^2$  [42] and the value of the drag coefficient  $C_d = 0.1$  [43]. The aggregated efficiency of the LIM and VSI is also assumed to be  $\eta = 0.95$  [4].

The upper bounds for the accelerations in the stages  $M_1$  and  $M_2$  are selected to be in the same order of magnitude of maximum accelerations imposed by modern passenger aircrafts. In (2.20) we summarize the upper bounds for  $M_1$  and  $M_2$  (note that  $g = 9.81 \frac{m}{s^2}$ ), along with the maximum speed,  $v_{max}$ , and maximum travel time  $T_{max_q}$ . The maximum travel times are

bounded by using the factor  $\phi = \frac{L}{T_{max1}}$ <sup>V</sup> assumed to be equal to  $11.3 \frac{km}{min}$ .

$$\left\{ \begin{array}{l} v_{max} = 1200 \frac{km}{h} \\ T_{max1} = 20min; T_{max2} = 44.25min; T_{max3} = 88.5min \\ a_{min_{M1}} = 0.05g; a_{max_{M1}} = 0.9g \\ a_{min_{M2}} = 0.05g; a_{max_{M2}} = 0.6g \\ a_{min_{M3}} = 0g; a_{max_{M3}} = 0.001g \end{array} \right. \quad (2.20)$$

## BESS

We assume the BESS to be composed by Lithium-Polymer NMC cells. In this respect, the numerical results of this section are inferred using a real cell, the Kokam SLPB 11543140H5. This specific cell was selected in view of its excellent power density and very-high discharge rate since these two are the most important cell characteristics for our application. More specifically, the cell can sustain a continuous discharge rate up to 30C and exhibits remarkable performance in terms of ageing (more than 1000 cycles at 90% depth-of-discharge). Its parameters have been fully characterized at the Authors' laboratory.

Concerning the maximum value for the  $V_{OCV}^{batt}$ , it was chosen based on "Railway applications – Supply voltages of traction systems" according to IEC 60850 standard [44]. Thereby, the values defined in (2.2) imply a  $V_{OCV}^{batt} = 1.5kV$  for  $SoC_{max} = 100\%$ .

The constraints of the  $SoC$  mark a safe operation zone of the BESS in order to guarantee that the cell will wear with the expected ageing and that they were selected according to the manufacturer's specifications. The cell-equivalent series resistance was measured at the Authors' laboratory at an operating temperature between  $15 - 35^\circ C$ . Concerning the maximum discharge current, it also results from the cell capacity (5Ah) and maximum continuous discharge rate (30C). The charging current used by the regenerative braking is limited to 1C. Also, this value is according to the manufacturer's data.

$$\left\{ \begin{array}{l} SoC_{max} = 100\% \\ SoC_{min} = 10\% \\ R_{cell} = 4.4m\Omega \\ I_{cellMax} = 150A \\ I_{cellMaxcharge} = 5A \end{array} \right. \quad (2.21)$$

It is worth observing that using a pre-sized series/parallel groups of cells for the BESS design, instead of individual cells, may represent a different approach to numerically solve the

<sup>V</sup>The value of  $\phi$  is defined by the designer/modeler.



problem.

### Propulsion

The weight per unit power density of the LIM,  $k_1$ , is selected by making reference to a hyperloop prototype developed in our laboratory whilst the same parameter for the VSI,  $k_2$ , was inferred using industrial-grade VSI used in the automotive sector.

$$\begin{cases} k_1 = 0.091 \frac{kg}{kW} \\ k_2 = 0.075 \frac{kg}{kW} \end{cases} \quad (2.22)$$

### 2.3.3 Results

Problem (2.14) was solved for the three different lengths of the trajectory, corresponding to three different average travel time constraints as shown in (2.20). For every length of the trajectory, Algorithm 1 is used in order to solve problem (2.14) using `fmincon` in Matlab R2020, where the normalization factor  $w$  was varied from  $10^0$  to  $10^8$  in a decade-logarithmic way and, for each of its values, the control variables  $N_s N_p$  and  $a$  were initialized with different values (these initial values were selected in a range where they have a feasible technical meaning). An example for the behaviour of the problem objective, for  $L = 226km$  and  $w = 100$ , as a function of the initial values of  $N_s N_{p,init}$  and  $a_{init}$  is given in Fig. 2.4. We generated the solution space in Fig. 2.4 with the different initialization of  $a$  and  $N_s N_p$  for  $w = 100$  and  $L = 226km$  by solving (2.14). This process was repeated for all the values of  $w$  and  $L$  where the white zone of the figure represents the minimum of the optimization problem (2.14). For the minimum point in Fig. 2.4 (identified within the white zone of the graph) we extract the corresponding trajectory information regarding the acceleration, speed, and time profiles, with respect to the position of the capsule and BESS status. The cluster of information found for each of the solutions contains all the necessary trajectory and system details of the capsule. The knowledge of the acceleration profile enables us to compute the speed profile (Fig. 2.5) along with the traction power profile (Fig. 2.6) and cell-current profile (Fig. 2.7) of the capsule.

---

#### Algorithm 1

---

- 1: **for**  $w = 10^0 \rightarrow 10^8$
  - 2:   **for**  $a_{init} = 0 \rightarrow 1, \Delta a_{init} = 0.1$
  - 3:     **for**  $N_s N_{p,init} = 0 \rightarrow 10000, \Delta N_s N_{p,init} = 1000$
  - 4:       Solve (2.14)
  - 5:     **end for**
  - 6:   **end for**
  - 7:   Find  $N_s N_p$  and  $a$  with min obj
  - 8: **end for**
-

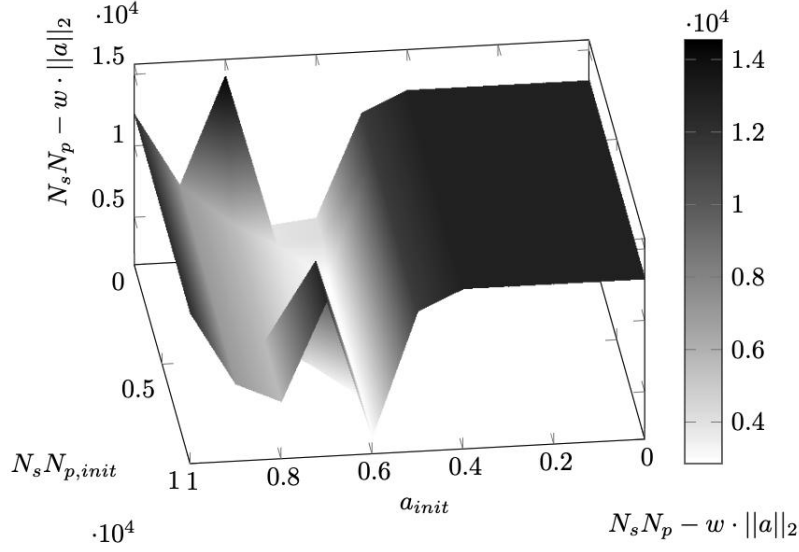


Figure 2.4: Behaviour of the problem objective for  $L = 226km$  and  $w = 100$  as a function of the initial values of  $N_s N_{p,init}$  and  $a_{init}$ .

With Algorithm 1, the following figures show, for every length of the trajectory,  $L$ , the Pareto fronts of the most important capsule performance indicators and key parameters of the PS as a function of the normalization factor  $w$ . More specifically, Fig. 2.8 shows the values of the total number of cells of the BESS, Fig. 2.9 shows the capsule and the BESS masses, Fig. 2.10 and Fig. 2.11 show the maximum speed and acceleration achieved along the trajectory, Fig. 2.12 shows the maximum traction power, Fig. 2.13 shows the final  $SoC$  of the BESS,  $SoC_{final}$ , and Fig. 2.14 shows the average time necessary to cover the trajectory.

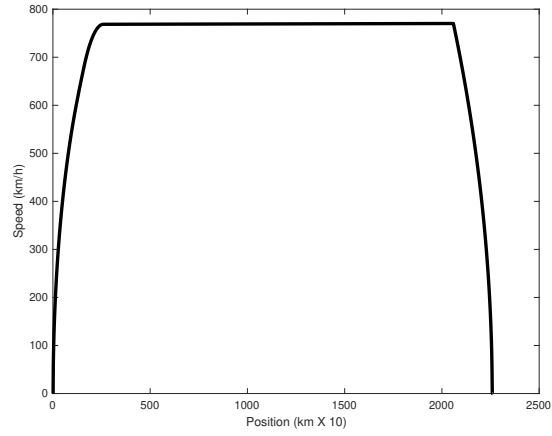


Figure 2.5: Optimal-speed profile for  $L = 226\text{km}$ ,  $w = 100$ ,  $a_{init} = 0.6 \frac{m}{s^2}$ ,  $N_s N_{p,init} = 2000\text{cells}$ .

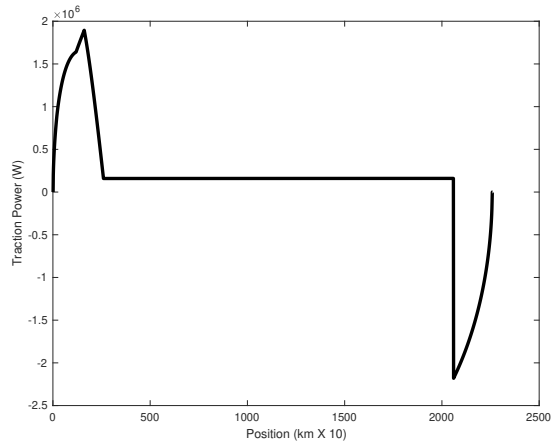


Figure 2.6: Optimal traction-power profile for  $L = 226\text{km}$ ,  $w = 100$ ,  $a_{init} = 0.6 \frac{m}{s^2}$ ,  $N_s N_{p,init} = 2000\text{cells}$ .

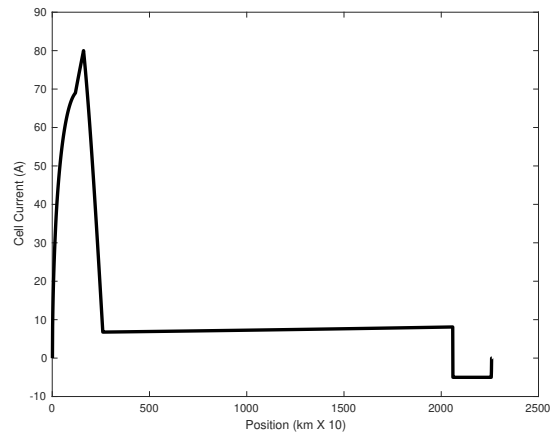


Figure 2.7: Optimal cell-current profile for  $L = 226km$ ,  $w = 100$ ,  $a_{init} = 0.6 \frac{m}{s^2}$ ,  
 $N_s N_{p,init} = 2000 cells$ .

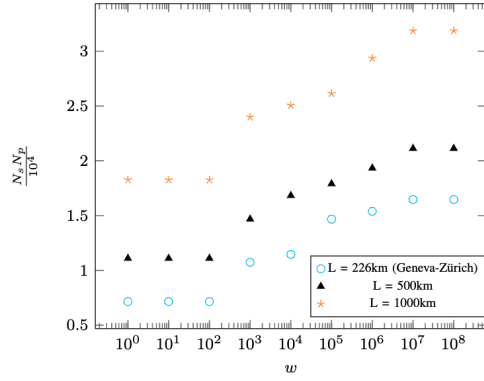


Figure 2.8: Total number of cells of the BESS.

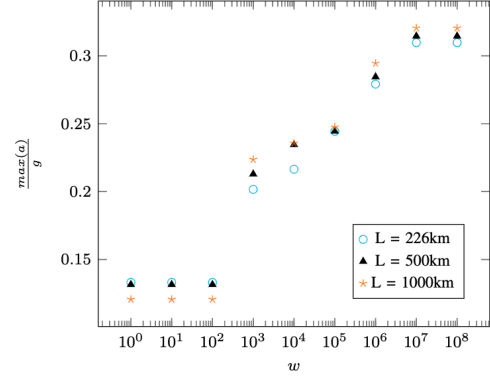


Figure 2.11: Maximum acceleration along the trajectory (values in per-unit to g).

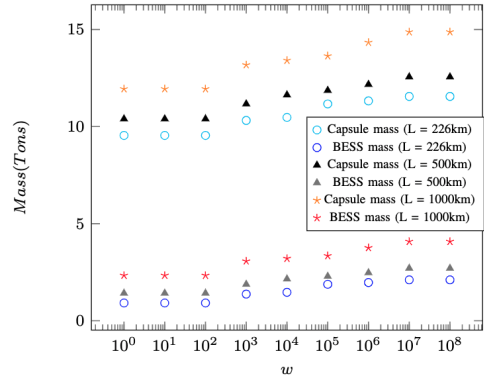


Figure 2.9: Capsule and BESS masses.

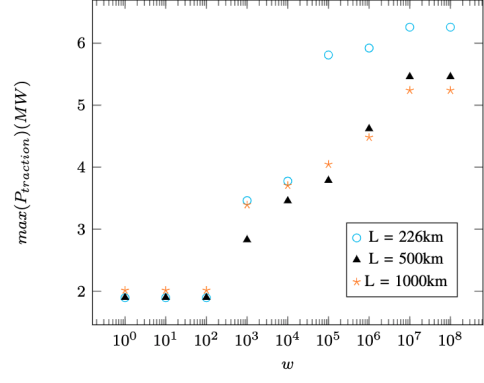


Figure 2.12: Maximum traction power provided by the capsule PS along the trajectory.

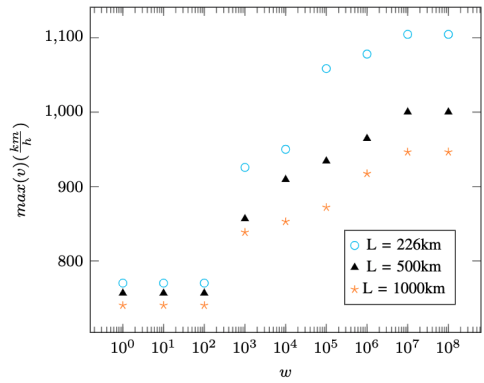


Figure 2.10: Maximum speed along the trajectory.

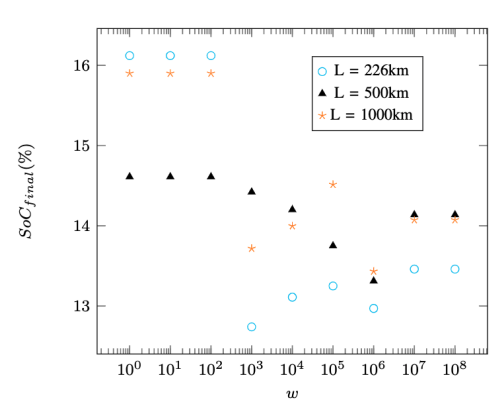


Figure 2.13: BESS SoC at the end of the trajectory.

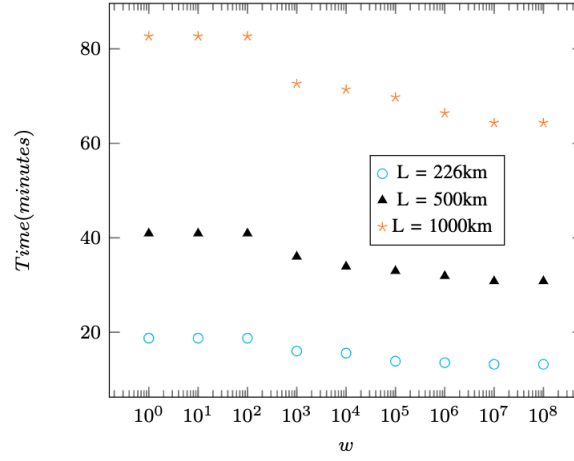


Figure 2.14: Average time necessary to cover the trajectory.

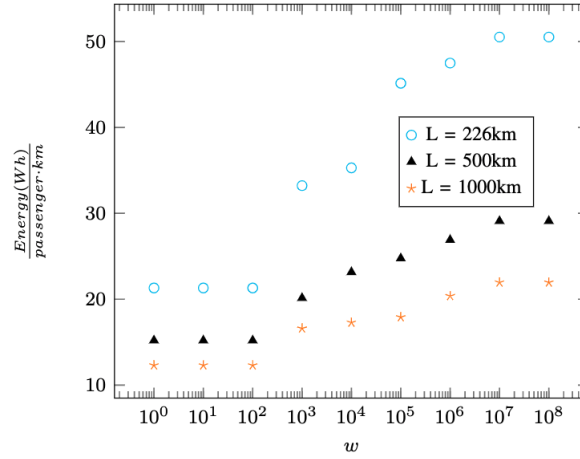


Figure 2.15: The energy consumption per passenger per km.

### 2.3.4 General Observations

As shown in Fig. 2.12, the maximum instantaneous power along the trajectory for the longer distances (i.e.,  $L = 500\text{km}$  and  $L = 1000\text{km}$ ) is similar for the various solutions and in the range of 2 to 5.5 MW. For the shorter distance ( $L = 226\text{km}$ ) the maximum power applied by the capsule's PS is, instead, larger due to two reasons: (i) the cruising speed (maximum speed) along the trajectory is smaller due to the amount of time that the capsule spends at that speed which enables minimizing the average traveling time, and (ii) the solutions of the optimization problem are governed by the *SoC* constraint while the discharge rate and *DoD* of the cell are underused.

The normalization factor  $w$  has, as expected, a substantial influence on the obtained optimal solutions. For relatively small values of  $w \in [10^0; 10^2]$ , the maximum acceleration (see Fig. 2.11)

is half of the maximum one imposed by a modern passenger aircraft. The corresponding BESS is not larger than  $1000\text{ kg}$ ,  $1500\text{ kg}$  and  $2500\text{ kg}$  for  $L = 226$ ,  $L = 500\text{ km}$ , and  $L = 1000\text{ km}$  respectively. The maximum capsule acceleration grows rapidly as  $w$  increases up to a point where it saturates. Hence, for  $w > 10^3$ , the maximum acceleration increases up to  $0.3 \div 0.32g$ ; this represents the maximum acceleration obtained for the considered cell and the assumptions on the capsule characteristics for three different lengths. The maximum instantaneous power is about  $6.25\text{ MW}$  (for  $L = 226\text{ km}$ ) and  $5.5\text{ MW}$  (for  $L = 500\text{ km}$  and  $L = 1000\text{ km}$ ) for  $w \in [10^7, 10^8]$  and is associated to a total number of cells of  $N_s N_p = 16468$ ,  $N_s N_p = 21122$ ,  $N_s N_p = 31862$ . The maximum speed for the different lengths,  $L = 226\text{ km}$ ,  $L = 500\text{ km}$ ,  $L = 1000\text{ km}$  varies between  $771 \frac{\text{km}}{\text{h}} - 1104 \frac{\text{km}}{\text{h}}$ ,  $757 \frac{\text{km}}{\text{h}} - 1000 \frac{\text{km}}{\text{h}}$ , and  $740 \frac{\text{km}}{\text{h}} - 946 \frac{\text{km}}{\text{h}}$  respectively. For larger distances, the optimal maximum-speeds intervals given by the minimum and maximum value of  $w$  shrinks down due to the linear increase of the maximum travel time constraint and the longer zones travelled by the capsule at the maximum speed.

As already stated in Fig. 2.4, the minima of the objective function given in (2.14) for  $w = 100$  and  $L = 226\text{ km}$  is found for the following initialization:  $a_{init} = 0.6 \frac{\text{m}}{\text{s}^2}$  and  $N_s N_{p,init} = 2000\text{ cells}$ . In Fig. 2.5, the optimal-speed profile is shown, hence computed as a result of the optimal-acceleration profile solved in (2.14). The capsule achieves its maximum speed at  $771 \frac{\text{km}}{\text{h}}$ , and constantly runs at this speed, until the deceleration zone. The two different acceleration zones are clearly observed in Fig. 2.6, where the optimal-traction power profile is presented. Before achieving its peak of power, due to the two different acceleration zones (after  $L_1 = 5\text{ km}$ ), and to the increase of speed, the traction profile exhibits a transition because of (2.13). The instantaneous power of the capsule substantially reduces once the maximum speed is achieved; and, due to the low-pressure atmosphere, even at high-speeds, the necessary amount of injected power to maintain the constant speed is low—relative to the maximum instantaneous power given by the acceleration zone. We present the current consumption for a given cell from the BESS in Fig. 2.7, as a result of (2.2). The profile of the current consumption for a single cell is similar to the profile of the power profile presented in Fig. 2.6, except for the constant-speed zone of the capsule. In this zone, due to the variation of the cell voltage with the SoC in (2.2), and in order to keep a constant power of the capsule, the current consumption slightly increases from the moment when the maximum speed is achieved until the braking zone. The peak of current consumption over the trajectory represents almost half of the maximum allowed discharge rate of the cell. The other optimal profiles for speed, traction power, cell current consumption look similar as the presented ones for every  $w$  and  $L$ . However, due to the low-energy density of the cell, the solution of the optimization problem is constrained by the level of SoC. For higher values of  $w$ , where the solution is represented by larger values of the instantaneous power of the capsule (Fig. 2.12), the solution of the problem is constrained by the discharge rate of the cell and not by the level of SoC.

The identified hyperloop PS solutions are feasible with the today's cell technology. In a range of  $0.9 - 2\text{ tones}$ ,  $1.4 - 2.7\text{ tones}$ , respectively  $2.3 - 4\text{ tones}$  of battery cells (Fig. 2.8 and Fig. 2.9), most of the mass is still distributed between the mechanical sub-systems and the payload. Another outcome is related to the level of the SoC. The problem has been constrained for a

minimum  $SoC$  value of 10% before the regenerative braking zone. Therefore, all the available BESS energy is absorbed at the end of the constant-speed zone, and the level of  $SoC$  tends to the minimum value imposed by the optimization problem. Due to the low charging rate of the cell (1C), compared with the discharge rate (30C), the level of  $SoC_{final}$  presented in Fig. 2.13 does not reach high values.

In Fig. 2.14, the average traveling time stays in the range of 13 – 19 *minutes*, 31 – 40 *minutes*, respectively 65 – 83 *minutes*, where the upper boundary of this range is governed by the lower values of  $w$  ( $w = \{1, 10, 100\}$ ). Indeed, the average traveling time is related to the maximum speed over the trajectory given in Fig. 2.10, as a result of the acceleration profile, where every maximum point, with respect to  $w$ , can be found in Fig. 2.11.

Irrespectively of the value of  $w$ , it is important to observe that the obtained BESS masses and the total number of cells are compatible with the currently proposed applications in commercial heavy-duty electric vehicles (e.g., electric trucks). The same observation applies to the maximum powers obtained for the other elements of the capsule propulsion. Therefore, the results indicate the technical feasibility of the identified capsule propulsion using today's technologies. To the best of the Authors' knowledge, this is the first paper in the literature that provides numerical support to this fundamental observation for the hyperloop capsules PS design. With a battery-energy reservoir not larger than 10MW, hyperloop can offer a transportation system for goods or people at speeds of  $1000 \frac{km}{h}$  with accelerations comparable with the commercial aircrafts.

A final remark is about the estimation of the required energy/passenger/km given in Fig. 2.15. This estimation refers only to the capsule's energy consumption and does not include the hyperloop-tube vacuuming process. For this computation, the BESS charging efficiency is considered to be:  $\eta_{charging} = 89.4\%$  [45]– [47]. It is worth observing that, for the identified solution corresponding to  $w = 100$ , we obtain values in the order of  $22 \frac{Wh}{passenger \cdot km}$  for  $L = 226km$ ,  $15.2 \frac{Wh}{passenger \cdot km}$  for  $L = 500km$  and  $12.3 \frac{Wh}{passenger \cdot km}$  for  $L = 1000km$ . The results show an interesting finding: for longer distances (i.e.,  $L = 500km$  and  $L = 1000km$ ), the energy consumption per passenger per km is dropping down. This important compression of the average energy consumption is mostly influenced by the longer time spent by the capsule at the cruising speed where the power consumption of the capsule is flattened (and minimal).

The solutions corresponding to longer distances (i.e.,  $L = 500km$  and  $L = 1000km$ ) present similar maximum instantaneous power profiles (Fig. 2.12) even if they present different masses and different lengths. With similar acceleration profiles, the difference is made by the speed profiles and the time spent at the cruising speed, and the  $SoC$  limitation which is directly influenced by the speed profile and mass of the capsule.



### 2.3.5 Dominant Solutions

For the sake of comparing the results, it is necessary to identify dominant solutions. The dominant solution for the capsule design can be determined by minimizing cost, power, and mass of the PS, while preserving similar capsule's performances. In this respect, the key performance indicator is given by the trajectory travel-time. Reducing the power of the PS implies both reducing its cost and mass and increasing the trajectory travel-time. Hence, the dominant solution can be determined by looking at the values assumed by the quantity  $O_1 = \frac{\max(P_{traction})}{TravelTime}$ . This auxiliary quantity helps us to identify a dominant solution (for the minimum value of  $O_1$ ) that is for:

- $L = 226km$ , for  $w = 100$ ,  $O_1 = 0.101 \frac{MW}{min}$
- $L = 500km$ , for  $w = 100$ ,  $O_1 = 0.047 \frac{MW}{min}$
- $L = 1000km$ , for  $w = 100$ ,  $O_1 = 0.025 \frac{MW}{min}$

We can consider another auxiliary quantity in order to identify a different dominant solution. This additional auxiliary quantity takes into consideration the energy consumption with respect to the travel time, hence we can define the auxiliary quantity  $O_2 = \frac{Energy}{Distance \cdot Passenger \cdot TravelTime}$  which is minimal for:

- $L = 226km$ , for  $w = 100$ ,  $O_2 = 1.14 \frac{Wh}{km \cdot passenger \cdot min}$
- $L = 500km$ , for  $w = 100$ ,  $O_2 = 0.371 \frac{Wh}{km \cdot passenger \cdot min}$
- $L = 1000km$ , for  $w = 100$ ,  $O_2 = 0.149 \frac{Wh}{km \cdot passenger \cdot min}$

These metrics enable us to conclude that for any different considered length, the optimal solution is found for  $w = 100$ . These results are also similar with the one presented in the Results section. Namely, for a lower power sizing of the capsule's PS, lower energy consumption/passenger/km and larger travel time, the  $O_1$  and  $O_2$  metric shrinks down.

### 2.3.6 Sensitivity Analysis

In the subsection discussing the dominant solutions, the solution corresponding to  $w = 100$  appears to represent the best trade-off between the performance and cost of the PS. In this subsection, we verify the sensitivity of this dominant solution with respect to the variations of parameters that might exhibit changes in the design stage of the capsule. We specifically refer to  $k_1 + k_2$  and  $m_0$ . The reasons of using these two metrics on the sensitivity analysis are: (i) for  $m_0$ , other capsule's equipment is not considered in the original value assumed for this parameter and (ii) by considering a passive cooling system for the VSI and LIM,  $k_1$  and  $k_2$  may present higher values.

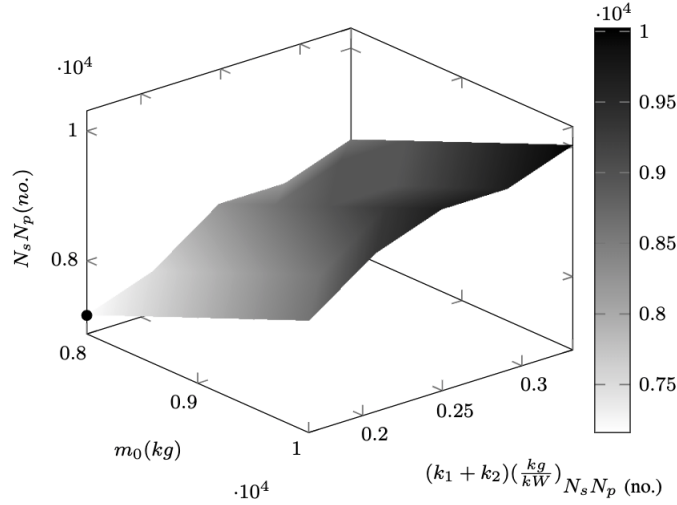


Figure 2.16: Number of cells sensitivity analysis (for  $w = 100$ ).

The sensitivity analysis is carried out for  $w = 100$ , by solving (2.14) varying  $k_1 + k_2$  and  $m_0$  above their initial values. The ranges of these parameters used in this analysis are  $(k_1 + k_2)_{init} \rightarrow 2(k_1 + k_2)_{init}$  and  $m_{0,init} \rightarrow \frac{5}{4} \cdot m_{0,init}$ . Fig. 2.16 and Fig. 2.17 show the modifications of the BESS total number of cells and trajectory travel time. As it can be seen from these two figures, the solutions vary in a continuous way. For the largest values of  $(k_1 + k_2)$  and  $m_0$  with a fixed length of trajectory,  $L = 226 \text{ km}$ , the average traveling time is reduced by one minute (i.e., 5%), with respect to the value obtained with the original solution. This result is due to an increase of the BESS number of cells in the range of 10%, with respect to the original optimal solution.

## 2.4 Extension with a different battery cell model

©2020 IEEE

Reprinted, with permission, from: D. Tudor and M. Paolone, "Influence of Battery Models on the Optimal Design of the Propulsion System of a hyperloop Capsule," 2019 IEEE Vehicle Power and Propulsion Conference (VPPC), January 2020.

### 2.4.1 Introduction

One of the fundamental aspects in the design of a hyperloop transportation system lies in the optimal assessment of the energy reservoir that capsules need to carry along with the characteristics of its PS. It is worth noting that the modelling of the cell plays an important role to define the size of the BESS.

This Section assesses the influence of equivalent circuit battery models on the optimal design

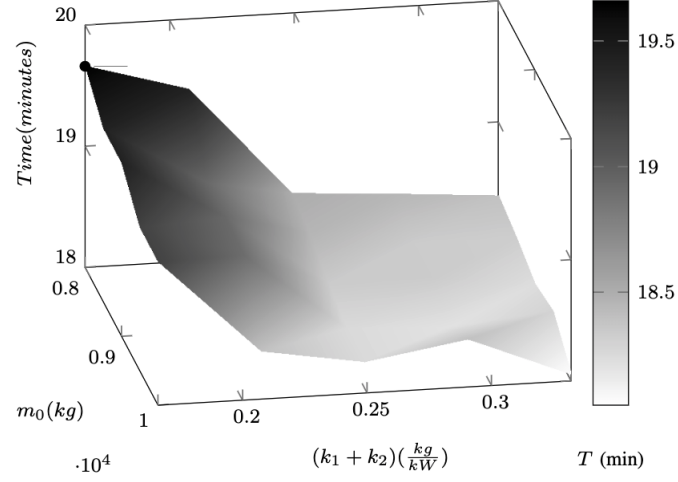


Figure 2.17: Trajectory traveling time sensitivity analysis (for  $w = 100$ ).

of the propulsion system of an energy-autonomous hyperloop capsule.

To fix ideas, the same problem (2.14) has been solved, but with a different battery cell model and the results are compared with respect to the initial cell model shown in Fig. 2.3.

#### 2.4.2 Cell Models and Formulation of the Optimization Problems

Let us recall the initial model of the cell used in (2.14) as in Fig. 2.3 to be considered (*Cell Model 1*). This model is the simplest one, but it is computational-effective when applied to optimization problems as it contains a single state variable given by the SoC.

The second model (*Cell Model 2*) of the battery cell is the well-known two (or multiple) time constant (TTC) model capable to capture the charging/discharging and redistribution phases. The equivalent circuit of the TTC model is shown in Fig. 2.18 and its mathematical model in the state space form in (2.23) (e.g., [48]).

$$\begin{bmatrix} \dot{U}_{C_1} \\ \dot{U}_{C_2} \\ \vdots \\ \dot{U}_{C_p} \end{bmatrix} = \begin{bmatrix} \frac{1}{R_1 C_1} & 0 & \dots & 0 \\ 0 & \frac{1}{R_2 C_2} & \dots & 0 \\ 0 & \dots & \dots & 0 \\ 0 & 0 & \dots & \frac{1}{R_p C_p} \end{bmatrix} \cdot \begin{bmatrix} U_{C_1} \\ U_{C_2} \\ \vdots \\ U_{C_p} \end{bmatrix} + \begin{bmatrix} \frac{1}{C_1} \\ \frac{1}{C_2} \\ \vdots \\ \frac{1}{C_p} \end{bmatrix} \cdot I_{cell} \quad (2.23)$$

where:  $U_{C_1}, U_{C_2}, \dots, U_{C_p}$  are the voltages of the RC series branches (i.e., new additional states of the model);  $C_1, C_2, \dots, C_p$  are the capacitors of the RC branches;  $I_{cell}$  is the current flowing through the cell;  $R_0$  is the ESR of the cell and cell's terminals connections.

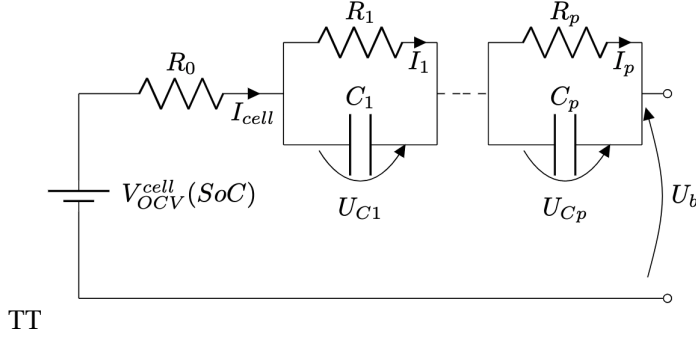


Figure 2.18: Cell Model 2: second equivalent circuit of a cell used to derive the BESS constraints (in general, the TTC model can contain multiple RC series branches in order to improve its capability to model the charge diffusion).

The cell accessible voltage provided by the TTC model,  $U_b$ , is given by (2.24).

$$U_b = V_{OCV}^{cell}(SoC) - R_0 I_{cell} - \sum_{i=1}^p U_{C_i} \quad (2.24)$$

In the second approximation, the model of an entire BESS pack composed by identical cells can mathematically be described by (2.25).

$$\begin{cases} V_{OCV}^{batt} = f(SoC) \\ V_{OCV}^{batt} = V_{OCV}^{cell} N_s \\ I_{batt} = I_{cell} N_p \\ SoC = SoC(0) + \int_0^t \frac{I_{batt}}{C_{batt}} dt \end{cases} \quad (2.25)$$

Hence,  $V'_{batt}$  and  $P'_{batt}$ , are the accessible voltage and power of the BESS (2.26) for *Cell Model 2*.

$$\begin{cases} V'_{batt} = N_s (V_{OCV}^{cell}(SoC) - R_0 I_{cell} - \sum_{i=1}^p U_{C_i}) \\ P'_{batt} = I_{batt} V'_{batt} \end{cases} \quad (2.26)$$

Therefore, the optimization problem has been solved with the *Cell Model 1* as in (2.14) and with the *Cell Model 2*. The main objective of this comparison is to quantify the impact of using a simple, but time-effective cell model with one which is closer to reality, but more computationally demanding in view of the increased number of state variables. It is worth noting that the main results that can potentially be affected are related to the mass of the capsule and maximum instantaneous power along the trajectory delivered by the BESS and,

as consequence, by the PS. The constraints of the optimization problem remain the same with the exception of the cell model as explicitly mentioned in (2.27).

$$\begin{aligned}
 & \min_{N_s N_p, a} \quad N_s N_p - w \cdot \|a(x)\|_2 \\
 & \text{subject to} \quad [\text{constraints as in (2.14)}] \\
 & \hline
 & \text{Cell Model 1:} \quad (2.2), (2.3) \quad \text{Cell Model 2:} \quad (2.23), (2.24), (2.25), (2.26) \\
 & P_{traction} \leq \eta P_{batt} \quad \text{or} \quad P_{traction} \leq \eta P'_{batt}
 \end{aligned} \tag{2.27}$$

### 2.4.3 Numerical Assumptions and Results

#### Numerical Assumptions

The numerical assumptions of the optimization problems are the same as the ones above-mentioned in the actual chapter. In this section, only one length of trajectory has been used to solve the optimization problem (i.e.,  $L = 226 \text{ km}$ ).

Regarding the *Cell Model 2*, two RC branches have been chosen additionally to the initial ESR (*Cell Model 1*) as shown in Fig. 2.19.

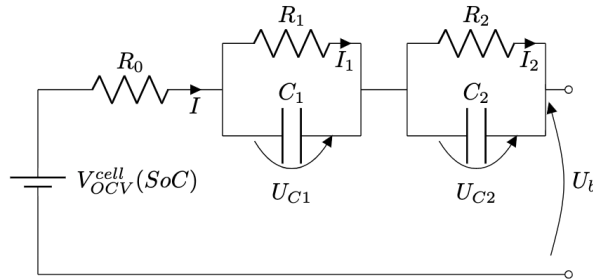


Figure 2.19: Cell Model 2: second equivalent circuit of a cell adopted to derive the BESS constraints.

The chosen cell is the same (i.e., Kokam SLPB 11543140H5) as initially used. It is worth re-noting that its parameters have been fully-characterized at the EPFL, DESL laboratory. Regarding the maximum value of  $V_{OCV}^{batt}$  this is chosen based on [44], therefore  $V_{OCV}^{batt} = 1.5 \text{ kV}$  for  $SoC_{max} = 100\%$ . The other limits are given in (2.28).

$$\left\{ \begin{array}{l} SoC_{max} = 100\% \\ SoC_{min} = 10\% \\ R_{cell} = R_0 = 4.4m\Omega \\ R_1 = 12.2m\Omega \\ C_1 = 7380.96F \\ R_2 = 1.3m\Omega \\ C_2 = 2370.78F \\ m_{cell} = 0.128kg \\ I_{cellMax} = 150A \\ I_{cellMaxcharge} = 5A \end{array} \right. \quad (2.28)$$

## Results

The problems stated in (2.27) have been solved under the same initialization conditions. The mapping of the control variables initialization is the same as in Algorithm 1 for both cell models. By using Algorithm 1, the following figures represent the two different fronts corresponding to the *Cell Model 1* and *Cell Model 2* of BESS as a function of  $w$  (for each  $w$ , the obtained solutions represent the best minimum for (2.27) given by the several initializations). Fig. 2.20 shows the capsule and BESS masses, Fig. 2.21 and Fig. 2.22 the maximum speeds and accelerations achieved along the trajectory, Fig. 2.23 the maximum traction powers and Fig. 2.24 the average times necessary to cover the trajectory with the two different cell models.

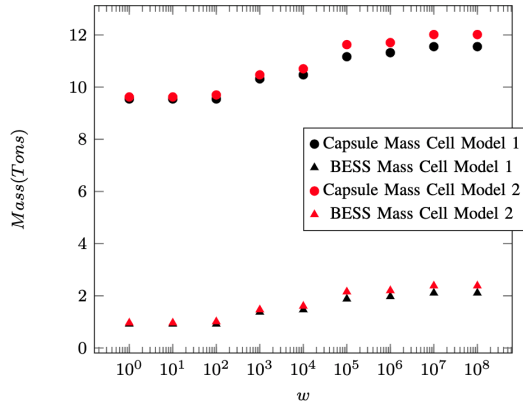


Figure 2.20: Capsule and BESS masses.

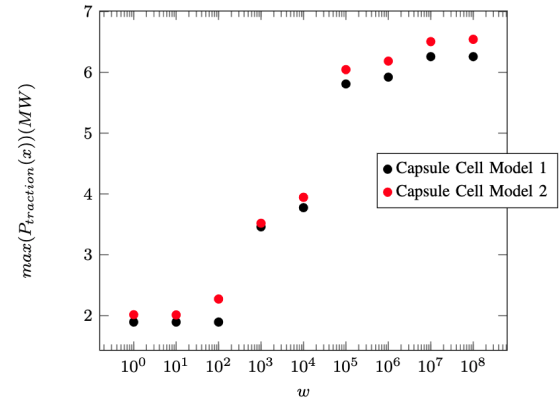


Figure 2.23: Maximum traction power provided by the capsule propulsion system.

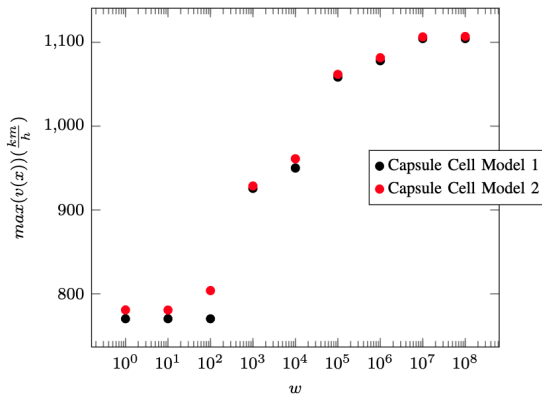


Figure 2.21: Maximum speed along the trajectory.

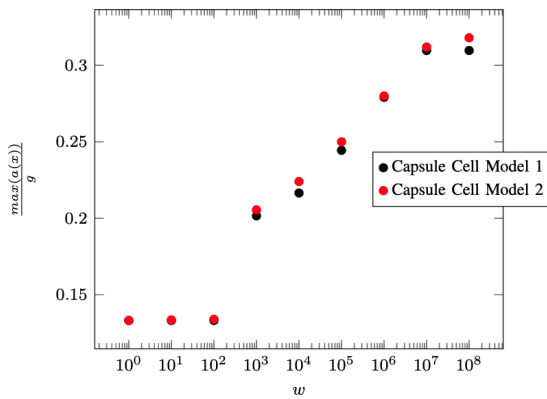


Figure 2.22: Maximum acceleration along the trajectory (values in per-unit to g).

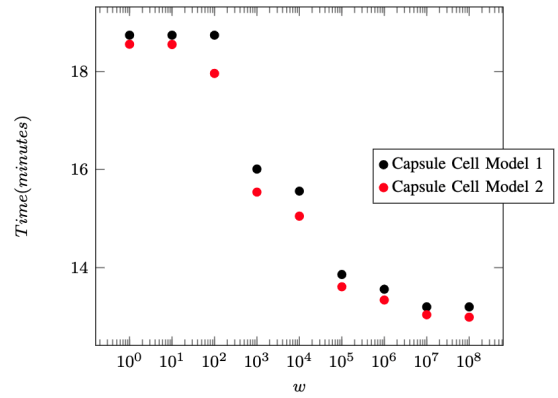


Figure 2.24: Time necessary to cover the trajectory.

## 2.4.4 Discussions

### General Observations

Nine different capsule-PS solution spaces for every cell model were generated depending on the value of  $w$ . The nine solutions represent various trade-off between the average traveling time and energy consumption or maximum required instantaneous power.

Irrespectively of the value of  $w$  or the cell model, it is interesting to observe that the obtained BESS masses and the total number of cells are compatible with the currently proposed applications in commercial heavy-duty electric vehicles (e.g., electric trucks). The same observation applies to the maximum powers obtained for the other elements of the capsule propulsion. Therefore, the results indicate the technical feasibility of the identified capsule propulsion using today's available technologies.

Indeed, in a range of  $[0.9, 2]$  tons for *Cell Model 1* and  $[0.95, 2.4]$  tons for *Cell Model 2* of battery cells (Fig. 2.20), most of the mass is still distributed to the mechanical sub-systems and for the payload. The amount of maximum power necessary to transport a payload of 25 people is in the range of  $[2, 6.5]$  MW for *Cell Model 1* and in the range of  $[2.1, 6.6]$  MW *Cell Model 2*. In Fig. 2.24, the average traveling time stays in the range of  $[13, 19]$  minutes for both cell models, where the upper boundary of this range is constrained by the optimization problem and is governed by the lower values of  $w$  ( $w = \{1, 10, 100\}$ ). Indeed, the average traveling time (Fig. 2.24) is related to the maximum speed over the trajectory (see Fig. 2.21) and the acceleration profile, where every maximum point, with respect to  $w$ , can be found in Fig. 2.22.

As a final remark, it is worth computing the capsule's energy consumption/km/passenger. The results are shown in Fig. 2.25 and we have assumed a BESS charging efficiency  $\eta_{charging} = 89.4\%$  [45]. This estimation refers to the both cell models and only to the energy consumption of the capsule and does not include any vacuuming process.

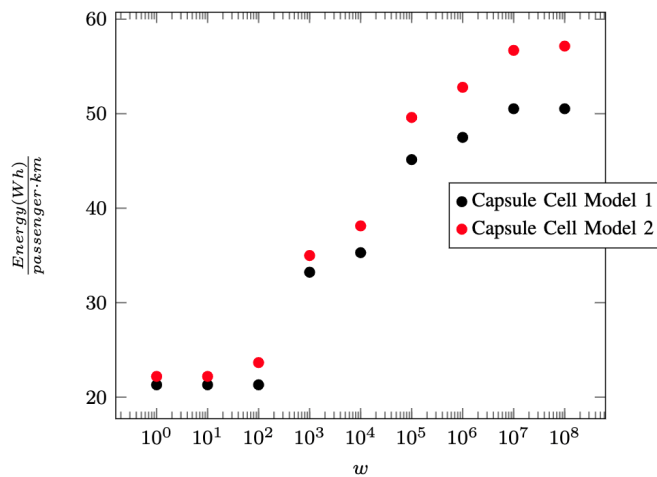


Figure 2.25: The energy consumption per passenger per km.



### Dominant Solutions

The dominant solution for the capsule PS should be identified by looking at solutions preserving capsule's performances. Hence the first metric to be used to identify a dominant solution can be represented by:  $O_1 = \frac{\max(P_{traction})}{TravelTime}$ . This quantity is minimal for  $w = 1$ , and the value of  $O_1 = 0.101 \frac{MW}{min}$ .

The auxiliary quantity to identify a potential different dominant solution takes into account the energy consumption with respect to the travel time:  $O_2 = \frac{Energy}{Distance \cdot Passenger \cdot TravelTime}$  which is also minimal for  $w = 1$  (with  $O_2 = 1.11 \frac{Wh}{km \cdot passenger \cdot min}$ ).

The optimal values,  $O_1$  and  $O_2$ , regard the *Cell Model 1*. The analogy for the *Cell Model 2*, which eventually creates  $O'_1$  and  $O'_2$ , coincides with the same  $w$  value ( $w = 1$ ). Therefore, for both cell models, the dominant solutions could be found at  $w = 1$ .

### Final Observations on the Influence of Cell Models

The Algorithm 1 was applied for both aforementioned cell models. The *Cell Model 2* generally results in BESSs characterized by higher values of the energy-reservoir compared to *Cell Model 1*. The additional weight of cells is in a range of [4, 12.5]% as shown in Fig. 2.26. The computation has been made for every  $w$ . Nevertheless, it is worth observing that the average time travel is slightly reduced. Along with the mass of the BESS associated to *Cell Model 2*, the energy consumption/km/passenger is increased by a maximum of 12.2% for higher values of  $w$ . For lower values of  $w$ , the differences between the energy consumption/km/passenger term are not relevant as the BESS masses do not exceed a 4% relative difference.

The impact of the *Cell Model 2* is evident, and it independently results in a larger BESS mass. Larger BESS masses associated to the usage of *Cell Model 2* were expected as this model results in larger voltage variations compared to *Cell Model 1*.

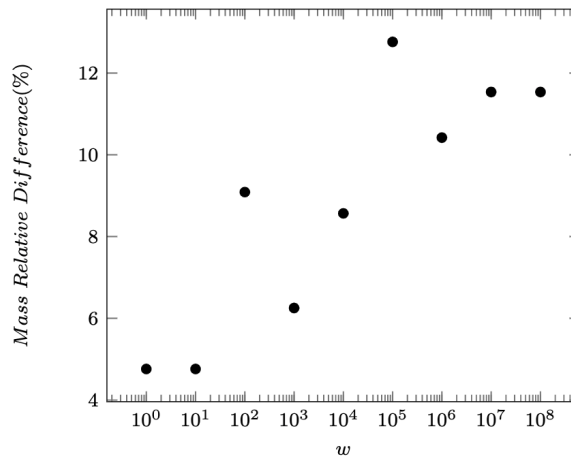


Figure 2.26: BESS relative difference depending on the battery cell model.

## 2.5 Conclusions

In this chapter, we have proposed a specific optimization problem for the design of the PS of a hyperloop capsule with a simplified model of aerodynamics and independent of the infrastructure's limitations. The problem's objective-function is composed by the number of cells of the BESS that supply the capsule propulsion and the performance of the capsule given by the norm-2 of the array of the space-discretized accelerations along the capsule trajectory. The constraints rely on numerically tractable models of the three elements composing such a PS, as well as the kinematic model of the capsule. The problem has been solved in 2 independent ways using two different battery cell models.

The chapter presented a comprehensive analysis of the results that demonstrated the technical feasibility of the hyperloop PS with respect to existing BESS and electrical propulsion technologies. Furthermore, the proposed design method enables to compute energy consumption of the capsule's propulsion between 10 to 57.15 Wh/km/passenger depending on the assumptions, trajectory parameters and cell model. With the proposed sizing method and hyperloop capsule architecture, we estimate that today's battery and power-electronics technologies exhibit characteristics that might be compatible with the hyperloop application, thus enable its development as a potential viable transportation solution. However, a study regarding the safety of the system and how the safety can affect the sizing of the BESS and PS is not considered, therefore, future research is needed. In the next chapter, the proposed optimization framework is further complexified towards an operational-driven optimal-design framework of the entire hyperloop system.

## 3 Operational-Driven Optimal-Design of a Hyperloop System

Reprinted, with permission: Denis Tudor, Mario Paolone, "Operational-driven optimal-design of a hyperloop system", *Transportation Engineering Journal*, September 2021.

In this chapter, we present an operational-driven optimal-design framework of a hyperloop system. The novelty of the proposed framework is in the problem formulation that links the operation of a network of hyperloop capsules, the model of the hyperloop infrastructure, and the model of the capsule's propulsion and kinematics. The objective of the optimisation is to minimize the energy consumption of the whole hyperloop system for different operational strategies. By considering a network of energy-autonomous capsules and various depressurization control strategies of the hyperloop infrastructure, the constraints of the optimisation problem represent the capsule's battery energy storage system response, the capsule's propulsion system and its kinematic model linked with the model of the depressurization system of the hyperloop infrastructure. Depending on the operational scheme and lengths of the trajectories, the proposed framework determines optimal operating pressures of the hyperloop infrastructure between  $1.5 - 80\text{ mbar}$  along with the maximum capsules cruising speeds. Furthermore, the proposed framework determines maximum operational power of the capsule's propulsion system in the range between  $1.7 - 5\text{ MW}$  with a minimum energy need of  $25\text{ Wh/passenger/km}$ .

### 3.1 Introduction and Literature Review

The hyperloop transportation system comprises a set of capsules traveling at (almost) sonic speed in a constrained space characterized by a low-pressure environment (i.e., a tube) housing a dedicated set of rails that enable the capsules' guidance, levitation and/or suspension. The hyperloop is characterised by higher speeds, compared to existing ground transportation systems and, due to the large reduction of the drag aerodynamic losses, can require lower energy needs with respect to electric trains and intra-continental aircrafts. Since 2015, when the research activity on the hyperloop system was relaunched, very few manuscripts have addressed the problem of the optimal design of this very peculiar transportation system. The

very first technical question was whether the hyperloop capsules can be designed to be energy-autonomous in order to avoid the electrification of the rail with the obvious consequences on the simplification of the tube design and cost. In Chapter 2, this question has been addressed by proposing an optimisation framework capable of designing the propulsion system (PS) of a hyperloop capsule that is supplied by a battery energy storage system (BESS). However, the approach proposed in Chapter 2 did not take into consideration the energy needs of the tube (i.e., associated with its depressurization) nor the impact of the hyperloop tube operation on the total energy consumption and the associated capsule PS design. Indeed, in order to minimise the overall energy needs of both the capsules' PS and tube depressurization, the operation of the hyperloop infrastructure (i.e., the tube operational pressure, the interval between subsequent depressurization processes, as well as the number of capsules occupying the tube per day) could be coupled with the capsule's PS optimal design. Furthermore, the operation of the infrastructure and the capsules' PS design could change as a function of the length of the tube, and determining whether this is the case is a technical question that deserves to be addressed.

Therefore, there are five fundamental questions that need to be addressed. (i) What is the optimal operating pressure inside a hyperloop tube in order to minimize its global energy consumption ? (ii) What is the achievable minimal energy consumption of a hyperloop system ? (iii) Is there a strong dependency between the infrastructure operation and capsule's PS design ? (iv) Which is the impact of the magnetic levitation on the energy consumption of the capsule ? (v) Can a compressor increase the energy efficiency of a hyperloop system?

Although the existing literature has not yet produced specific contributions to address these questions, it has produced a number of publications that addressed similar problems. Indeed, it is worth observing that the design of a hyperloop system presents similarities to an inverted Maglev train (the rail of the Maglev is the main source of power generating the capsule thrust). In [49], [50] and [51], other researchers have shown how the main characteristic of Maglev levitation and guidance systems can be determined by solving a suitable optimization problem. In [51] and in [52], Cassat and Jufer studied how the propulsion and energy transfer to an in-motion vehicle can be jointly modeled in order to be suitably optimised. The operational performance and safety standards for Maglev system have been further studied in [53] by Cassat and Jufer.

Publications addressing the problem of the design of wireless energy-transfer systems into in-motion vehicles are also worth mentioning: in [54] by other researchers, this type of systems is studied for vehicles that host a BESS and travelling at atmospheric pressure. An economic viability and environmental study about wireless power transfer is presented in [55] by Limb.

In [57], He proposed a multiobjective co-optimization problem for a vehicle with a hybrid power supply with the main purpose of improving the energy efficiency of the vehicle propulsion system along with its ride comfort. As a result, a Pareto front is obtained to analyse the best compromise solutions between the power consumption and ride comfort.

A hybrid power supply system of an electric train is discussed in [58] by other researchers, where the BESS has the role of a dedicated energy buffer for transferring power between the kinematic energy stored in the train and its regenerative braking system. The model also contains a dissipative braking system due to the limited energy capacity of the on-board BESS. The proposed design determines the best trade-off between the optimal BESS capacity, energy-saving rate, volume of the system, capital cost, maximum power and mass of the train.

Note that none of the aforementioned manuscripts presents a complete framework that can be used to address the hyperloop-specific questions listed above. In this respect, the original contribution in this chapter is to fill this gap by proposing a non-convex and non-linear optimization framework. The multi-objective function of the proposed optimization targets the minimization of the total energy consumption of the hyperloop system (composed by the capsules' and tube's depressurization energy needs), which is subject to a comprehensive set of constraints modeling in detail the hyperloop capsule's kinematic, and its PS, the tube depressurization process, leaks compensation, and the operation of the hyperloop system.

The structure of this chapter is the following: In Section 3.2, we illustrate the model of the hyperloop infrastructure where the energy consumption of the vacuum pumps (both for the initial depressurization process and air leaks compensation) is taken into account with the model of the energy consumption of a network of capsules travelling on a trajectory of generic length. We also represent the operation of the whole infrastructure. In the Section 3.3, we propose the optimization framework targeting the minimization of the global energy need of the hyperloop system subject to the capsule's infrastructure and operational constraints illustrated in Section 3.2. In Section 3.4, we present a numerical example used to obtain the results discussed in Section 3.5. We complete this last sections with a comprehensive analysis related to the average energy consumption (Wh/passenger/km). In Section 3.6, we conclude the chapter with a summary of the findings.

## 3.2 Hypotheses and Models

The impact on the energy consumption of capsule's auxiliary systems, such as heating, ventilation, and air conditioning (HVAC), passengers entertainment and safety systems is not considered in this chapter.

### 3.2.1 Model of the Hyperloop Infrastructure

In order to model the operation of the hyperloop system, we represent two processes: (i) the depressurization that refers to the decrease of the pressure inside the hyperloop tube from the atmospheric pressure,  $p_0$ , to the desired one,  $p_{tube} (< p_0)$ , and (ii) the compensation of the air leaks in order to maintain the pressure  $p_{tube}$  as the material used to manufacture the tube is assumed to not be perfectly airtight. The depressurization and leak compensation processes are considered independent (see Section II.C for further details).

The system is supposed to have available a total number of vacuum pumps, say  $q'$ , between Stations A and B of the hyperloop tube. All the  $q'$  pumps are used for the depressurization process and a subset of them, say  $q''$ , is used to compensate the air leaks. In view of the different air volumes that these pumps have to process, the need for  $q'' \leq q'$  is obvious. Fig. 3.1 provides a schematic view associated with the assumptions reported above.

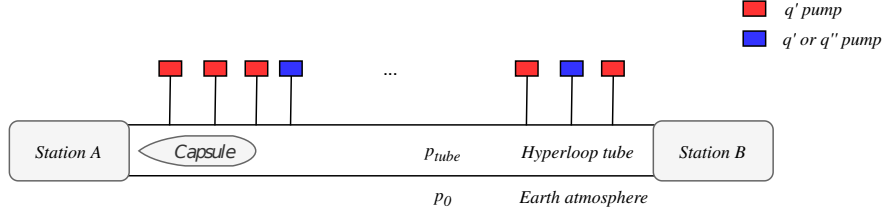


Figure 3.1: Schematic view of the hyperloop infrastructure's depressurization system.

As shown in Fig. 3.2, the parameters of the tube geometry are as follows:  $L$  is the length of the hyperloop tube,  $\lambda$  represents the thickness of the tube,  $d_{in}$  corresponds to the inner diameter of the tube, and  $d_{out}$  represents the outer diameter of the tube, with  $d_{out} = 2 \cdot \lambda + d_{in}$ . The inner cross section of the tube is simply  $S_{tube} = \pi(\frac{d_{in}}{2})^2$ .

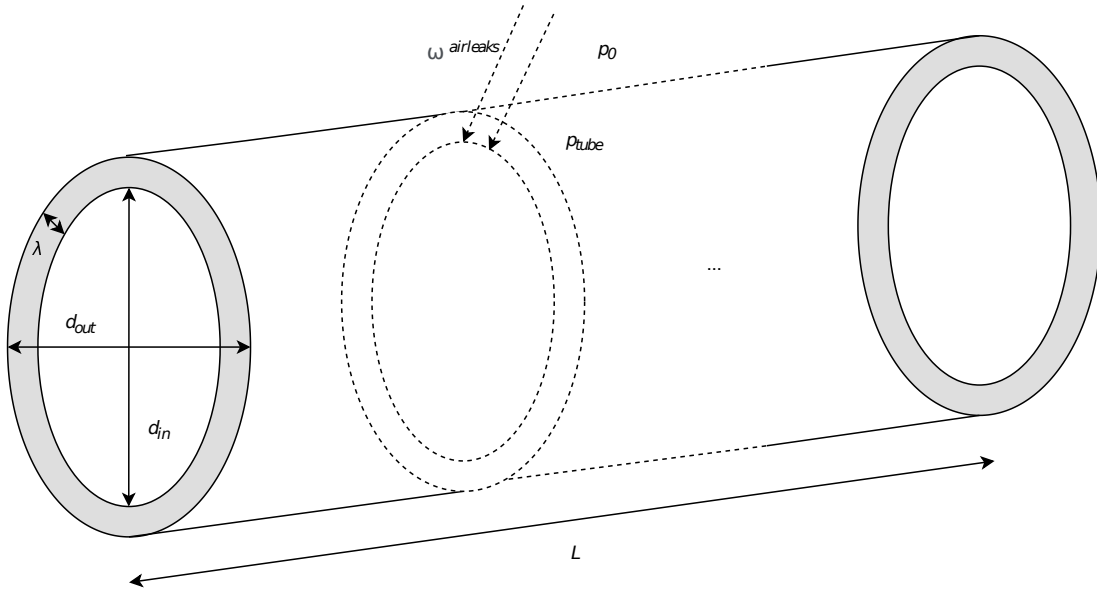


Figure 3.2: Simplified geometry of the hyperloop tube (side view).

The  $q'$  pumps are expected to operate periodically when the hyperloop tube needs to be completely depressurized, starting from the atmospheric pressure  $p_0$ . This period of time is named  $T_{depr}$ . Assuming the depressurization process to be an adiabatic thermodynamic transformation, we can easily compute the time necessary,  $\tau_d$ , to bring the hyperloop tube pressure from its initial value,  $p_0$ , to the final one,  $p_{tube}$  shown by other researchers in [59]-[61]. This computation is expressed by (3.1) where  $\omega^{pump}$  represents the pumped-air volume

flow expressed in  $[\frac{m^3}{h}]$ , usually a known quantity from the pump's manufacturer expressed as a function of the pressure.

$$\tau_d = \frac{\pi \cdot (\frac{d_{in}}{2})^2 \cdot L}{q' \cdot \omega^{pump}(p_{tube})} \cdot \ln\left(\frac{p_0}{p_{tube}}\right) \quad (3.1)$$

Equation (3.2) quantifies the energy needed for the depressurization of the hyperloop tube between subsequent maintenance periods<sup>1</sup>, where  $P_{pump}$  represents the power of a single vacuum pump (during the operations, the pump's power is constant).

$$E_{depr} = q' \cdot P_{pump} \cdot \tau_d \quad (3.2)$$

By referring to a daily operation horizon (i.e., 24h) of the hyperloop tube, we assume the capsules to be launched within an operation period named  $T_{op}$ . Therefore, it is reasonable to impose the following inequality  $\tau_d \leq 24hours - T_{op}$  as we might want the initial depressurization process to be finalised in a relatively short time and, then, to start the scheduled operation.

The next step is to determine a model of the hyperloop air leaks. The material used to build the hyperloop tube should be characterized by a known air permeability. In view of the evident impact that the tube material has on the hyperloop infrastructure cost, we consider the case of concrete as strongly advocated in [62] by Heller and we assume its permeability to be isotropic. The use of concrete corresponds to a worst-case scenario regarding the influence of tube's air leaks. On the contrary, the use of steel tubes defines the situation where the corresponding air-permeability is close to zero. However, steel tubes presents the main disadvantage represented by the associated cost of the infrastructure. In view of the above, here below we mainly refer to the case of concrete tubes and the reader may refer to the sensitivity analysis regarding the air permeability of the tube's material shown in Section 3.5.

The material and fluid parameters taken into account to estimate the leaks are  $k_{perm}$ , which represents the concrete's air permeability, and  $\mu$ , which corresponds to the dynamic air viscosity.

In order to compute the energy needed to compensate for the air leaks, we need to express the air-leak volumetric flow rate,  $\omega^{airleaks}$ . This quantity can be estimated using the Darcy's law, assuming the compressible characteristic and the radial bidirectional air flow. According to [59]- [61], the air leaks volumetric flow rate is given by (3.3).

<sup>1</sup>We suppose that, during the hyperloop operation, the tube is always depressurized (i.e., for several days/weeks). The maintenance period corresponds, therefore, to a halt of the tube where its pressure is back to the atmospheric one.

$$\omega^{airleaks} \left[ \frac{m^3}{h} \right] = - \frac{3600 \cdot \pi \cdot k_{perm} \cdot L \cdot (p_{tube}^2 - p_0^2)}{\mu \cdot \ln(1 + \frac{\lambda}{d_{in}}) \cdot p_{tube}} \quad (3.3)$$

To compensate for the air leaks, we need to activate  $q''$  pumps in order to satisfy the following inequality  $\omega^{airleaks} \leq q'' \cdot \omega^{pump}$ . The daily energy needs to supply the  $q''$  pumps,  $E_{pr}$ , is given by (3.4), where  $t_{leaks}$  represents the time the air leakage is occurring. As we are modeling the operation of the hyperloop tube over a 24h horizon,  $t_{leaks} = 24hours$  because leaks are always present.

$$E_{pr} [J/day] = q'' \cdot P_{pump} \cdot t_{leaks} \quad (3.4)$$

The energy required to operate the hyperloop tube is expressed by  $E_{depr}$  (needed between two subsequent complete depressurization periods) and  $E_{pr}$  (daily need). These two quantities are used next within a suitably defined optimization problem that enables us to assess the optimal parameters associated with the hyperloop propulsion and the optimal parameters associated with the operation of the hyperloop tube along a given time horizon. It is worth noting that the energy consumption corresponding to tube operations may be supplied by a renewable source of energy such as photo-voltaic (PV).

### 3.2.2 Model of the Hyperloop Capsule

The operation of a hyperloop system involves the launching of several capsules travelling in series in the same tube. This operation is required as the number of passengers per capsule is limited to a few dozen. Hence, a set of travelling hyperloop capsules in the above-mentioned tube is considered, where  $r_{caps}$  represents the number of launched capsules per unit of time. A detailed model of the capsule propulsion can be found in Chapter 2 and the main equations can be found in this section, as they are used in the optimization problem proposed here.

#### Trajectory

The trajectory of one capsule is presented in Section 2.2.1, Chapter 2 and it is traveled by a network of capsules (see Fig. 3.3).

#### The Model of the Capsule Propulsion System

As in Chapter 2, the hyperloop PS is assumed to be composed by three main components: (i) an energy reservoir represented by a BESS, (ii) a DC/AC power electronic converter (usually a



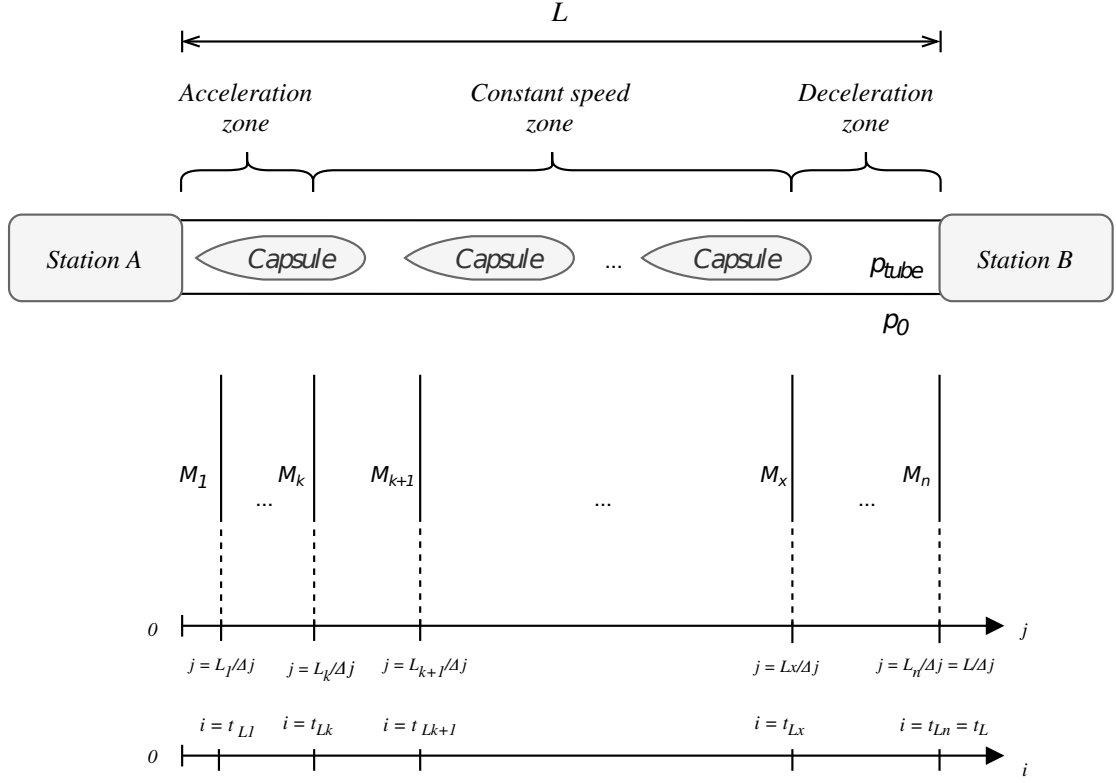


Figure 3.3: The generic trajectory of hyperloop capsules. Adapted from Fig.2.2

voltage source inverter (VSI)) and (iii) an electrical machine consisting of a linear induction motor (LIM) as studied by other researchers in [31]- [34].

a) Model of the BESS: the capsule's source of power is supposed to be a BESS that is modeled at the cell level. As discussed in Chapter 2, due to the numerical complexity and large number of equations and corresponding state variables, we choose a simple equivalent circuit of a cell where the charge diffusion dynamics are not taken into account as the obtained results are not affected by more sophisticated cell models [28] as shown by Einhorn et al. To fix ideas, in this chapter, the *Cell Model 1*, with the corresponding equations from Section 2.2.2, has been used in order to model the cell.

b) Propulsion: acceleration and speed profiles are dependent on the traction force, where the most important parameters are (as already stated in Section 2.2.2):

- $\frac{P}{PS_{weight}}$  which represents the ratio between the available propulsion power per unit mass.
- $V_{DC}^{max}$  which represents the maximum allowable DC voltage of the VSI.

### Capsule Kinematic Model

As in Section 2.2.3, the mass of the mechanics and payload,  $m_0$ , BESS,  $m_{BESS}$ , and PS represented by the VSI and LIM,  $m_{PS}$ , compose the total mass of one capsule,  $m = m_0 + m_{BESS} + m_{PS}$ .

The LIM and VSI are characterized by a given weight-per-unit input power density  $k_1 = \frac{m_{LIM}}{P_{LIM}}$  and  $k_2 = \frac{m_{VSI}}{P_{VSI}}$ , respectively. Thus, the final expression of total mass is given by (3.5), where  $m_0$  is constant and considered a passive mass,  $m_{cell}$  is the associated cell's mass embedding the unitary mass plus cells' wiring,  $\eta_{tr}$  represents the supplementary power transfer efficiency from BESS to LIM (i.e., the efficiency of the power electronics converter),  $\cos(\phi)$  is the power factor of the VSI and  $P_{maxCell}$  the maximum power provided by a cell. As mentioned in the Chapter 2, in order to determine the mass of the PS, we should consider the maximum output PS power given by the peak output power of the BESS multiplied with the traction system efficiency. However, there is an important observation to be made regarding the cooling of the PS. Indeed, capsules are traveling in an environment where the reduced pressure drastically compromise the heat exchange. First, it is interesting to note that the time spent by the capsules to travel hundreds of kilometers at subsonic speeds it is in the range of tens of minutes. These two observations may justify the decision to accumulate all the heat losses of the VSI and LIM in their masses. This design option may largely simplify a complex cooling system that in any case will be inefficient for pressures below hundreds of mbars. For these reasons, the mass of the PS is considered to be inverse proportional to its efficiency: in order to have larger mass for lower efficiencies of the VSI and LIM. Naturally, we have that  $m \sim N_s N_p$  who are two of the main control variables for the design of the capsule's PS. In order to keep the proposed optimisation problem tractable, these efficiencies and VSI power factor are assumed constant.

$$m = m_0 + N_s N_p m_{cell} + \frac{1}{\eta_{tr}} P_{maxCell} N_s N_p k_1 + \frac{1}{\eta_{tr} \cos(\phi)} P_{maxCell} N_s N_p k_2 \quad (3.5)$$

The kinematic model of the capsule is represented by the acceleration,  $a$ , and the speed,  $v$ , both sampled at every  $\Delta j$  (or  $\Delta i$  since these two indexes have a unique 1:1 correspondence). The trajectory length is  $L$  divided into three main zones: acceleration, constant speed, and braking zones; with a total number of discrete points  $\lceil \frac{L}{\Delta j} \rceil$ , considering  $\Delta j \ll L$  as in Chapter 2.

Again, the capsule is subjected to two main forces: the traction provided by the propulsion, and the aerodynamic drag force. The latter is given by (3.6), where  $\rho$  is the fluid density,  $C_d$  represents the capsule's drag coefficient, and  $S$  is the cross section capsule's surface.  $C_d$  is function of  $v$ , as discussed in [63] by Kang et al.

$$F_{dr}(j) = \frac{1}{2} SC_d(v) \rho v(j)^2 \quad (3.6)$$

The traction force and mechanical traction power,  $F_{tr}$  and  $P_{tr}$ , respectively, are given in (3.7) by using a mono-dimensional Newtonian kinematic model of the capsule.

$$\begin{cases} F_{tr}(j) = ma(j) + F_{dr}(j) \\ P_{tr}(j) = (ma(j) + F_{dr}(j)) \cdot v(j) \end{cases} \quad (3.7)$$

The levitation drag of the capsule may be considered to be null due to a potential usage of a suspended capsule solution as mentioned in [64]. In practice, a drag-less magnetic levitation can be realized by using in the capsule's propulsion system a Single Sided Linear Induction Motor (SSLIM). Indeed, a SSLIM may provide the necessary thrust and levitation force with no magnetic drag. Nevertheless, the presence of a magnetic levitation system is analyzed in the Section 3.5 in order to quantify the effects of the magnetic levitation drag on the power/energy requirements of the capsule propulsion system.

Through the reduction of the pressure inside of depressurized tubes, the hyperloop system reduces the density of the tube's fluid. The expression of  $\rho$  given by (3.8) assumes (i) the air to behave as an ideal gas, where  $\rho_0$  represents the fluid density at standard atmospheric conditions ( $\rho_0 = 1.225 \frac{kg}{m^3}$  for  $p_0 = 1.013 Bar$ , and  $T = 288.15 K$ ) and (ii) the operating temperature of the depressurized hyperloop tube to be equal to  $T = 288.15 K$ .

$$\rho = \frac{p_{tube}}{p_0} \cdot \rho_0 \quad (3.8)$$

The electrical power provided by the BESS,  $P_{batt}$ , is directly related with  $P_{tr}$  through the efficiency of the LIM,  $\eta_{LIM}$ , as in (3.9).

$$P_{batt}(j) = \frac{P_{tr}(j)}{\eta_{LIM}} \quad (3.9)$$

The total energy consumption for one capsule,  $E_c$ , is calculated in (3.10).

$$E_c = \int_0^{t_L} P_{batt} dt \quad (3.10)$$

Assuming a set of capsules traveling in the same tube and launched within a given period of time, we can define  $r_{caps}$  as the number of launched capsules in one day during the  $T_{op}$ . The total energy consumption per day of these capsules is simply  $E_{caps} = r_{caps} \cdot E_c$ .

### 3.2.3 Accounting for the Kantrowitz Limit to determine the upper-bound of capsules' speed

The study of a high speed capsule in a confined environment (i.e., tunnel or tube) implies compressibility effects. As capsules travel at high speed through a tube, they can choke the flow of the fluid in the area between the capsules' cross section,  $S$ , and the tube's cross section,  $S_{tube}$ . The assessment of the choke flow regime plays a major role in the determination of the maximum speed of the capsules,  $v_{max}$ , which is a fundamental constraint of the capsule kinematic model.

By making reference to the speed of sound,  $v_{sound}$ , in the air for a given temperature,  $T$ , we make use of the standard definition of the Mach number  $M_\infty = \frac{v_{max}}{v_{sound}}$ . Furthermore, we introduce the quantity  $S_{ratio} = \frac{S}{S_{tube}}$ .

We assume that the flow of the fluid around the capsule obeys the conventional isentropic gas equations. With this assumption, the limitation of the maximum capsule's speed results from the Mach number  $M_{lim} = 1$  of the fluid flow around the capsule, which represents the maximum value of the Mach number before the choke flow. Equation (3.11) allows to compute  $S_{ratio}$  as a function of  $M_\infty$ ,  $\gamma = \frac{c_p}{c_v}$  is the isentropic expansion factor of the gas in the tube environment and  $c_p$  and  $c_v$  represent the specific heats of the gas at constant pressure and volume. Therefore, (3.11) allows to link the cross-sectional dimensions of the tube/capsule with the maximum speed of the capsules to avoid the choke-flow regime to take place.

$$S_{ratio} = 1 - \frac{\frac{1}{M_{lim}} \left[ \frac{2}{\gamma+1} \left( 1 + \frac{\gamma-1}{2} M_{lim}^2 \right) \right]^{\frac{\gamma+1}{2(\gamma-1)}}}{\frac{1}{M_\infty} \left[ \frac{2}{\gamma+1} \left( 1 + \frac{\gamma-1}{2} M_\infty^2 \right) \right]^{\frac{\gamma+1}{2(\gamma-1)}}} \quad (3.11)$$

It is worth observing that the detrimental effects of pressure waves generated by a supersonic fluid between the capsules and the tube can be neglected since the maximum speed of the capsule enforced by (3.11) avoids the choke-flow regime to take place. This analysis has been shown by Kang and Ham in Fig. 7 and Fig. 8 of reference [63].

### 3.2.4 Hyperloop Infrastructure Operation

The energy needs of the whole hyperloop system is given by adding (i) the energy associated to the initial depressurization of the tube from  $p_0$  to  $p_{tube}$ , (ii) the energy needed to compensate the air leaks (i.e., to maintain  $p_{tube}$  inside the tube), and (iii) the energy used by the capsules'

PSs.

As we are interested in defining the operational parameters of the hyperloop infrastructure (essentially  $p_{tube}$ ) and the characteristics of its PS, which that minimize the whole hyperloop energy consumption, we need to define the ways to operate the infrastructure with respect to the vacuum pumps. We can identify two main ways to operate the infrastructure: (i) At the end of the daily operations, the  $q'$  pumps are shut down; hence, a new stage of tube depressurization to achieve  $p_{tube}$  is needed. (ii) The  $q''$  pumps continue to maintain the  $p_{tube}$  inside the tube independently of the operations. This option represents a relatively more advantageous solution with respect to the objective of minimizing the total energy consumption. Therefore, the nominal operation process involves an initial depressurization stage from  $p_0$  to  $p_{tube}$  including  $q'$  vacuum pumps, maintaining of the nominal pressure (parasitic air leakage in the tubes) at the level of  $p_{tube}$  and  $r_{caps}$  traveling per one direction per day during the  $T_{op}$ .  $E_{pr}$  is independent of  $T_{op}$  as the air leakage always occurs when  $p_{tube} \neq p_0$ . The entire operations process of the hyperloop system is periodical with the period  $T_{depr}$ , as shown by the operations' diagram of Fig. 3.4.

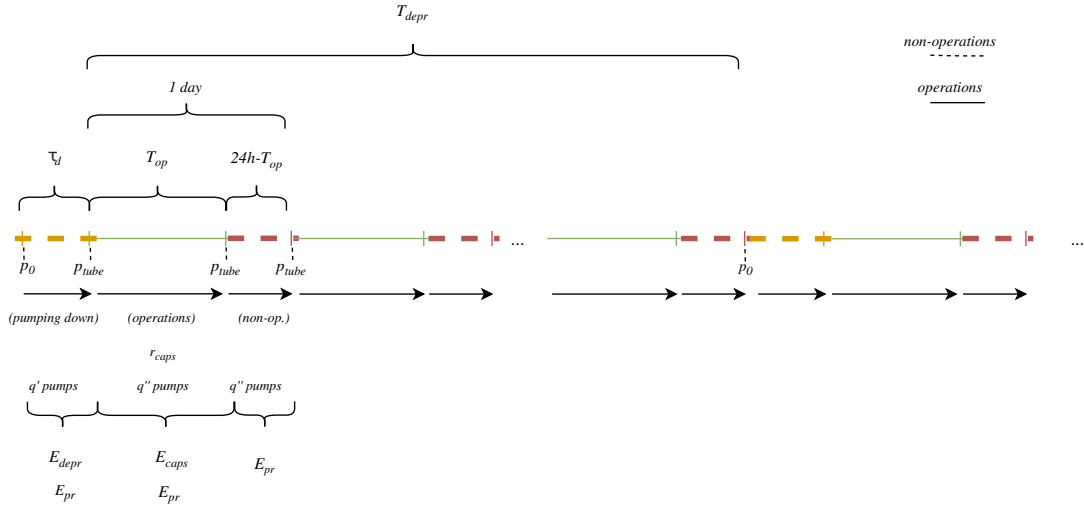


Figure 3.4: Operational scheme for the hyperloop infrastructure.

### 3.3 Formulation of the Optimization Problem

Given the model of the hyperloop infrastructure, capsules and operations, we formulate operational-driven optimal-design problem of the hyperloop system, as in (3.12). The objective function is to minimize total energy requirement of the whole hyperloop system. This is expressed by the objective  $E_{depr} + T_{depr}(E_{pr} + E_{caps})$ , where:

- $E_{depr}$  is the energy required by the  $q'$  pumps to depressurize the hyperloop tube between subsequent maintenance periods  $T_{depr}$  (expressed in days);

- $E_{pr}$  is the daily energy need of the  $q''$  hyperloop tube pumps compensating for the air leaks;
- $E_{caps}$  is daily energy need of the hyperloop capsules.

The decision variables of the problem are:

- $N_s$ : number of cells in series in the capsule's BESS;
- $N_p$ : number of cells in parallel in the capsule's BESS;
- $a$ : capsule acceleration along the trajectory;
- $p_{tube}$ : pressure inside the hyperloop tube;
- $q'$ : number of pumps of known rated power to depressurize the hyperloop tube;
- $q''$ : number of pumps of known rated power to compensate for the air leaks in the hyperloop tube.

$$\min_{N_s, N_p, a, q', q'', p_{tube}} E_{depr} + T_{depr}(E_{pr} + E_{caps})$$

subject to

$$j = 0, 1, 2, \dots, \frac{L_x}{\Delta j} - 1$$

$$v(j) \leq v_{max}$$

$$a_{min_{M_1}} \leq a(j) \leq a_{max_{M_1}},$$

$$\forall j = 0, 1, 2, \dots, \frac{L_1}{\Delta j} - 1$$

...

$$a_{min_{M_x}} \leq a(j) \leq a_{max_{M_x}},$$

$$\forall j = \frac{L_x-1}{\Delta j}, \dots, \frac{L_x}{\Delta j} - 1$$

$$t_{L_x} \leq T_{max_x}$$

$$SoC_{min} \leq SoC \leq SoC_{max}$$

$$N_{Smin} \leq N_s \leq N_{Smax}$$

$$\max(I_{cell}) \leq I_{cellMax}$$

$$V_{OCV}^{cell}(0) = V_{OCV}^{cell} | SoC = SoC_{max}$$

$$V_{OCV}^{batt} = V_{OCV}^{cell} N_s$$

$$R_{batt} = R_{cell} \frac{N_s}{N_p}$$

$$I_{batt} = I_{cell} N_p$$

$$C_{batt} = N_p C_{cell}$$

$$SoC = SoC(0) + \sum_{i=1}^{t_{L_x}} \frac{I_{batt}}{C_{batt}} \Delta i$$

$$\Delta i = \frac{-v(j-1) + \sqrt{v^2(j-1) + 2a\Delta j}}{a}$$

$$V_{batt} = N_s(V_{OCV}^{cell} - R_{cell} I_{cell})$$

$$P_{batt} = I_{batt} V_{batt}$$

$$k_1 = \frac{m_{LIM}}{P_{LIM}}; k_2 = \frac{m_{VSI}}{P_{VSI}}$$

$$m = m_0 + N_s N_p m_{cell} + \frac{1}{\eta_{tr}} P_{maxCell} N_s N_p k_1 + \frac{1}{\eta_{tr} \cos(\phi)} P_{maxCell} N_s N_p k_2$$

$$C_d = f(v)$$

$$\rho = \frac{p_{tube}}{p_0} \cdot \rho_0$$

$$F_{dr}(j) = \frac{1}{2} S C_d(v) \rho v(j)^2$$

$$F_{tr}(j) = m a(j) + F_{dr}(j)$$

$$P_{tr}(j) = (m a(j) + F_{dr}(j)) \cdot v(j)$$

$$P_{tr} \leq \eta_{LIM} P_{batt}$$

$$E_c = \sum_0^{t_L} P_{batt} \Delta i$$

$$E_{caps} = r_{caps} \cdot E_c$$

$$d_{out} = 2 \cdot \lambda + d_{in}$$

$$\omega^{airleaks} = - \frac{3600 \cdot \pi \cdot k_{perm} \cdot L \cdot (p_{tube}^2 - p_0^2)}{\mu \cdot \ln(1 + \frac{\lambda}{d_{in}}) \cdot p_{tube}}$$

$$\tau_d = \frac{\pi \cdot (\frac{d_{in}}{2})^2 \cdot L}{q' \cdot \omega^{pump}} \cdot \ln(\frac{p_0}{p_{tube}})$$

$$\tau_d \leq 24h - T_{op}$$

$$E_{depr} = q' \cdot P_{pump} \cdot \tau_d$$

$$\omega^{airleaks} \leq q'' \cdot \omega^{pump}$$

$$E_{pr} = q'' \cdot P_{pump} \cdot t_{leaks}$$

(3.12)

It is worth observing that the single elements of the objective function have conflicting behaviours as  $E_{caps}$  decreases with the decrease of  $p_{tube}$ , whereas  $E_{depr}$  and  $E_{pr}$  increase. Therefore, the problem (3.12) determines the best the trade-off between the energy required by the depressurization process and the losses due to the drag force of the energy-autonomous capsules. As in the last Chapter, in (3.12) we consider the constraints associated with the model of the capsule's PS, in addition to the constraints of the infrastructure model and its operation.

The kinematic variables of the capsule are constrained as follows: The maximum speed is limited by  $v_{max}$  namely by the establishment of the choke-flow regime in the air surrounding the travelling capsules and the tube, the acceleration is limited to the value presented in the last Chapter derived from civil air crafts, and the traveling time at the end of the constant speed zone,  $i = t_{L_x}$  ( $j = \frac{L_x}{\Delta_j}$ ), is limited to  $T_{max_x}$ .

Regarding the constraints of the capsule's PS, the discharge rate of the cells that compose the BESS have to be lower than the maximum admissible discharge rate of the selected cell's type.  $V_{OCV}^{batt}$  is bounded with respect to the railway electrification system standard through the control variable  $N_S$  multiplied by the maximum  $V_{OCV}^{cell}$ . As this latter parameter is known once the cell technology is selected, we simply require that  $N_{S_{min}} \leq N_S \leq N_{S_{max}}$ . Finally, the BESS SoC should be in the range between  $SoC_{min}$  and  $SoC_{max}$ . The minimum value of the SoC can be found at position  $j = \frac{L_x}{\Delta_j}$ , which represents the end of the constant speed zone. After this point, the capsules enter the deceleration zone where a part of the braking is ensured by a regenerative one [37] - [38], but limited by the maximum charging rate of the considered cell,  $I_{cellMax_{charge}}$ . The regenerative braking zone is not taken into account in (3.12), as it is a consequence of acceleration and constant speed zones. The SoC at the end of the trajectory,  $SoC_{final}$  when  $j = \frac{L}{\Delta_j}$ , it is in any case computed.

For the infrastructure, the volume flow of the  $q''$  pumps should compensate at least the  $\omega^{airleaks}$ , and the time to depressurize the tube from  $p_0$  to  $p_{tube}$ ,  $\tau_d$ , is constrained to be less than  $24h - T_{op}$ .

As discussed in Chapter 2, the optimisation problem is non-convex and it has been solved using a gradient-based method [39] - [40]. The presence of mixed integer decision variables  $N_S, N_p, q'$  and  $q''$  was solved by treating these as continuous variables that, once determined, are rounded to the nearest integer. The problem (3.12) can be solved by different numerical solvers. We opted to use Yalmip [41] coupled with the fmincon solver in Matlab R2021. The initialization of the solver is performed by fixing the initial values of the decision variables (see below Section). Then, for all solutions of (3.12) obtained in correspondence of each of the initialisation of the decision variables, we retain only the one with the least objective value.

### 3.4 Numerical Assumptions

In this section, we provide the numerical assumptions used to solve the problem (3.12).



### 3.4.1 Infrastructure Assumptions

The diameter of the tube is selected based on the values the values reported in [10], [65]. Therefore, we assume for the simulations  $d_{in} = 4m$ .

For the thickness of the tube, the lower bound is given by reinforced concrete adopted by the tunnelling industry:  $\lambda = 25cm$  (e.g., as used for the Lötschberg tunnel in Switzerland and mentioned in [66]). The average value for the permeability of the reinforced concrete is  $k_{perm} = 5 \cdot 10^{-18} m^2$  as reported in [67]- [69].

Regarding the other physical quantities associated with the infrastructure,  $p_0 = 1bar$  is the standard atmospheric pressure and, for the dynamic air viscosity, we assumed  $\mu = 1.85 \cdot 10^{-5} Pa \cdot s$  (at 298.15 K). The rated power of the vacuum pumps and the associated characteristics are taken from real data: We refer to the Dessin Cobra NC 2500 B for which  $P_{pump} = 55kW$  and the characteristic  $\omega^{pump} = f(p_{tube})$  are both documented in [70].

Finally,  $L$  represents the length of the tube (or trajectory) for which we have considered the following three values:  $L = 226km$ ,  $L = 500km$  and  $L = 1000km$  as they are associated to typical distances of intra-continental flights.

### 3.4.2 Capsule Assumptions

Most of the numerical assumptions for capsules are those made in Chapter 2.

#### Assumptions on the Capsule Trajectory

As we mentioned in the previous chapter, we consider  $L = 226km$  for the first selected length of the hyperloop trajectory as it represents the distance between the two largest economical poles in Switzerland: Geneva and Zürich. In order to extensively validate the optimization process, we also consider  $L = 500km$  and  $L = 1000km$ . The discrete space sampling of the trajectory is  $\Delta j = 100m$ , resulting into 2260 points for  $L = 226km$ , 5000 points for  $L = 500km$  and 10000 points for  $L = 1000km$ . The value of  $\Delta j$  can be determined as the capsule acceleration is upper-bounded to 0.3204g (being this value derived from civil air crafts as in Chapter 2) and because we would like to have an upper bound on the variations in the capsule speed we would like to observe in correspondence of the point in the trajectory with the maximum acceleration. Since we would like to observe a maximum difference of speed of 50 km/h between two equidistant discretization points along the trajectory, for a maximum acceleration of 0.3204g, the corresponding  $\Delta j = 100m$ . Such a computation has been done in correspondence of the first and the second node of the discretized trajectory where we have the capsule's maximum acceleration.

In (2.17)-(2.19)  $M_1$  and  $M_2$  represent the acceleration zones,  $M_3$  the constant speed zone, and  $M_4$  the deceleration one. The chosen values for the extension of these zones is to have

them large enough to allow the optimization finding the optimal values of the capsule's speed. To be specific, for the maximum acceleration of  $0.3204g$  and the extensions of the acceleration zones  $M_1$  and  $M_2$  of total  $12\text{km}$ , the maximum potential speed is of  $988\text{ km/h}$  which is larger than the upper bound we have chosen for the maximum speed to avoid choked-flow conditions (see Section below). Regarding the deceleration zone, its extension is of  $20\text{ km}$ , i.e. a value larger than the extension of the acceleration zones allowing for the optimisation problem to have ample margin to determine the optimal speed profile while satisfying the constraints on the maximum speed and acceleration. It is worth noting that the extension of the acceleration/constant speed/deceleration zones can be also imposed by the modeler according to safety requirements of the hyperloop infrastructure.

### Assumptions on the Capsule and PS

In contrast with Chapter 2 where the capsule carried a payload of 25 persons, each of the capsules launched per day ( $r_{caps}$ ) carry a payload mass equivalent to 50 persons [71] (the corresponding mass can be also a cargo). The average mass payload attributed for a single person is  $80\text{kg}$ , which means a total payload mass of  $4000\text{kg}$ ; the considered mass of mechanics is  $6000\text{kg}$ . These two assumptions translate into  $m_0 = 10000\text{kg}$ .

According to [42], the frontal cross-section surface of capsules is assumed to be  $S = 3.14\text{m}^2$ . Regarding the dependency of the drag coefficient with the speed of the capsule,  $C_d(v)$ , we adopted the values shown in Fig.3 ("3D\_model") of [63] for a blockage ratio  $S_{ratio} = 0.25$  (as it is in our case). For the reader's convenience, such dependency  $C_d(v)$  is also shown in Fig. 3.5. Considering the lack of available literature regarding hyperloop capsules dependency of aerodynamic drag coefficient with speed, a dedicated sensitivity analysis on the obtained optimal solutions is reported in Section V.

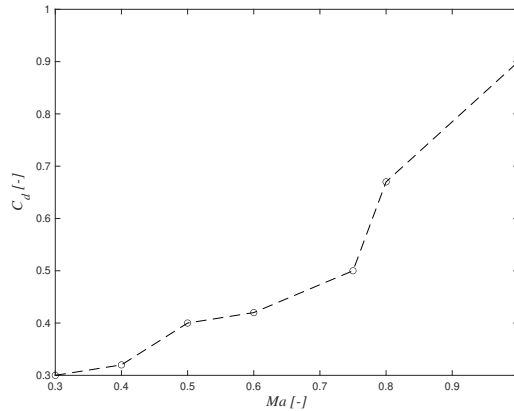


Figure 3.5:  $C_d$  dependency with the Mach number,  $Ma$ , adapted from [63].

Regarding the PS, the efficiency of the power transfer is assumed to be  $\eta_{tr} = 0.95$ , whereas the efficiency of a high-speed LIM is assumed to be  $\eta_{LIM} = 0.65$  (this value has been inferred by

preliminary tests at the Authors' laboratory). The parameter  $k_1$  for LIM is selected according to a hyperloop capsule prototype realised by our laboratory and assumed to be  $k_1 = 0.091 \frac{kg}{kW}$ . The values for  $k_2$  is chosen with respect to industry-grade VSI used by the automotive sector:  $k_2 = 0.075 \frac{kg}{kW}$ , as well as  $\cos(\phi) = 0.6$ . Furthermore, in Section 3.5 it is shown how the dependency of both  $\eta_{LIM}$  and  $\cos(\phi)$  with the capsule's speed influences the solution of (3.12).

In (3.13), we indicate the upper bounds for the accelerations<sup>II</sup> in the Sections  $M_1$ ,  $M_2$  and  $M_3$  (the values of these upper bounds are the same used in Chapter 2). In (3.13), we also indicate the maximum speed,  $v_{max}$ , and maximum travel time at the end of the constant speed zone,  $T_{max_1}$ ,  $T_{max_2}$  and  $T_{max_3}$  for the three selected trajectory lengths  $L = 226km$ ,  $L = 500km$  and  $L = 1000km$ . The maximum travel times at the end of constant speed zone are bounded.

$$\left\{ \begin{array}{l} T_{max_1} = 25min; T_{max_2} = 60min; T_{max_3} = 120min \\ a_{min_{M_1}} = 0g; a_{max_{M_1}} = 0.3204g \\ a_{min_{M_2}} = 0g; a_{max_{M_2}} = 0.3204g \\ a_{min_{M_3}} = 0g; a_{max_{M_3}} = 0.0001g \end{array} \right. \quad (3.13)$$

Regarding the BESS, the numerical assumptions shown in (3.14) can be found in Section 2.3.2.

$$\left\{ \begin{array}{l} SoC_{max} = 100\% \\ SoC_{min} = 10\% \\ N_{s_{min}} = 238 \\ N_{s_{max}} = 357 \\ R_{cell} = 4.4m\Omega \\ I_{cellMax} = 150A \\ I_{cellMax_{charge}} = 5A \\ V_{cell}^{OCV} = 4.2V \end{array} \right. \quad (3.14)$$

### 3.4.3 Assumptions for the computation of the Kantrowitz Limit and associated capsules' maximum speed

By considering  $T = 288.15K (t = 15^\circ C)$  and  $\gamma = 1.4032$ , Fig. 3.6 illustrates the dependency of  $M_\infty$  with  $S_{ratio} = \frac{S}{S_{tube}}$ . At  $T = 288.15K (t = 15^\circ C)$ , the speed of the sound is  $v_{sound} = 1224 \frac{km}{h}$  and, since  $S_{ratio} = 0.25$ , we get at the choke flow limit  $M_\infty = 0.504$  and a corresponding  $v_{max} = 616.28 \frac{km}{h}$ . Fig. 3.6 has been obtained by numerically inputting the above-mentioned values into (3.11).

---

<sup>II</sup>Note that  $g = 9.81 \frac{m}{s^2}$

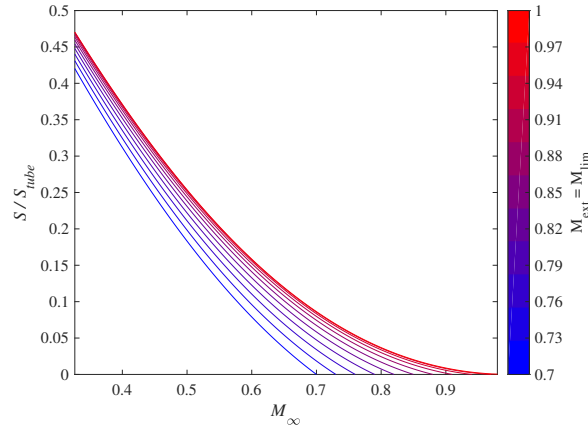


Figure 3.6: Assessment of the choked flow regime of the fluid around the hyperloop capsule.

### 3.4.4 Hyperloop Infrastructure Operational Assumptions

For the infrastructure operation, the most relevant parameter to fix is  $T_{op}$ , as it represents the total number of hours-per-day where capsules are launched into the hyperloop infrastructure. In order to define a value for this parameter, we made reference to the actual daily time for operations adopted by the Swiss Federal railways for which  $T_{op} = 16 \text{ hours}$ . The other parameter to fix is the number of capsules launched per day ( $r_{caps}$ ). In [71], it is reported a rate of  $\frac{1 \text{ capsule}}{2 \text{ minutes}}$  which translates to a  $r_{caps} = 480 \frac{\text{capsules}}{\text{day}}$ , equivalent to a maximum number of passengers per day of  $k_{pass} = 24000 \frac{\text{passengers}}{\text{day}}$ . Furthermore, the value adopted for  $r_{caps}$  can be coupled with the capsules distance at cruising speed vs the distance needed to decelerate them in case of an emergency braking. Indeed, it is reasonable to suppose the network of capsules being controlled by an automatic system capable to estimate the position of each capsule along their trajectories (i.e., a classical state estimator). Such an automatic system governs the entire network of capsules and is capable to handle any error appearing from any capsule. In this case, all the capsules enter in an “Error State” where a safe braking is applied to all capsules to stop them. Assuming the capsules traveling at a maximum speed of  $616 \frac{\text{km}}{\text{h}}$  ( $171 \frac{\text{m}}{\text{s}}$ ), namely the maximum cruising speed we have determined in Section IV.C, a safety braking deceleration should not exceed  $0.5g$  (i.e.,  $4.905 \frac{\text{m}}{\text{s}^2}$ ) (such a value for an emergency deceleration has been proposed to prevent passengers’ injuries in the document by C. Grover, I. Knight in [73]). Therefore, the corresponding safety braking distance would be:  $L_a = 2457.8 \text{ m}$ . For the assumed  $r_{caps} = \frac{1 \text{ capsule}}{2 \text{ minutes}}$ , the time difference between two capsules is of  $120 \text{ s}$  and, at the maximum speed of  $171 \frac{\text{m}}{\text{s}}$ , the distance between two subsequent capsules is  $L_b = 20520 \text{ m}$ . It is evident that  $L_a \ll L_b$  guaranteeing a safe emergency braking with ample margin. Regardless of the above reasoning, a sensitivity analysis on the influence of  $r_{caps}$  on the solutions provided by the optimization problem is contained in Section 3.5.

### 3.5 Results

This section illustrates the results obtained by solving (3.12) with respect to different values of the main parameters of the proposed optimisation problem. The results are shown with respect to the quantities shown in Table 3.1 as they represent the main operational characteristics of both the hyperloop infrastructure and capsule's propulsion system.

Variable	Name	Unit
$p_{tube}$	tube's pressure	mbars
$E_{depr}$	depressurization's energy	Wh
$E_{pr}$	process' energy	Wh
$E_{caps}$	capsules' energy	Wh
$max(P_{batt})$	capsules' maximum power	MW
$max(v)$	capsules' maximum speed	km/h
$m$	capsules' masses	kg
$v$	capsules' speed	km/h
$t_{L_k}$	capsules' traveling time profile	minutes
$SoC$	capsules' state-of-charge profile	%
$P_{batt}$	capsules' power profile	MW
$E_r$	capsules' average energy consumption	Wh/passenger/km
$T_{depr}$	tube's depressurization period	days

Table 3.1: Variables' information.

#### 3.5.1 Main Numerical Assumptions

As the total energy consumption of the hyperloop system is largely influenced by  $T_{depr}$ , the analyses discussed in this section are carried out by increasing this parameter up to a certain value until the total energy consumption of the infrastructure tends to an asymptotic value. Hence,  $T_{depr}$  is varied in the following set:  $T_{depr} = \{1, 7, 14, 21, 28, 35, 42, 70, 84, 168\}$  days for each of the three considered trajectory lengths. As the optimisation problem is non-convex, yet numerically tractable, it is solved by using a gradient-descent method where the initial conditions were varied within intervals that have a technical feasible meaning. Then, the obtained solutions were ranked according to their objective value in order to determine the one with the least value. For every  $T_{depr}$  and  $L$ , the initialization of the control variables were made accordingly to the intervals shown in Table 3.2. The  $N_s$ ,  $N_p$  and  $a$  initialization values were chosen accordingly to Chapter 2, and for the initialization for  $p_{tube}$ , we assumed the range indicated in Chapter 2 and [10].

#### 3.5.2 General Observations

Fig. 3.7 shows the optimal values of  $p_{tube}$  as a function of  $T_{depr}$  for each trajectory length. The optimal pressure inside the tube,  $p_{tube}$  varies from 2.82mbar to 76.92mbar for  $L = 226km$ ,

Variable	Min value init	Max value init	Discretization step values	Unit
$N_s$	200	400	20	no. cells
$N_p$	20	40	5	no. cells
$a$	0	0.36g	0.18g	$\frac{m}{s^2}$
$p_{tube}$	0	300	20	mbar
$q'$	100	600	50	no. pumps
$q''$	0	100	20	no. pumps

Table 3.2: Initialization of the control variables.

from  $1.17\text{mbar}$  to  $54.5\text{mbar}$  for  $L = 500\text{km}$  and from  $1.14\text{mbar}$  to  $17.25\text{mbar}$  for  $L = 1000\text{km}$ . As a first general conclusion we can see that for lower values of  $T_{depr}$ , the largest fraction of used energy is associated to the hyperloop infrastructure, namely  $E_{pr} + E_{depr}$ . For values of  $T_{depr}$  in the range between  $42\text{days}$  to  $168\text{days}$ , the energy needed by the infrastructure is of the same order of magnitude of the energy used by the capsules, whereas, for higher values of  $T_{depr}$  (and of  $p_{tube}$ ), the energy used by the capsules is dominant (this dependency is expected as  $\omega^{airleaks}$  are lower for higher values of  $p_{tube}$ ). It is also worth observing that, for the same value of  $T_{depr}$ , the optimisation problem determines optimal tube's pressures that decrease with the increase of the trajectory length as, for longer trajectories, capsules' aerodynamic energy losses become more important compared to the energy used by the hyperloop infrastructure (i.e.,  $E_{pr} + E_{depr}$ ) that tends to a constant value for  $T_{depr} \rightarrow \infty$  (see Fig. 3.8, Fig. 3.9). Furthermore, as the value of  $T_{depr}$  increases, the value of  $p_{tube}$  increases as well. This trend is due to the non-linear behaviour of  $E_{pr}$  and  $E_{depr}$  as a function of the tube's operating pressure. In particular, for increasing values of  $p_{tube}$ ,  $E_{pr}$  and  $E_{depr}$  both decrease and tend to have comparable magnitudes. Indeed, in (3.12) the best trade-off between the energy used for by the capsules,  $E_{caps}$ , and the energy used by the hyperloop infrastructure,  $E_{caps} + E_{pr}$ , determines the value of  $p_{tube}$  that tends to a constant value for  $T_{depr} \rightarrow \infty$ . These trends are shown in Fig. 3.8, Fig. 3.9 and Fig. 3.10 that quantify, respectively, the dependency of  $E_{depr}$  with  $T_{depr}$ , the dependency  $E_{pr}$  with  $T_{depr}$  and the dependency  $E_{caps}$  with  $T_{depr}$ .

Fig. 3.11 shows the optimal maximum power required by the PS of a hyperloop capsule as a function of  $T_{depr}$ : it can be seen that it increases with the increase of  $T_{depr}$  since larger values of  $T_{depr}$  results in larger tube operational pressures,  $p_{tube}$ , and consequent larger aerodynamic drag. It is also worth observing that, for the various considered trajectories and  $T_{depr}$ , the optimal maximum power required by the PS of a hyperloop capsule is in the range between  $1.8 - 5.1\text{MW}$ . These values of maximum power appear to be compatible with technologies nowadays available for both BESS and power electronics.

Fig. 3.12 shows the optimal maximum cruising speeds of the capsules for the various considered trajectories and  $T_{depr}$ . The results shown in this figure allows to draw an important conclusion: in order to optimise the energy needs of the whole hyperloop system, the maximum speed of hyperloop capsules has to be subsonic. Such a conclusion appears to hold also for relatively long trajectories.

It is worth observing that, due to the non-linearity between the  $T_{max_1}$ ,  $T_{max_2}$  and  $T_{max_3}$  and longer constant speed zone (i.e.,  $L = 1000km$ ), the capsules energy consumption, the capsule's BESS maximum power and the capsule's maximum speed values for  $L = 500km$  are larger (i.e., in Fig. 3.10, Fig. 3.11, Fig. 3.12.)

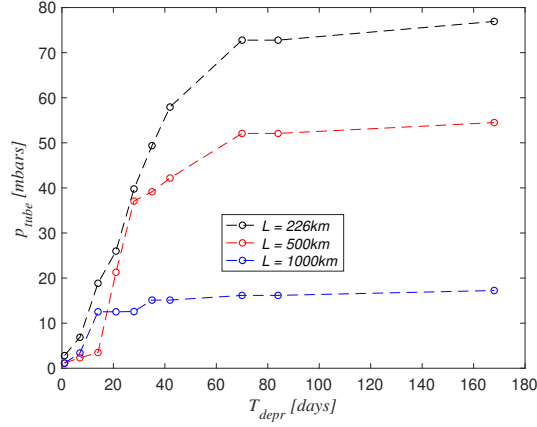


Figure 3.7: Dependency of the optimal operational internal pressure of the tube,  $p_{tube}$ , with  $T_{depr}$ .

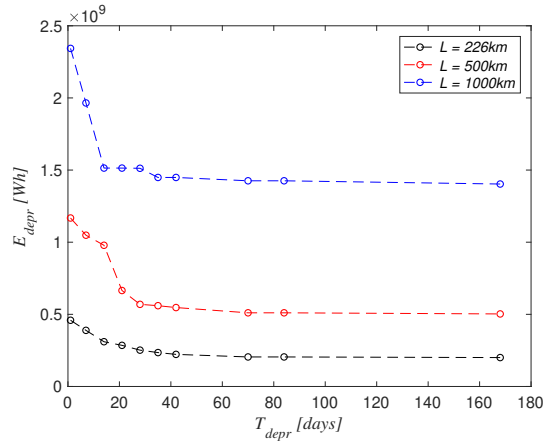


Figure 3.8: Dependency of the tube depressurization energy,  $E_{depr}$ , with  $T_{depr}$ .

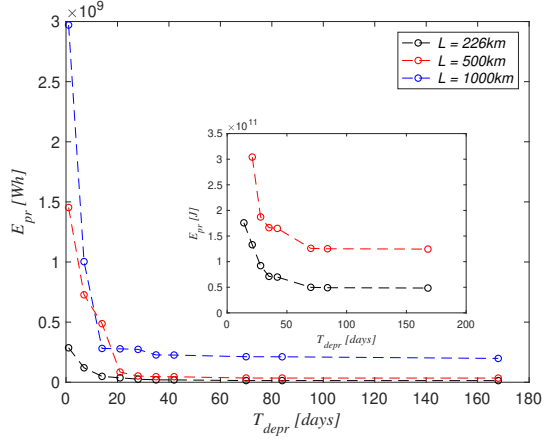


Figure 3.9: Dependency of the air leaks compensation energy,  $E_{pr}$ , with  $T_{depr}$ .

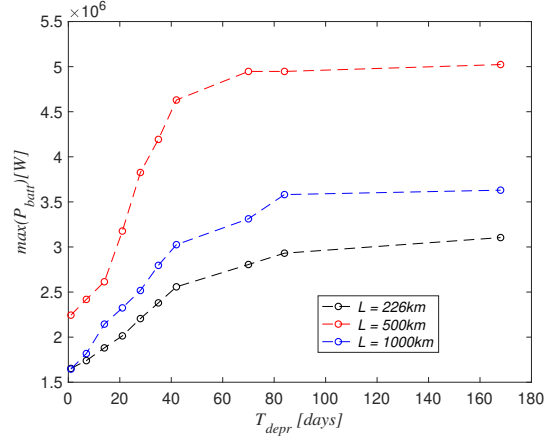


Figure 3.11: Dependency of the capsule's BESS maximum power,  $\max(P_{BESS})$ , with  $T_{depr}$ .

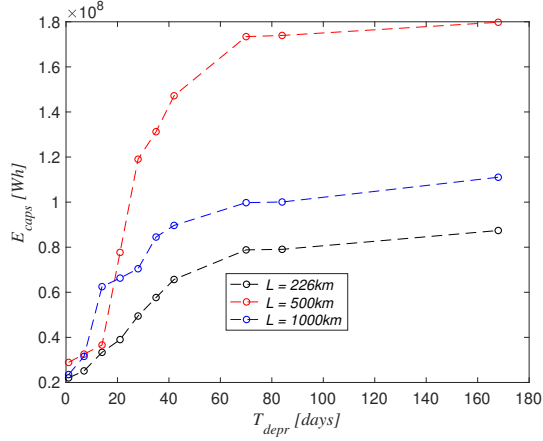


Figure 3.10: Dependency of capsules network energy,  $E_{caps}$ , with  $T_{depr}$ .

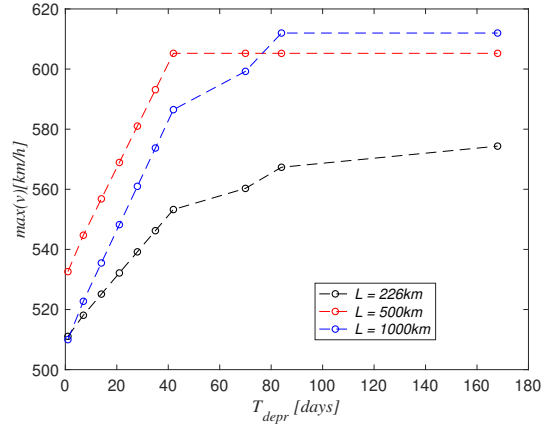


Figure 3.12: Dependency of capsule's maximum (or cruising) speed,  $\max(v)$ , with  $T_{depr}$ .



### 3.5.3 Pressure vs. Masses

Fig. 3.13 illustrates the dependency of the active masses of the capsule:  $m$ ,  $m_{BESS}$  and  $m_{PS}$  as a function of the infrastructure's operational pressure,  $p_{tube}$ . Observe a linear increase of the masses as a function of  $p_{tube}$  with steeper trends for longer trajectories.

It is important to remember that the proposed optimisation problem considers both the capsule's mass increase with  $p_{tube}$  (as the capsules are energy-autonomous) along with the increase of the infrastructure's energy with the decrease of  $p_{tube}$ . As a matter of fact, the identified optimal solutions for the capsule's masses and  $p_{tube}$  represent the best trade-off that makes the solution of the proposed problem non-trivial and less intuitive.

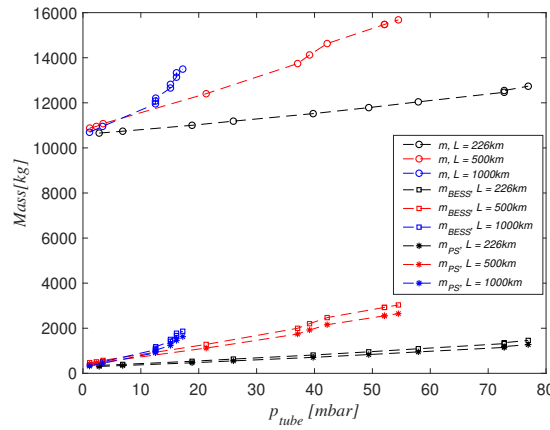


Figure 3.13: The dependency of the masses ( $m$ ,  $m_{BESS}$ ,  $m_{PS}$ ) with  $p_{tube}$  for every  $L$ .

### 3.5.4 Profiles of Speed, Travel Time, BESS SoC and Power

In this subsection, we show the profiles of the most important internal variables of the optimisation problem (3.12) as a function of the capsule's position along its trajectory for the specific case of  $L = 226\text{km}$  (as for the other graphs, the results are also shown for the various  $T_{depr}$ ). Fig. 3.14, Fig. 3.15, Fig. 3.16, Fig. 3.17 show the profile of speed, travel time, BESS SoC and BESS power as a function of the capsule position for every  $T_{depr}$ .

As already observed, due to the nonlinear increase of the aerodynamic losses with the speed associated with  $C_d$  and  $F_{dr}$ , the optimal cruising speed of the capsules is in the order of  $612 \frac{\text{km}}{\text{h}}$ . Such an optimal cruising speed is linked with  $T_{depr}$ , due to the various optimal values of  $p_{tube}$ .

Fig. 3.16 shows the trend of the capsule's BESS SoC. For very short maintenance periods, i.e.,  $T_{depr} = 1\text{day}$  and partially  $T_{depr} = 7\text{days}$ , the SoC does not reach the minimum binding value of 10%, because the BESS is constrained by the maximum discharge rate of the cell. Indeed, the optimal solutions identified for these short maintenance periods have a peculiar BESS design for which the binding constraints in (3.12) are those associated with the power,

rather than with the energy of the BESS. This occurs because the optimal  $p_{tube}$  reaches its lowest values and the energy consumption for one capsule,  $E_c$ , is the lowest too. Therefore, for low values of  $T_{depr}$  (and corresponding  $p_{tube}$ ), the hyperloop system can be associated with a power-intensive application, as the constraints associated with the cells discharge are binding. Whereas, for higher values of  $T_{depr}$  (and corresponding  $p_{tube}$ ), the hyperloop system can be associated to an energy-intensive application as the constraints on the BESS SoC are binding.

Fig. 3.17 shows the different optimal profiles of  $P_{batt}$ , depending on  $T_{depr}$ . The maximum power vary in the interval between 1.8–3.2MW. Smaller maximum values of  $P_{batt}$  correspond to lower  $p_{tube}$  and lower maximum speed (see Fig. 3.14).

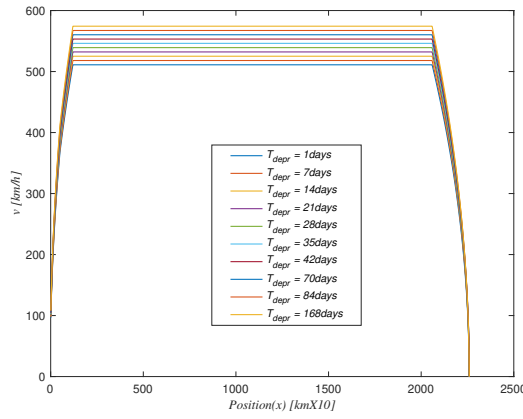


Figure 3.14: Capsule speed along its position for each  $T_{depr}$  (profiles refers to  $L = 226\text{km}$ ).

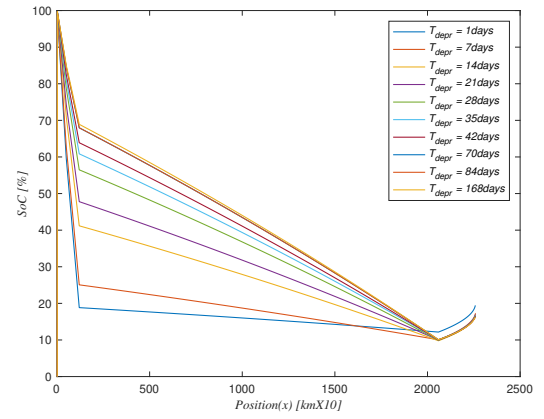


Figure 3.16: Capsule BESS SoC along its position for each  $T_{depr}$  (profiles refers to  $L = 226\text{km}$ ).

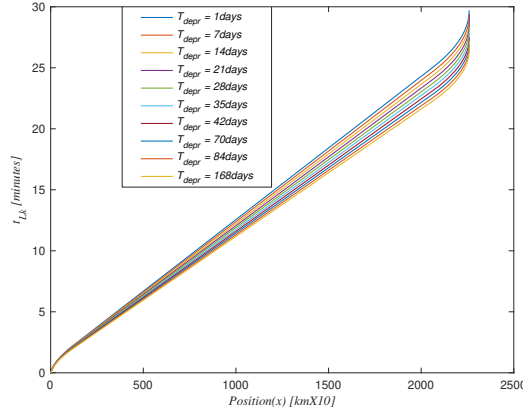


Figure 3.15: Capsule traveling time,  $t_{Lk}$ , along its position for each  $T_{depr}$  (profiles refers to  $L = 226\text{km}$ ).

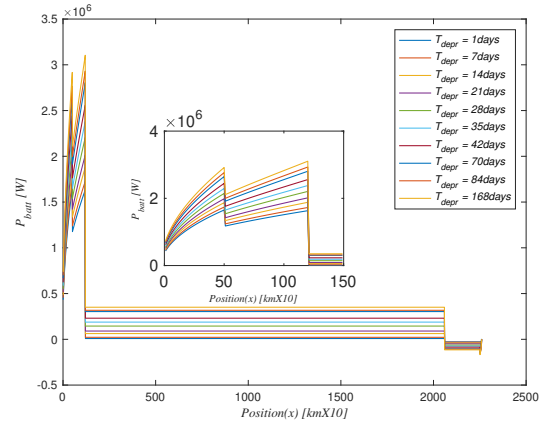


Figure 3.17: Capsule  $P_{batt}$  along its position for each  $T_{depr}$  (profiles refers to  $L = 226\text{km}$ ).

### 3.5.5 Energy Needs and Infrastructure Operation

For a given  $T_{depr}$  and trajectory length, the total energy need per number of passengers and per km is given in (3.15) and the results are shown in Fig. 3.18.

$$E_r \left[ \frac{Wh}{passenger \cdot km} \right] = \frac{E_{depr} + T_{depr} \cdot (E_{pr} + E_{caps})}{L \cdot T_{depr} \cdot k_{pass}} \quad (3.15)$$

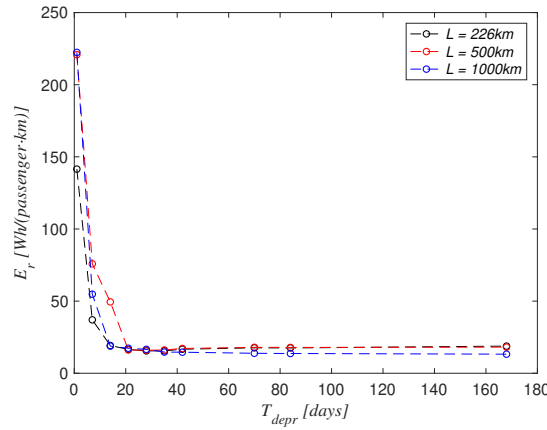


Figure 3.18: Total energy need per number of passengers and per km,  $E_r$ , as a function of  $T_{depr}$  for each trajectory length.

The operational strategy of the hyperloop infrastructure plays an important role on the energy consumption of the entire system. For short  $T_{depr}$ ,  $E_r$  can reach high values, especially for long trajectory lengths, as for  $L = 1000km$  the best values of  $E_r$  are in the range of  $100 - 225 \frac{Wh}{passenger \cdot km}$ . Therefore, independently of the infrastructure length, it is suggested to have  $T_{depr} \geq 21days$  as, depending on the length of the trajectory,  $E_r$  ranges between  $[20, 30] \frac{Wh}{passenger \cdot km}$ .

### 3.5.6 Impact of the Levitation Drag

The optimisation model (3.12) considers suspended capsules where the levitation drag is null. However, it is worth analysing the impact of the magnetic levitation drag force,  $F_{drlev}$  on the optimal solution of (3.12) since the BESS power profile might be influenced as well as the energy consumption of the capsule.

In this sub-section, we analyse such an impact for a trajectory length of  $L = 226km$ .

$F_{drlev}$  is given by (3.16) where  $C_{lev}$  represents the levitation drag coefficient that has a dependency with the speed of the capsule,  $v$ , as discussed in [74]. The representation of  $C_{lev}(v)$  is shown in Fig. 3.19 adapted from [74].

$$F_{drlev}(j) = mgC_{lev}(v(j)) \quad (3.16)$$

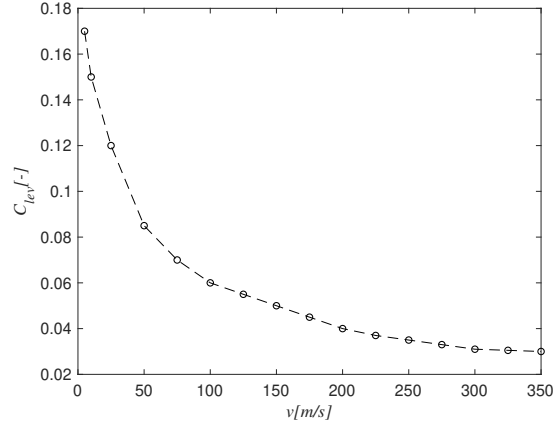


Figure 3.19:  $C_{lev}$  dependency with the speed of the capsule,  $v$ , adapted from [74].

Therefore, compared with (3.7), the new capsule's traction force is represented by (3.17) and the traction power by (3.18).

$$F_{tr}(j) = ma(j) + F_{dr}(j) + F_{drlev}(j) \quad (3.17)$$

$$P_{tr}(j) = (ma(j) + F_{dr}(j) + F_{drlev}(j)) \cdot v(j) \quad (3.18)$$

With the same conditions imposed in (3.12), except for the definition of  $F_{tr}$  and  $P_{tr}$  that, in this case, include the magnetic levitation drag, the problem (3.12) has been solved for all the  $T_{depr}$  for the trajectory length  $L = 226\text{km}$ .

The profiles of  $p_{tube}$ ,  $P_{BESS}$  and  $v$  are presented in Fig. 3.20, Fig. 3.21, respectively in Fig. 3.22. In Fig. 3.23, it is worth observing the  $m$ ,  $m_{BESS}$ ,  $m_{PS}$  dependencies with  $p_{tube}$  for  $L = 226\text{km}$ .

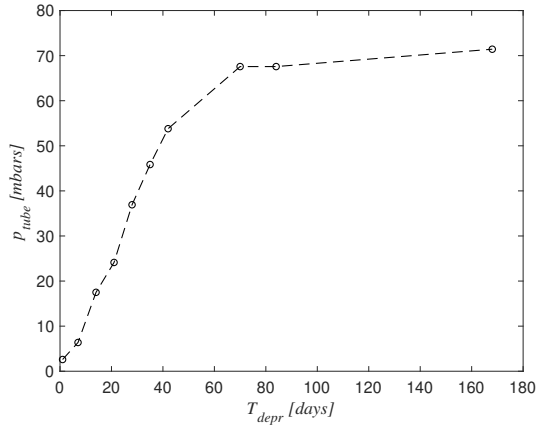


Figure 3.20: Infrastructure  $p_{tube}$  for each  $T_{depr}$  (profiles refers to  $L = 226km$ ) including the losses of the passive levitation.

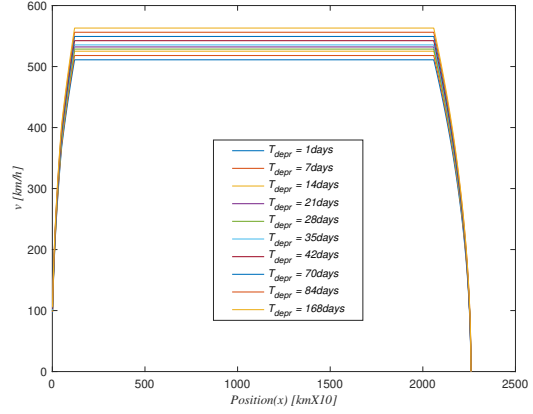


Figure 3.22: Speed  $v$  along its position for each  $T_{depr}$  (profiles refers to  $L = 226km$ ) including the losses of the passive levitation.

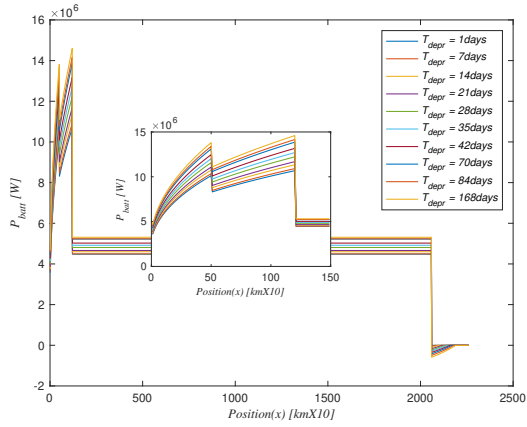


Figure 3.21: Capsule  $P_{batt}$  along its position for each  $T_{depr}$  (profiles refers to  $L = 226km$ ) including the losses of the passive levitation.

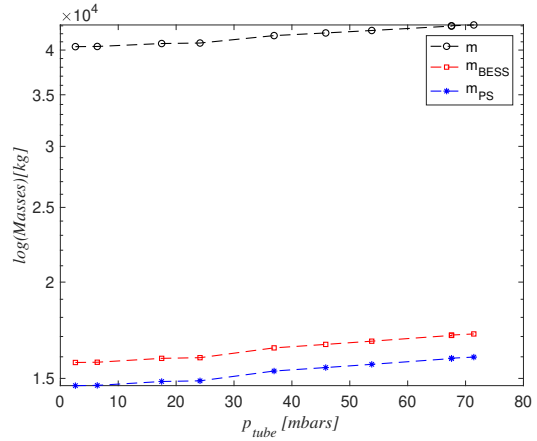


Figure 3.23: The dependency of masses ( $m$ ,  $m_{BESS}$ ,  $m_{PS}$ ) with  $p_{tube}$  for  $L = 226km$  including the losses of the passive levitation.

By comparing the results of Fig. 3.20 with those in Fig. 3.7, the tube operational pressure  $p_{tube}$  shows a slight decrease of up to 10% for each  $T_{depr}$ . Regarding the capsule masses, by comparing the results of Fig. 3.13 with those in Fig. 3.23, we can observe that, for each operational pressure,  $p_{tube}$ , the total mass increase of up to 4 times. The peak BESS power required for the case with magnetic levitation is about  $14.5MW$  whereas, for the case without the magnetic levitation, is  $3MW$ . For the constant speed zone, the BESS power required for the case with magnetic levitation is about  $5.5MW$  while, for the case without the magnetic levitation, is about  $0.5MW$ . Regarding the speed profiles, the comparison between Fig. 3.14 vs Fig. 3.22 shows that they are quite similar.

When compared to a Maglev system running in open-air (i.e., at  $p_0$ ) and considering the magnetic drag of the levitation, (i.e., Chuo Shinkansen in tunnel, Abe 2013, 7 sections as shown in [75]), the power needed at the constant speed zone is estimated to be  $P_{mag} = 26MW$  for a speed of  $v_{mag} = 500 \frac{km}{h}$  and a propulsion efficiency of  $\eta_{mag} = 0.65$ .

In view of the obtained results, it is worth observing that the magnetic levitation is responsible of a dramatic increase the capsule's masses, energy needs as well as peak power requirements. It is quite clear from these results that hyperloop capsules have to rely on drag-less magnetic levitation solutions especially if the energy reservoir is embedded in the capsule.

### 3.5.7 Sensitivity Analysis

This section contains a comprehensive sensitivity analysis with respect to parameters that have an influence on the solutions of the proposed optimisation problem. In particular, these parameters are: (i) the number of capsules per unite of time  $r_{caps}$ , (ii) the aerodynamic drag coefficient  $C_d$ , (iii) the permeability of tube's material  $k_{perm}$ , (iv) the passive mass of the capsule  $m_0$  and (v) the LIM efficiency and power factor dependency on capsule's speed  $\eta_{LIM}(v)$ ,  $\cos(\phi)(v)$ . The length of trajectory is considered  $L = 500km$ .

#### Variable $r_{caps}$ (number of capsules per unite of time)

In this sub-section we analyse the influence on the solution of (3.12) of different values of the variable  $r_{caps}$ . For this purpose, with respect to the original value of  $r_{caps} = \frac{1capsule}{2minutes}$  chosen for this parameter, we have considered two other values, namely: (i)  $r_{caps} = \frac{1capsule}{5minutes}$  and (ii)  $r_{caps} = \frac{1capsule}{10minutes}$ .

Fig. 3.24 shows that, with respect to the values obtained for  $r_{caps} = \frac{1capsule}{2minutes}$  in correspondence of large values of  $T_{depr}$ , a slight change in the tube pressure (less than 15%) is obtained. The differences for  $E_{depr}$ ,  $E_{pr}$  and  $E_{caps}$  are presented in Fig. 3.25, Fig. 3.26 and Fig. 3.27, respectively. Lower flows of capsules produce a decrease of the energy consumption of the capsules. As a consequence, in order to minimize the total energy need, the optimization identifies slightly larger tube pressure (see Fig. 3.24) that limit the increase of the energy

needed to operate the infrastructure (i.e.,  $E_{depr}+E_{pr}$ ). The values obtained for the energy per-passenger-per-km shown in Fig. 3.28, do not exceed  $70Wh/passenger/km$  for  $r_{caps} = \frac{1capsule}{10minutes}$  and  $T_{depr} > 21days$  and are slightly higher compared to the case of  $r_{caps} = \frac{1capsule}{2minutes}$ .



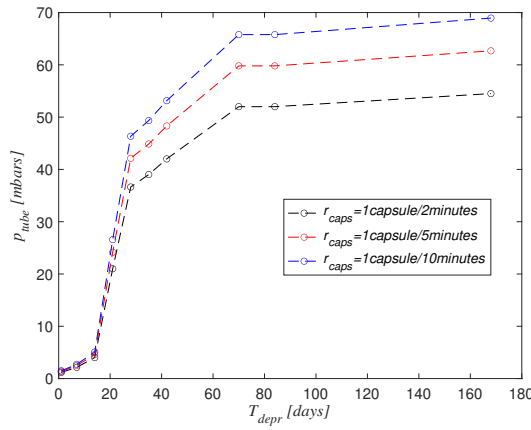


Figure 3.24: Dependency of the optimal operational internal pressure of the tube,  $p_{tube}$ , with  $T_{depr}$  ( $r_{caps}$  sensitivity analysis).

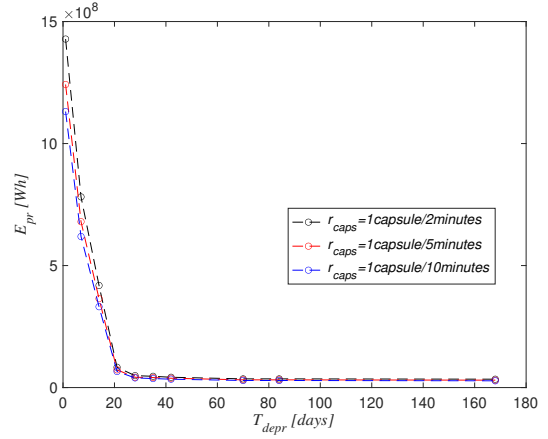


Figure 3.26: Dependency of the air leaks compensation energy,  $E_{pr}$ , with  $T_{depr}$  ( $r_{caps}$  sensitivity analysis).

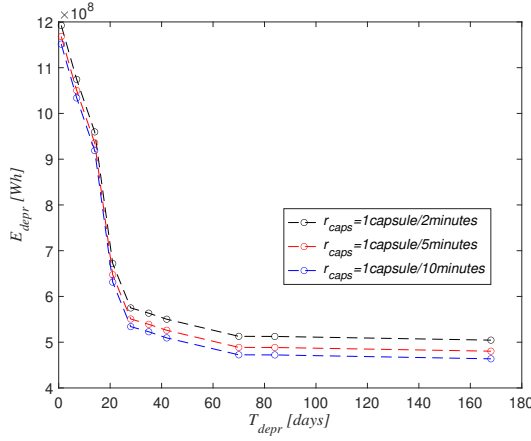


Figure 3.25: Dependency of the tube depressurization energy,  $E_{depr}$ , with  $T_{depr}$  ( $r_{caps}$  sensitivity analysis).

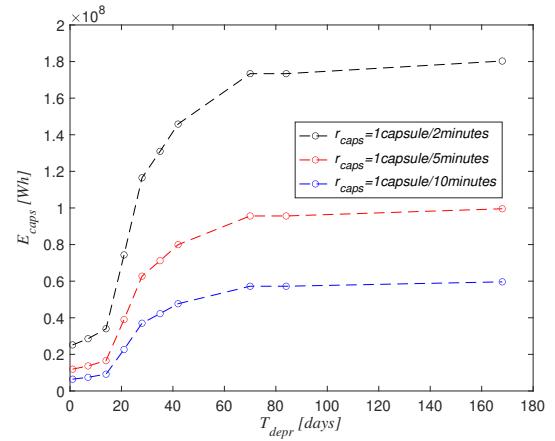


Figure 3.27: Dependency of capsules network energy,  $E_{caps}$ , with  $T_{depr}$  ( $r_{caps}$  sensitivity analysis).

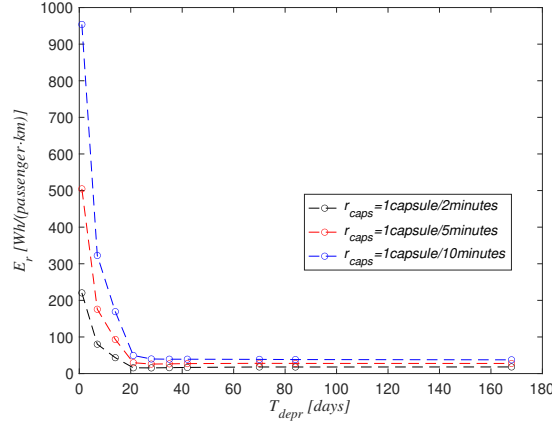


Figure 3.28: Total energy need per number of passengers and per km,  $E_r$ , as a function of  $T_{depr}$  for each trajectory length ( $r_{caps}$  sensitivity analysis).

#### Variable $C_d$ (aerodynamic drag coefficient)

A sensitivity analysis regarding this parameter is here carried out by adding an offset to the original aerodynamic drag coefficient as shown in Fig. 3.29 where (i)  $C_d = C_{d,orig} + 0.1$  and (ii)  $C_{d,orig} = C_d + 0.2$ .

A variation in the drag coefficient directly impacts the energy required by the capsules. In order to minimise such an impact, the optimisation identifies optimal tube pressures that, in correspondence of large values of  $T_{depr}$ , have a slight change (less than 15% - see Fig. 3.30) with respect to the optimal solutions obtained for the original aerodynamic drag coefficient. The obtained values for  $E_{caps}$  shown in Fig. 3.31 exhibit changes in the order of 10% with respect to the original value. It is also interesting to observe that the variations on the tube pressure are small enough to not influence the energy consumption related to the infrastructure (i.e.,  $E_{depr}$  in Fig. 3.32 and  $E_{pr}$  in Fig. 3.33). The energy per-passenger-per-km shown in Fig. 3.34 is very similar with respect to values obtained with the original aerodynamic drag coefficient.

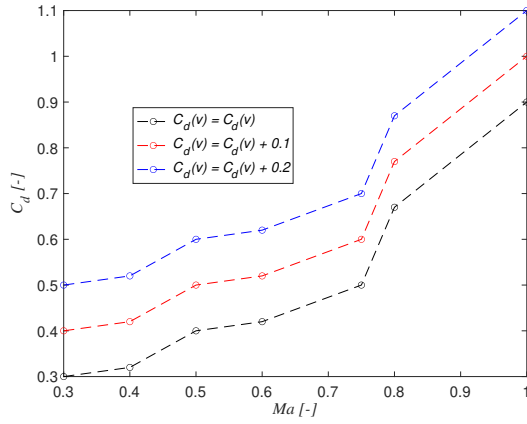


Figure 3.29:  $C_d$  dependency with the Mach number,  $Ma$  ( $C_d$  sensitivity analysis).

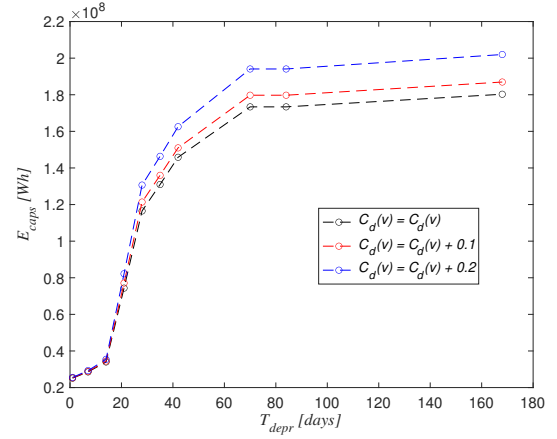


Figure 3.31: Dependency of capsules network energy,  $E_{caps}$ , with  $T_{depr}$  ( $C_d$  sensitivity analysis).

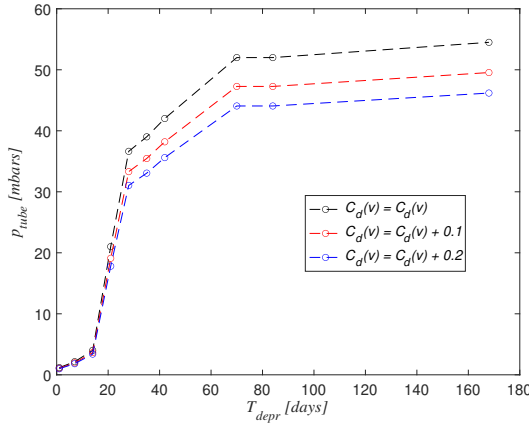


Figure 3.30: Dependency of the optimal operational internal pressure of the tube,  $p_{tube}$ , with  $T_{depr}$  ( $C_d$  sensitivity analysis).

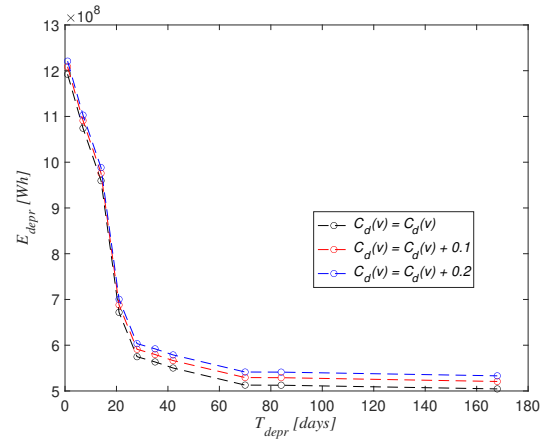


Figure 3.32: Dependency of the tube depressurization energy,  $E_{depr}$ , with  $T_{depr}$  ( $C_d$  sensitivity analysis).

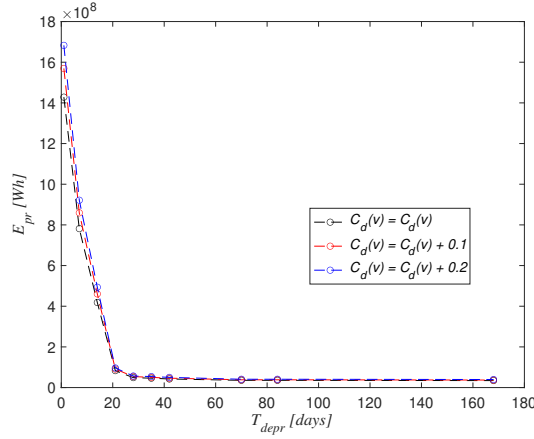


Figure 3.33: Dependency of the air leaks compensation energy,  $E_{pr}$ , with  $T_{depr}$  ( $C_d$  sensitivity analysis).

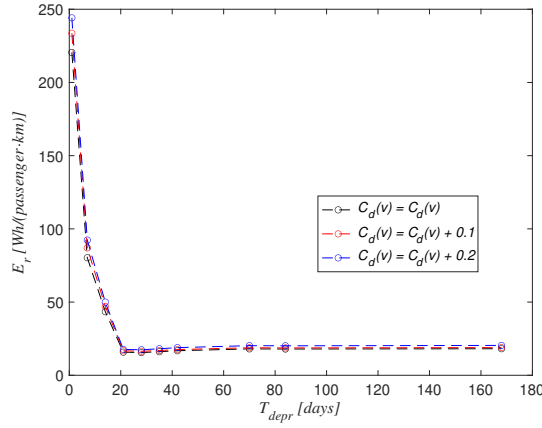


Figure 3.34: Total energy need per number of passengers and per km,  $E_r$ , as a function of  $T_{depr}$  for each trajectory length ( $C_d$  sensitivity analysis).

#### Variable $k_{perm}$ (permeability of tube's material)

It is worth observing that the construction of an hyperloop tube may require to impose the value of  $k_{perm}$  in order to guarantee a given performance of the tube regarding its depressurization and air leaks. Although the value adopted for  $k_{perm}$  is inferred from the existing literature, a sensitivity analysis on this parameter is shown in this sub-section. The sensitivity analysis is considering variations of 25% with respect to the original value assumed for this parameter, namely: (i)  $k_{perm} = 3.75 \cdot 10^{-18} m^2$  and (ii)  $k_{perm} = 6.25 \cdot 10^{-18} m^2$ .

As expected, higher values of the tube permeability involve higher amount of energy needed for the operation of the infrastructure (i.e.,  $E_{depr} + E_{pr}$ ). As a consequence, the proposed optimization manages to adjust the tube pressure,  $p_{tube}$  (see Fig. 3.35) such that, for a higher value of  $k_{perm}$ , the tube pressure is increased with respect to the values obtained for the

original value assumed for  $k_{perm}$  in order to minimize the increase of  $E_{depr}$  (see Fig. 3.36) and  $E_{pr}$  (see Fig. 3.37). On the contrary, for a lower value of  $k_{perm}$ , the optimization identifies lower tube pressure levels with respect to those obtained in correspondence of the original value adopted for  $k_{perm}$ . As a result,  $E_{depr}$  and  $E_{pr}$  present an average difference of 7% with respect to the values obtained with the original value adopted for  $k_{perm}$ . It is also worth observing that different tube's operating pressures have an impact on the capsules' energy consumption  $E_{caps}$  (see Fig. 3.38) that exhibits changes of 10%–11% with respect to the values obtained to the original value adopted for  $k_{perm}$ . In Fig. 3.39, the average energy consumption does not exhibit a significant change.

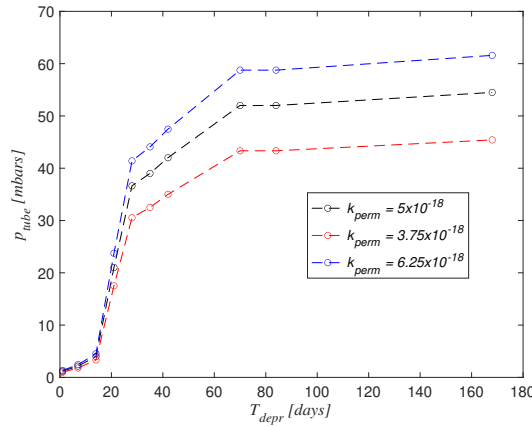


Figure 3.35: Dependency of the optimal operational internal pressure of the tube,  $p_{tube}$ , with  $T_{depr}$  ( $k_{perm}$  sensitivity analysis).

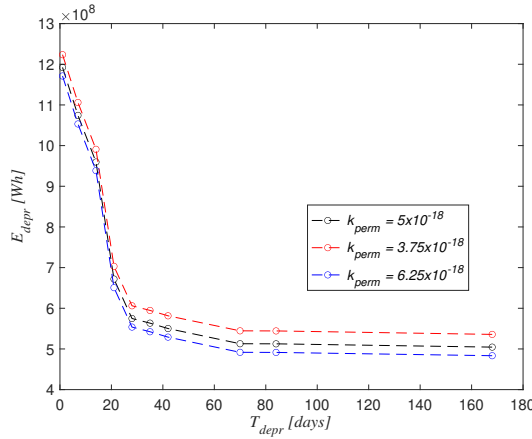


Figure 3.36: Dependency of the tube depressurization energy,  $E_{depr}$ , with  $T_{depr}$  ( $k_{perm}$  sensitivity analysis).

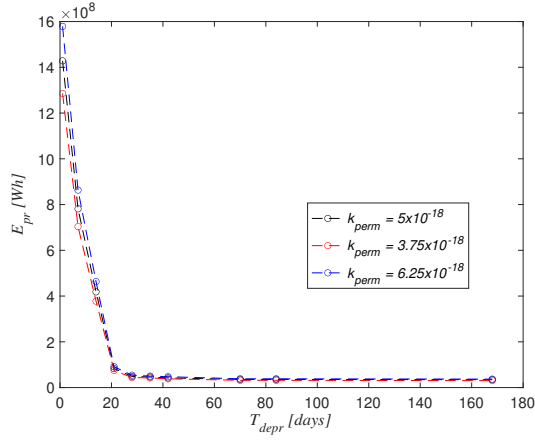


Figure 3.37: Dependency of the air leaks compensation energy,  $E_{pr}$ , with  $T_{depr}$  ( $k_{perm}$  sensitivity analysis).

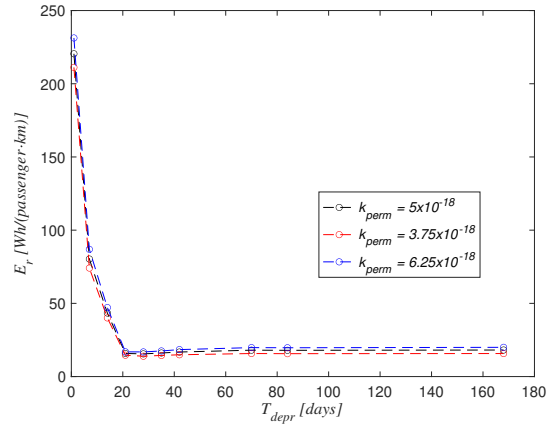


Figure 3.39: Total energy need per number of passengers and per km,  $E_r$ , as a function of  $T_{depr}$  for each trajectory length ( $k_{perm}$  sensitivity analysis).

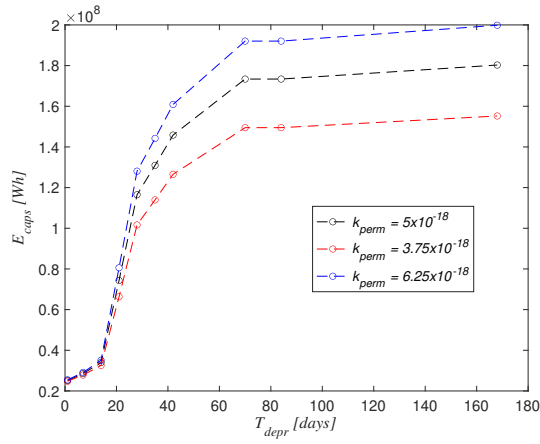


Figure 3.38: Dependency of capsules network energy,  $E_{caps}$ , with  $T_{depr}$  ( $k_{perm}$  sensitivity analysis).

**Variable  $m_0$  (passive mass of the capsule)**

As for the other parameters, the sensitivity analysis is carried out by varying the original value assumed for  $m_0$  (i.e.,  $6000\text{kg}$  for the passive mechanics +  $4000\text{kg}$  for the passengers =  $10000\text{kg}$ ) by adding a weight of 20% and 40% more with respect to the original value assumed for this parameter, namely: (i)  $m_0 = 12000\text{kg}$  and (ii)  $m_0 = 14000\text{kg}$ .

Fig. 3.40 shows that the optimisation problem identifies solutions with a difference in the tube pressure of about 20% with respect to the results obtained with the original value of  $m_0$ . The energy consumption of the capsules,  $E_{caps}$ , is correspondingly decreased by 6% with respect to the results obtained with the original value of  $m_0$  as shown in Fig. 3.41. The reduction of the energy needed by the capsules is shifted in a corresponding increase of the energy needed by the infrastructure ( $E_{depr}$  and  $E_{pr}$  shown in Fig. 3.42 and Fig. 3.43) respectively. The overall result is, however, unchanged as the optimization identifies operating conditions for which the energy per-passenger-per-km remains practically the same compared to the one obtained in correspondence of the original mass  $m_0$  as shown in Fig. 3.44.

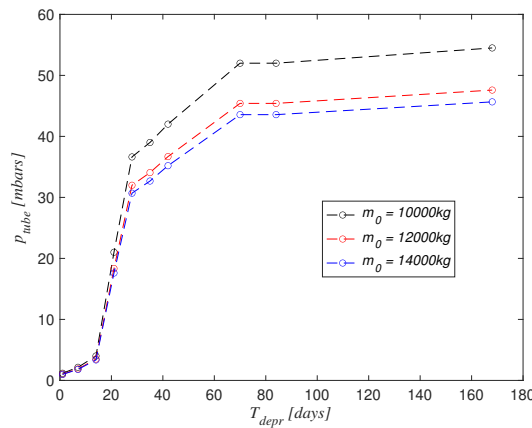


Figure 3.40: Dependency of the optimal operational internal pressure of the tube,  $p_{tube}$ , with  $T_{depr}$  ( $m_0$  sensitivity analysis).

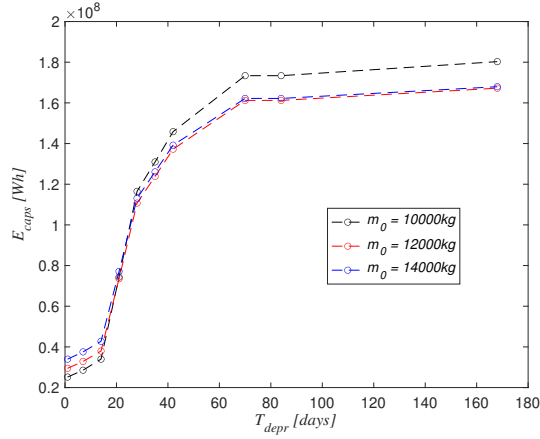


Figure 3.41: Dependency of capsules network energy,  $E_{caps}$ , with  $T_{depr}$  ( $m_0$  sensitivity analysis).

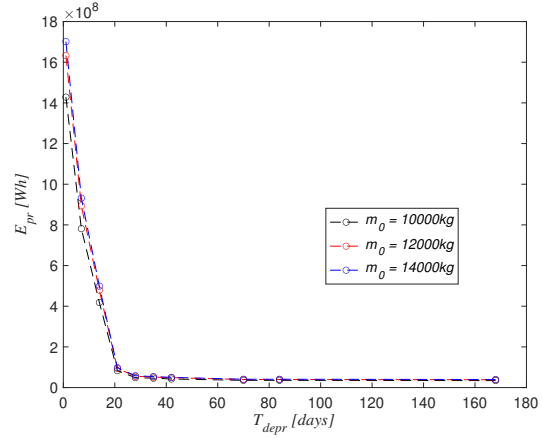


Figure 3.43: Dependency of the air leaks compensation energy,  $E_{pr}$ , with  $T_{depr}$  ( $m_0$  sensitivity analysis).

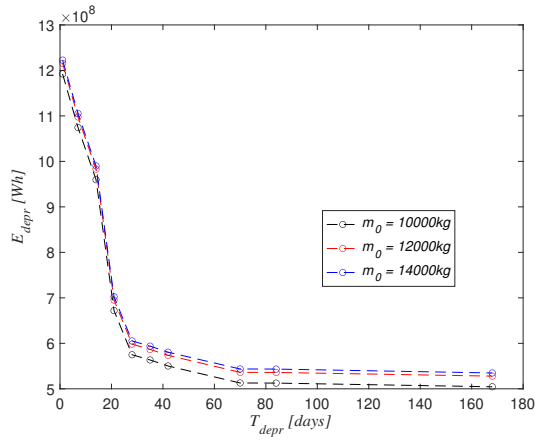


Figure 3.42: Dependency of the tube depressurization energy,  $E_{depr}$ , with  $T_{depr}$  ( $m_0$  sensitivity analysis).

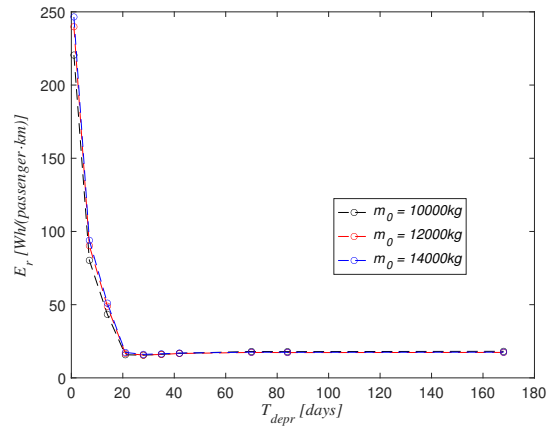


Figure 3.44: Total energy need per number of passengers and per km,  $E_r$ , as a function of  $T_{depr}$  for each trajectory length ( $m_0$  sensitivity analysis).



**Variables  $\eta_{LIM}(v)$ ,  $\cos(\phi)(v)$  (LIM efficiency and power factory expressed as a function of the capsule's speed)**

The efficiency ( $\eta_{LIM}$ ) and power factor ( $\cos(\phi)$ ) of a high-speed LIM designed at the Authors' laboratory for hyperloop applications are shown here below as a function of the capsule speed (see Fig. 3.45 and Fig. 3.46). In the optimisation problem (3.12), instead of using constant values, these two functions we have been imposed for the LIM's efficiency and power factor as a function of the speed of the capsule. However, in order to define the VSI's mass, the minimum value of  $\cos(\phi)$  has been considered (i.e.,  $\cos(\phi) = 0.47$ ), and not the average value (i.e.,  $\cos(\phi) = 0.6$ ). This creates the largest mass of the VSI as defined in (3.5). As shown in Fig. 3.47, the proposed optimization identifies a lower tube pressure (in the range of  $-15\%$ ) with respect to the results obtained for  $\eta_{LIM} = 0.65$  and  $\cos(\phi) = 0.6$ . The lower tube operating pressure is identified to compensate for the larger losses in the capsule propulsion system associated to  $\eta_{LIM}(v)$ ,  $\cos(\phi)(v)$ . Indeed, the energy needed for the capsules,  $E_{caps}$ , exhibit an increase of 20% as shown in Fig. 3.48 while the energy needed by the infrastructure,  $E_{depr} + E_{pr}$ , remains practically unvaried as shown by Fig. 3.49 and Fig. 3.50. As shown in Fig. 3.51, the energy per-passenger-per-km exhibit a small increase with respect to the results obtained for  $\eta_{LIM} = 0.65$  and  $\cos(\phi) = 0.6$ .

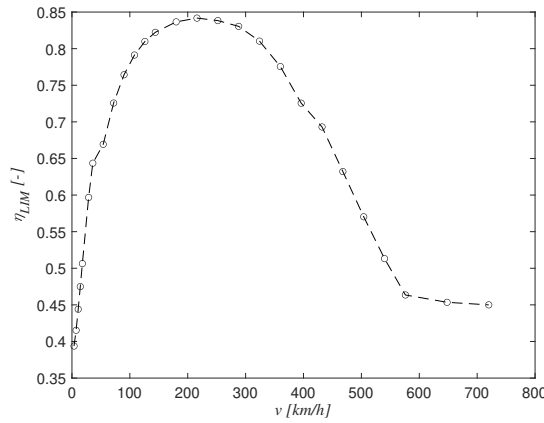


Figure 3.45: Dependency of the LIM's efficiency,  $\eta_{LIM}$ , with the speed of the capsule,  $v$ .

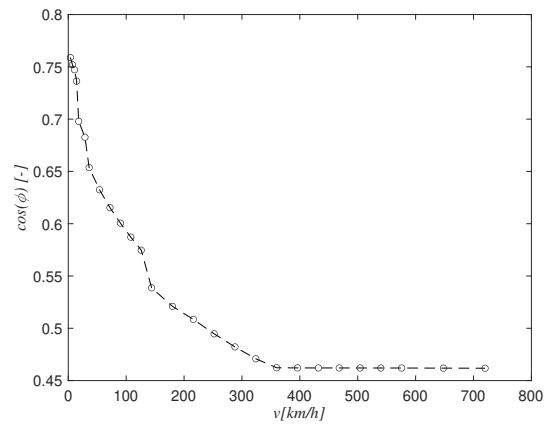


Figure 3.46: Dependency of the VSI's power factor,  $\cos(\phi)$ , with the speed of the capsule,  $v$ .

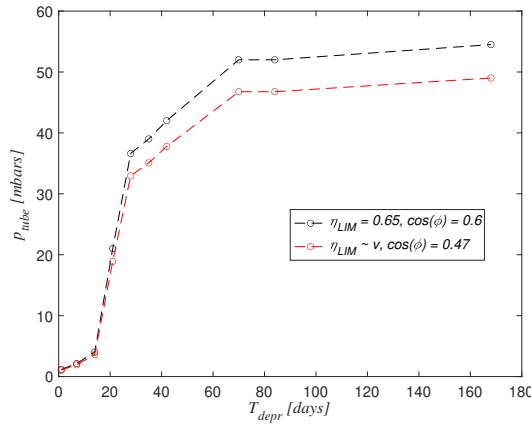


Figure 3.47: Dependency of the optimal operational internal pressure of the tube,  $p_{tube}$ , with  $T_{depr}$  (propulsion sensitivity analysis).

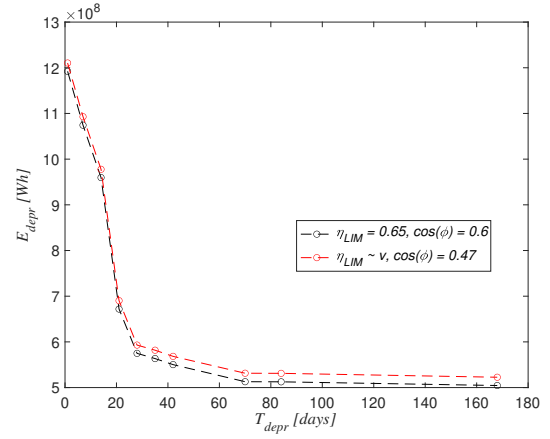


Figure 3.49: Dependency of the tube depressurization energy,  $E_{depr}$ , with  $T_{depr}$  (propulsion sensitivity analysis).

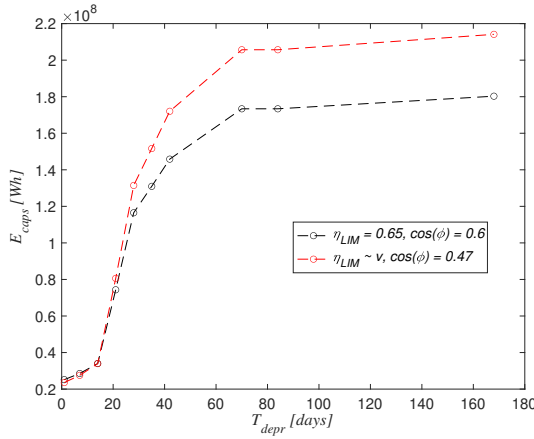


Figure 3.48: Dependency of capsules network energy,  $E_{caps}$ , with  $T_{depr}$  (propulsion sensitivity analysis).

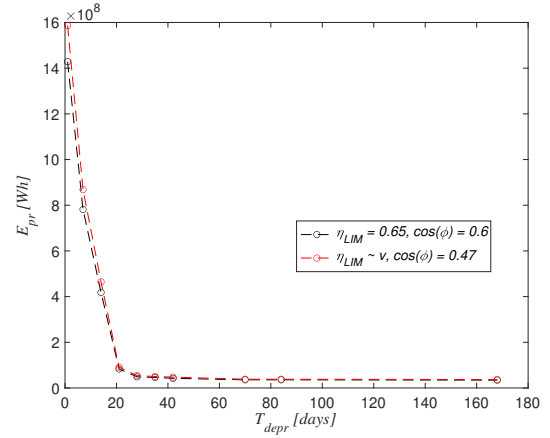


Figure 3.50: Dependency of the air leaks compensation energy,  $E_{pr}$ , with  $T_{depr}$  (propulsion sensitivity analysis).

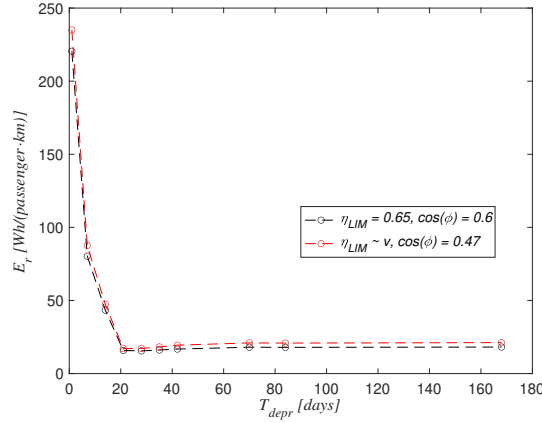


Figure 3.51: Total energy need per number of passengers and per km,  $E_r$ , as a function of  $T_{depr}$  for each trajectory length (propulsion sensitivity analysis).

Indeed, another representation of the PS model embedding the variation of  $\eta_{LIM}$  can be formulated as function of the LIM slip. However, we opted to use the dependency of  $\eta_{LIM}$  with  $v$  as our objective is a system-level design.

### 3.5.8 Use of Compressor

In order to increase the maximum potential speed of the capsules in hyperloop tubes by increasing the flow's cross section ( $S_{tube} - S$ ), a compressor might be considered to be placed in front of the capsule. In order to increase the pressure in the tube by a factor of 2 (e.g.  $0.02bar$  instead of  $0.01bar$ ), the compressor should suck part of the air in front of the tube and bypass it inside the capsule before letting it escaping from the back of the capsule. For the calculation, we assume that half of the air present in front of the tube is sucked by the compressor and send it to the bypass having a cross section area that is half of the capsule surrounding area, meaning a blockage ratio of 2. Therefore, assuming:

- Percentage of air bypassed through the compressor = 50%
- Compressor ratio = 2
- Tube diameter =  $4m$
- Volume of 1m of length of the tube =  $12.6m^3$
- Speed of the capsule =  $800 \frac{km}{h}$  (increased due to the increase of the flow's surface)
- Pressure in the tube =  $0.02bar$
- Air density =  $1.2 \frac{kg}{m^3}$
- Air density at tube pressure =  $0.024 \frac{kg}{m^3}$
- Efficiency of the compressor = 80%
- Temperature in the tube =  $20^\circ C$

For an isothermal compressor, the power calculation would be:

The capsule will cross  $2793m^3$  of air. If we consider that 50% will go in the bypass, it means that  $1396m^3$  of air should pass through the compressor. Considering the air density, the mass of air passing through the compressor per second,  $q_m = 34 \frac{kg}{s}$ , temperature in the tube,  $T_{te} = 20^\circ C$ , and  $r = \frac{R}{M} = 287 Jkg^{-1}K^{-1}$ , the ratio between the universal constant,  $R$ , and molar mass of the gas with a increased pressure factor of  $fact = 2$  as mentioned above, the power of the compressor,  $P_{compressor}$ , is calculated in (3.19):

$$P_{compressor} = \frac{q_m \cdot r \cdot T_{te} \cdot \ln(fact)}{\eta_{compressor}} \quad (3.19)$$

With the above mentioned numerical values,  $P_{compressor} = 2.5MW$ . It is interesting to note that, at cruising speed, the capsule propulsion system requires few hundreds of  $kW$  (see Fig. 3.17) and the amount of power required by the compressor shows that the power needed to reduce the air drag of the capsule by a factor of 2, at  $20mbars$ , is significant and incompatible with the capsule energy consumption. Therefore, a compressor or a turbofan may largely increase the energy reservoir of the capsule to unrealistic values and, furthermore, it can be also a heat generator in the low-pressure environment of the tube.

### 3.6 Conclusions

In this chapter, we have proposed an operational-driven optimal-design framework of a hyperloop system. The framework is capable of addressing fundamental questions related to the design of this new transportation mode, namely: (i) assess the optimal pressure inside a hyperloop tube to minimize its global energy consumption; (ii) determine the minimal energy need passenger and per km, (iii) understand whether there is a strong link between the infrastructure operation and the capsule's design, (iv) understand whether, or not, a magnetic levitation system affects the energy consumption of the capsule and (v) understand if a compressor can be used for a hyperloop capsule in order to assess the energy efficiency.

In this respect, we have proposed a comprehensive optimisation framework capable of linking the operation of a network of hyperloop capsules, the model of the hyperloop infrastructure and the model of the capsule's propulsion and kinematics in view of the inherent coupling between the tube environmental conditions (i.e., its operational pressure) and the motion of the capsules along the trajectory.

We have quantified the (strong) impact of the operational strategy of the hyperloop infrastructure on the energy consumption of the entire system. More specifically, for depressurization periods in the range of few days, the energy/passenger/km can reach high values (especially for long trajectories) with best values in the range of  $100 - 225 \frac{Wh}{passenger \cdot km}$ . Therefore, the first conclusion is to enforce depressurization periods  $\geq 21 days$  as, depending on the length of the trajectory, the energy/passenger/km can fall in the range between  $[20, 30] \frac{Wh}{passenger \cdot km}$ , thus making this transportation mode energy-competitive with respect to electric trains. Indeed, we have shown that for values of depressurization periods in the order of few days, the dominant use of energy is given by both process energy and depressurization energy, and for values of depressurization periods in the range between  $42 days$  to  $168 days$ , the energy need of the infrastructure is of the same order of magnitude of the energy used by the capsules. For higher values of depressurization periods, the energy used by the capsules becomes dominant.

Regarding the capsule's optimal cruising speed, the obtained results have shown that, in order to minimise the total energy required by the whole hyperloop system, the capsules have to travel at a sub-sonic speed.

The proposed framework has also allowed to determine the optimal pressures inside the tube to be in the range from  $2.82 mbar$  to  $76.92 mbar$  for a length of trajectory of  $226 km$ , from  $1.17 mbar$  to  $54.5 mbar$  for a length of trajectory of  $500 km$  and from  $1.14 mbar$  to  $17.25 mbar$  for a length of trajectory of  $1000 km$ . Note that, for the same value of depressurization period, the optimisation problem determines the increasing tube operating pressures for larger trajectory length.

Furthermore, the proposed optimisation has shown that the magnetic levitation is responsible of a dramatic increase the capsule's masses, energy needs as well as peak power requirements. Therefore, it is quite clear from these results that hyperloop capsules have to rely on drag-less

magnetic levitation solutions especially if the energy reservoir is embedded in the capsule.

On the same note, we have shown that carrying an on-board compressor, it will dramatically increase the power consumption. To fix ideas, at the coasting speed, the power consumption is expected to be one order of magnitude higher than without having an on-board compressor.

Compared to other electrical transportation modes, such as electrical vehicles (EVs) and electrical trains (ETs), the obtained results have shown that hyperloop represents an energy-efficient and high-speed solution. Such a conclusion is supported by the Gabrielli-Kármán diagram shown in Fig. 3.52 where the best energy need per-passenger-per-km obtained in this paper for the hyperloop system are compared with the corresponding values for ETs and EVs taken from Ruangjirakit [6] and Andersson [8]. Indeed, for a similar or lower values of energy need per-passenger-per-km, the hyperloop system can offer higher maximum speeds compared to the other two main electrical transportation modes making it a viable solution for intra-continental travels.

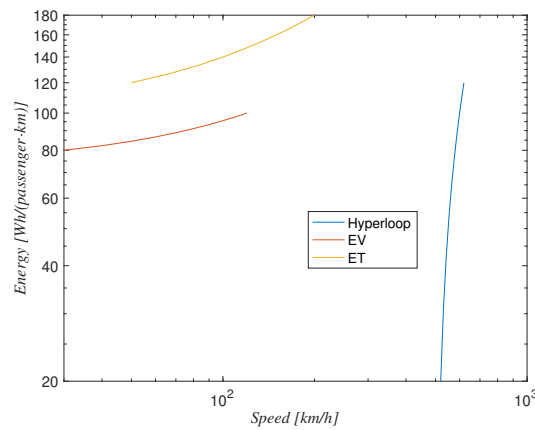


Figure 3.52: Gabrielli-Kármán diagram showing the comparison of hyperloop with electrical vehicles and electrical trains

It is worth noting that, for speed values close to  $500 \frac{km}{h}$ , the energy/passenger/km needs of a hyperloop system drops to values of  $20 - 30 Wh/passenger/km$ . At speed values close to  $600 \frac{km}{h}$ , the energy needs increase to values up to  $120 Wh/passenger/km$ . This value is similar for ETs and EVs, but with lower speeds (i.e.,  $100 - 200 \frac{km}{h}$ ).

Since the results shown in this chapter are the results of numerical simulations, they should be validated experimentally. However, realizing a full-scale hyperloop experiment is technically challenging and extremely expensive. Therefore, in the next chapter, a process to reduce the scale of a hyperloop system is presented.





## 4 Design of a Hyperloop System MockUp

©2022 IEEE

Reprinted from: D. Tudor, M. Paolone, T. Govoni, M. Leipold, “Design of a Hyperloop System MockUp, ” in *IEEE International Conference on Intelligent Transportation Systems (ITSC)*, 2022, (accepted, but not yet published)

The thorough development of the hyperloop system does require the availability of reduced-scale models. They can be used for the fast prototyping of various components, as well as for studying critical phenomena that takes place in this peculiar transportation system without the need to develop complex and expensive full-scale setups. In our case, the purpose is to develop a reduced scale hyperloop system to validate the findings of Chapter 3. In this respect, in this chapter, we present a process for the optimal assessment of the scaling factor; it is to be used for the development of a reduced-scale hyperloop model, starting from the knowledge of the technical characteristics of its full-scale counterpart.

The objective of the proposed process is the minimisation of the difference between the normalized power profiles associated with the reduced-scale and full-scale models of a hyperloop capsule traveling along a pre-defined trajectory with a pre-determined speed profile. By considering the hyperloop full-scale model as a reference, we propose a set of equations that link the above-mentioned metric with the constraints dictated by the kinematics of the hyperloop capsule, the capsule's battery-energy storage and propulsion systems, the capsule's aerodynamics, and the operating environmental conditions. We then derive a closed-form expression for the assessment of the optimal scaling factor and eventually use it to study the scaled-down version of an application example of a realistic hyperloop system.

### 4.1 Introduction and Literature Review

The use of reduced-scale (RS) model testing has been extensively adopted in several engineering disciplines to predict the behaviour of full-scale (FS) devices and structures by studying their equivalent RS models. The RS-model testing represents an efficient approach not only to

reduce the cost of FS-model development but also to support fast prototyping and to study critical phenomena on the RS model before the FS model is built.

The RS-model testing relies on the similitude of physical laws, which enables the rigorous definition of the necessary conditions for designing an RS model that is equivalent to its FS counterpart. Examples of similitude laws apply to the testing of hydraulic machines [76], wind-turbine fluid dynamics [77]- [79], rocket-fluid dynamics [80]- [82], and structural engineering [83] to mention a few. With respect to the development of hyperloop systems, the use of RS models is fundamental in order to develop several components of the capsule (e.g., its propulsion system), as well as to study the influence of the operation of the infrastructure on the energy need of the whole system. A first example related to the definition of a hyperloop RS model is discussed in [84]. In this chapter, the authors were interested in studying the vehicle dynamics via the development of a 1/10 scale model. By relying on the dynamic-motion similarity laws, the authors of this study investigated vertical and lateral motions of a hyperloop capsule to infer its complete dynamic characterization and to validate a corresponding numerical model.

To the best of our knowledge, the current literature has not defined suitable RS models of the whole hyperloop system in order to study the capsules' propulsion and its link with the operation of the hyperloop infrastructure. In this respect, we fill this gap by proposing a method that computes the optimal scaling factor of the physical characteristics of the capsule by taking into account the model of the hyperloop infrastructure and the model of the capsule's propulsion and kinematics as presented in Chapter 2 and Chapter 3.

As the physics laws governing the various components of a hyperloop exhibit different behaviours, with respect to a dimensional scaling process, we analyse this first fundamental aspect. The main physical phenomena that are considered are the kinematics of the hyperloop capsule, the capsule's battery-energy storage system (BESS), the propulsion system (PS), the capsule's aerodynamics, and the operating environmental conditions. We introduce and justify the metric given by the normalized aerodynamics losses, with respect to the maximum BESS power output. The link of this metric with the models of the above-mentioned physical phenomena, and with the scaling factor, results in a closed-form equation that enables the assessment of the optimal scaling factor between the FS and the RS capsules' models.

The structure of the chapter is as follows: in Section 4.2, we recall the main physical phenomena that govern the FS hyperloop model with particular references to the capsule's kinematics, BESS, PS, and aerodynamics. In Section 4.3, we describe the RS model. In Section 4.4, we first introduce and justify the metric used by the scaling process; then, we illustrate the process of analytically linking the proposed metric with the FS and RS models for the optimal assessment of the scaling factor. In Section 4.5, we illustrate an application example related to a scaling process of a realistic hyperloop system. In the last section, we conclude the chapter with our final remarks and observations regarding the applicability of the proposed process.

## 4.2 Full-Scale Hyperloop System

### 4.2.1 Hyperloop General Characteristics

As already discussed, the hyperloop is a new transportation system where vehicles travel along pre-determined trajectories and in a dedicated/confined environment (i.e., tunnels or tubes), where the pressure is kept at relatively low values (i.e., in the range of tens of mbars). As largely discussed in the previous chapters, these aspects are very specific to the hyperloop system hence largely differentiate it from existing modes of transportation that do not permanently isolate vehicles from the external environment. Furthermore, there is the possibility of optimally controlling the pressure in a hyperloop confined environment, in conjunction with the off-line optimisation of the speed profile of the capsules. This pressure control can substantially reduce the energy needs for the operation of the whole system, thus making it the most energy-efficient transportation system for intra-continental travels.

Nevertheless, even if the pressure is reduced to relatively low values, there are still some hard limitations. Indeed, the maximum speed of hyperloop capsules is limited by two main factors. The first is the ratio between the capsule's cross sections and that of the tube must be limited to ensure the flow around the capsule as it is subsonic. The second factor is the associated drag coefficient, as it limits the capsule's cruising speed for a given traction power (Indeed, such a dependency largely influences the energy required by the capsules, especially when approaching near-sonic speeds). In the following sub-sections, we first recall the limitations associated with the main aerodynamic phenomena in this system. Then, we give the fundamental equations to represent the FS hyperloop model as they are used later in the Chapter to derive the scaling process.

### 4.2.2 Aerodynamic Limitations of the Hyperloop System

The hyperloop is a complex system and the definition of the RS model characteristics requires macroscopic/integral models that are subsequently translated into a specific design of the RS model.

Regarding the aerodynamics, even if a hyperloop capsule in a tube does not have an axis-symmetric geometry, the physical phenomena regarding the flow can be studied by looking at a simplified geometry allowing to study the compression of the flow around the capsule due to the reduction of the available area. Indeed, the fluid-compressibility effects play a major role in the design of high-speed hyperloop capsules as they travel in a confined environment. Indeed, as the objective is to keep the fluid around the capsule in a subsonic regime in order to limit energy consumption, the capsules' and tubes' cross sections, and/or the maximum speeds, are constrained by the compressibility of the air near the capsule. This phenomenon, called Kantrowitz Limit, is well-known. In this paper, we consider capsules' speeds between  $400 \frac{km}{h}$  –  $780 \frac{km}{h}$  as shown in the last Chapter.

### Problem Definition

A 2D slice of the 3D problem can be considered and studied as a fluid flow accelerating in a converging nozzle. The following assumptions are made:

- 2D steady flow;
- unidirectional flow;
- isentropic compression;
- constant heat capacity ratio of air (i.e.,  $\gamma_{air} = 1.4032$ );
- constant specific gas constant (i.e.,  $r_{air} = 287[\frac{J}{kg \cdot K}]$ );

The geometry of the problem is represented in Fig. 4.1, where  $S_{fs}^{tube}$  represents the FS cross section of the tube<sup>I</sup>,  $S_{fs}^{capsule}$ <sup>II</sup> represents the FS cross section of the capsule, and  $A_{ext}$  represents the difference between  $S_{fs}^{tube}$  and  $S_{fs}^{capsule}$ .

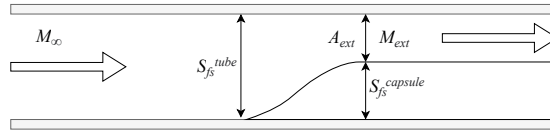


Figure 4.1: Schematic 2D representation of a hyperloop capsule traveling in a tube.

The Mach number of the far-field flow,  $M_\infty$ , can be related to (i) the speed of the capsule,  $v_{fs}$ <sup>III</sup>, and (ii) the speed of sound in the tube,  $v_{sound} = \sqrt{\gamma \cdot r_{air} \cdot T_\infty}$ , where  $T_\infty$  represents the temperature of the tube's environment. Therefore, the expression of  $M_\infty$  is given here below.

$$M_\infty = \frac{v_{fs}}{\sqrt{\gamma \cdot r_{air} \cdot T_\infty}} \quad (4.1)$$

As the flow encounters the capsule, the cross-section available for the flow decreases. This process leads to the acceleration of the flow's speed around the capsule that, in view of the previous considerations, needs to stay subsonic.

### Limiting Area Ratio

The main objective is to determine  $A_{ext} = A_{ext}^{sonic}$ . In [63] and [85], the cross section's ratio, at which the flow becomes sonic as a function of the far-field flow Mach number, is derived and

<sup>I</sup>the same variable in Chapter 3 was named  $S_{tube}$

<sup>II</sup>the same variable in Chapter 3 was named  $S$

<sup>III</sup>the same variable in Chapter 3 was named  $v$

recalled in (4.2).

$$\frac{S_{fs}^{tube}}{A_{ext}^*} = \frac{1}{M_\infty} \left[ \frac{2}{\gamma+1} \left( 1 + \frac{\gamma-1}{2} M_\infty \right) \right]^{\frac{\gamma+1}{2(\gamma-1)}} \quad (4.2)$$

Considering  $S_{fs}^{tube} = S_{fs}^{capsule} + A_{ext}$  and  $S_{ratio} = \frac{S_{fs}^{capsule}}{S_{fs}^{tube}}$ , we need to determine  $S_{ratio}$  as a function of  $M_\infty$  for a given internal tube temperature,  $T_\infty$ . The main constraint is to ensure that, for a given cross section's ratio, the flow remains subsonic everywhere around the capsule.

By referring to the Mach number limit, we need to have the airflow around the capsule cross section such as  $M_{ext} = M_{lim}$ . For instance, if  $M_{lim} = 1$ , this means we have reached the isotropic limit. Therefore, we can derive the relation that provides the dependency of  $S_{ratio}$  with  $M_\infty$  and  $M_{lim}$ , as in (4.3).

$$S_{ratio} = 1 - \frac{\frac{1}{M_{lim}} \left[ \frac{2}{\gamma+1} \left( 1 + \frac{\gamma-1}{2} M_{lim} \right) \right]^{\frac{\gamma+1}{2(\gamma-1)}}}{\frac{1}{M_\infty} \left[ \frac{2}{\gamma+1} \left( 1 + \frac{\gamma-1}{2} M_\infty \right) \right]^{\frac{\gamma+1}{2(\gamma-1)}}} \quad (4.3)$$

Fig. 3.6 shows the dependency of  $S_{ratio}$  with  $M_\infty$  and  $M_{lim}$ .

#### 4.2.3 Model of the Capsule's Propulsion System

The FS tube's and capsule's models and parameters are adapted from Chapter 3. The air-density of the full-scale infrastructure is  $\rho_{fs}$ , and the pressure inside the FS tube is  $p_{tube}^{fs}$  (considered in Chapter 3 as being  $p_{tube}$ ).  $a_{fs}$  represents the acceleration profile of the FS capsule model.

We assume that the cross section of the tube is circular. We consider a model with only one capsule in the tube.

#### Capsule's Trajectory and Kinematic Models

The trajectory and kinematic models of the capsule are considered as in Chapter 3, Section 3.2.2.

#### Capsule's PS Model

The PS model parameters are defined in Chapter 3, Section 3.2.2.

The total mass of the FS capsule,  $m_{fs}^{IV}$  can be derived as a function of the aforementioned main capsule's parameters as in (4.4), where  $\eta_{tr}$  represents the supplementary power transfer efficiency from BESS to LIM (i.e., the efficiency of the power electronics converter).

$$m_{fs} = m_0 + N_s N_p m_{cell} + \frac{1}{\eta_{tr}} P_{maxCell} N_s N_p k_1 + \frac{1}{\eta_{tr} \cos(\phi)} P_{maxCell} N_s N_p k_2 \quad (4.4)$$

We can also easily define the power losses associated with the aerodynamic drag force of the FS capsule,  $P_{drag}^{fs}$ , as in (4.5) (where  $C_D^{fs}$  is the drag coefficient that is a function of  $v_{fs}^V$ ). As this force is a function of the capsule's speed, it has to be defined for every discrete position, along the trajectory, of the capsule .

$$P_{drag}^{fs}(j) = \frac{1}{2} S_{fs}^{capsule} C_D^{fs}(v) \rho_{fs} v_{fs}^3(j) \quad (4.5)$$

Then, we can derive the mechanical power of the FS capsule necessary for propelling it in order to track the speed/acceleration profiles. It is worth noting that the magnetic drag has been disregarded as thrust and levitation are supposed to be both provided by the LIM as proposed in [86] - [89].

$$P_{tr}^{fs}(j) = m_{fs} a_{fs}(j) v_{fs}(j) + P_{drag}^{fs}(j) \quad (4.6)$$

Finally, the electrical power that has to be provided by the BESS of the FS capsule,  $P_{batt}^{fs}$ , can be directly related to  $P_{tr}^{fs}$  through the efficiency of the LIM,  $\eta_{LIM}$ .

$$P_{batt}^{fs}(j) = \frac{P_{tr}^{fs}(j)}{\eta_{LIM}} \quad (4.7)$$

### 4.3 Reduced-Scale Model of a Hyperloop System

This section describes how key physical phenomena of the hyperloop system are scaled-down. We refer, in particular, to the capsule's (i) masses, (ii) kinematic model, (iii) power profiles, (iv) BESS energy capacity, and (v) aerodynamics.

<sup>IV</sup>the same variable was named  $m$  in Chapter 3

<sup>V</sup>Note that  $C_D^{fs}$  is a function of  $Re$  for given (i.e., fixed)  $v_{fs}$  and  $S_{fs}^{capsule}$ .

More specifically, we first introduce the definition of the scaling factor. Then, we discuss the scaling of the capsule's kinematic model, its masses, power profiles, and environment operating conditions. We separately discuss the scaling of the capsule's aerodynamics, as it requires a dedicated section, in view of the need for numerical assessing its dependency with the scaling factor and the capsule's speed.

#### 4.3.1 Scaling of the Capsule's Kinematic Model, Masses, Power Profiles, and Environment

Let  $k \in \mathbb{R}^+$  the scale factor, with  $k > 1$ . Distances, speeds, accelerations, time and masses of the RS model, as well as environmental conditions, power profiles, and BESS energy capacity, can be derived in a straightforward way.

##### Distances, Speeds, Accelerations, Time, and Masses

As the times of the RS and FS models are unaltered by the scaling process, the kinematic quantities of the capsule's RS model can be directly linked to the corresponding ones of the FS model, as in (4.8).

$$\begin{cases} t_L^{rs} = t_L^{fs} \\ v_{rs} = \frac{v_{fs}}{k} \\ a_{rs} = \frac{a_{fs}}{k} \\ L_{rs} = \frac{L_{fs}}{k} \end{cases} \quad (4.8)$$

Regarding the masses of the RS model, as in [84], [90]- [92], we assume that the components of the capsule have to maintain the same relative density factor of their materials. As the RS and FS models are characterised by materials with the same volumetric densities, the overall mass of the capsule RS model,  $m_{rs}$ , is inversely proportional to the cube of the scaling factor times the mass of the capsule FS model,  $m_{fs}$  (see (4.9)). In other words, the overall mass of the RS capsule model scales-down like its overall volume.

$$m_{rs} = \frac{m_{fs}}{k^3} \quad (4.9)$$

##### Tube Environment

The operational conditions of the RS tube, namely the air-density  $\rho_{rs}$  and temperature, are assumed to be identical to those of the FS. The same consideration applies to the tube's pressure,  $p_{tube}^{rs}$ . The RS cross section of the tube varies with the FS cross section of the tube,

as shown in (4.10).

$$\begin{cases} \rho_{rs} = \rho_{fs} \\ p_{tube}^{rs} = p_{tube}^{fs} \\ S_{tube}^{rs} = \frac{S_{tube}^{fs}}{k^2} \end{cases} \quad (4.10)$$

### Powers

The power losses due to the aerodynamic drag force in the RS model can be defined similarly to (4.5), for every discrete position of the capsule along the RS trajectory and, as a function of the RS model, the drag coefficient  $C_D^{rs}$  and speed  $v_{rs}$ . Note that, in (4.11), the drag coefficient cannot be directly linked to the RS capsule speed in a closed form. This aspect is discussed in the following sub-section.

$$P_{drag}^{rs}(j) = \frac{1}{2} S_{rs}^{capsule} C_D^{rs}(v) \rho_{rs} v_{rs}^3(j) = \frac{1}{2} \frac{S_{fs}^{capsule}}{k^2} C_D^{rs}(v_{rs}) \rho_{fs} \frac{v_{fs}^3(j)}{k^3} \quad (4.11)$$

The mechanical power of the capsule is defined in (4.12).

$$P_{tr}^{rs}(j) = m_{rs} a_{rs}(j) v_{rs}(j) + P_{drag}^{rs}(j) = \frac{m_{fs}}{k^3} \frac{a_{fs}(j) v_{fs}(j)}{k^2} + P_{drag}^{rs}(j) \quad (4.12)$$

As for the FS model, the electrical power provided by the BESS RS model,  $P_{batt}^{rs}$ , is directly related to  $P_{tr}^{rs}$  through the VSI power-transfer efficiency,  $\eta_{VSI}$ , and the LIM-to-traction power-transfer efficiency,  $\eta_{LIM}$ . As we will see later, the values of these two efficiencies in the RS and FS models do not play any role. This is shown in (4.13)

$$P_{batt}^{rs}(j) = \frac{P_{tr}^{rs}(j)}{\eta_{LIM}} \quad (4.13)$$

#### 4.3.2 Scaling of the Capsule's Aerodynamics and Drag Coefficient

The drag coefficient of the RS capsule,  $C_D^{rs}$ , is a coefficient that takes into account the flow behaviour around a specific object.  $C_D^{rs}$  models the effects of the pressure and viscous forces parallel to the flow direction exerted on the capsule's surface. Although it can be defined as in (4.14), as a function of the previously introduced quantities and parameters of both RS and FS



models, the drag force  $F_{drag}^{rs}(k, \frac{v_{fs}}{k})$  does not have a closed-form expression that links it to the scaling factor  $k$  (e.g., [80]- [82]). Such a link has to be quantified numerically by means of a dedicated computational fluid dynamics (CFD) analysis as a function of the scaling factor  $k$  or, in another case, determined experimentally.

$$C_D^{rs} = \frac{2 \cdot F_{drag}^{rs}(k, v_{rs})}{\rho_{rs} v_{rs}^2 S_{rs}^{capsule}} = \frac{2 \cdot F_{drag}^{rs}(k, \frac{v_{fs}}{k})}{\rho_{fs} \frac{v_{fs}^2}{k^2} \frac{S_{fs}^{capsule}}{k^2}} \quad (4.14)$$

In this respect, we have carried-out a CFD analysis by using the COMSOL® Multiphysics simulation environment with respect to a discrete set of values of the scaling factor  $k$  that starts (i.e.,  $k = 1$ ) from a given shape of the FS capsule's aeroshell and tube diameter. The single-phase turbulent flow was solved using a Reynolds-averaged Navier-Stokes (RANS) Low Reynolds  $k-\epsilon$  model, because Large Eddy Simulations (LES) were too computationally demanding. We have selected this model because it provides a good compromise between computation time, resources, robustness, and accuracy of results. It is worth saying that a comparison between the two models is beyond the scope of this thesis.

The simulations refer to a steady-state condition at the capsule's cruising speed. Such a condition was selected as the capsule spends the majority of the time in this state.

Section 4.5 contains all the results regarding this specific set of simulations as it enables us to make a numerical quantification of the function  $C_D^{rs}(k)$ .

#### 4.4 Optimal Assessment of the Scaling Factor

In order to optimally determine the scaling factor  $k$ , there is the need to determine a specific metric to be minimised. To define such a metric, there are two fundamental considerations to take into account: (i) the hyperloop system should achieve the least possible energy use per passenger-per-km, and (ii) the high speed achieved by the capsule requires substantial power provided by the on-board BESS. Therefore, the FS and RS capsule models should be characterised by the same energy that is normalised by the maximum power output of the BESS (as this device is the only power source of the capsules). In other words, if we define  $E_{norm}^{fs} = \int \frac{P_{batt}^{fs}(t)}{\max(P_{batt}^{fs}(t))} dt$  as the normalized energy consumption of the FS capsule and  $E_{norm}^{rs} = \int \frac{P_{batt}^{rs}(t)}{\max(P_{batt}^{rs}(t))} dt$  as the normalized energy consumption of a RS capsule, these two values have to be as similar as possible.

As the time for the RS and FS models are unaltered by the scaling process, we can transform the above-mentioned metric in terms of powers provided by the FS and RS capsules' BESSs. In other words, we seek the least difference between the normalised power profiles of the RS and

FS models.

This similarity cannot be guaranteed all along the trajectory (essentially due to the non-linear relations of the power profiles with the scaling factor and capsules' speeds). Therefore, we will require it with respect to the capsule's cruising speed as in (4.15).

$$\min_k \left( \frac{P_{batt}^{rs}(k, v_{max}^{rs})}{\max(P_{batt}^{rs}(k))} - \frac{P_{batt}^{fs}(v_{max}^{fs})}{\max(P_{batt}^{fs})} \right) \quad (4.15)$$

subject to (4.5) – (4.7), (4.10) – (4.13)

In view of (4.11), (4.12), and (4.13), and by recalling that at cruising speed the capsule acceleration is null, the first term of the objective function, say  $T_1$  in (4.15), can be written as in (4.16).

$$\begin{aligned} T_1 &= \frac{P_{batt}^{rs}(k, v_{max}^{rs})}{\max(P_{batt}^{rs}(k))} \\ &= \frac{\frac{P_{tr}^{rs}(k, v_{max}^{rs})}{\eta_{LIM}}}{\frac{P_{tr,max}^{rs}}{\eta_{LIM}}} \\ &= \frac{P_{tr}^{rs}(k, v_{max}^{rs})}{P_{tr,max}^{rs}} \\ &= \frac{S_{fs}^{capsule} C_D^{rs}(k; \frac{v_{max}^{fs}}{k}) \rho_{fs} (v_{max}^{fs})^3}{\max(2m_{fs} a_{fs}(\hat{j}) v_{fs}(\hat{j}) + S_{fs}^{capsule} C_D^{rs}(k; v_{rs}(\hat{j})) \rho_{fs} v_{fs}^3(\hat{j}))} \end{aligned} \quad (4.16)$$

where the index  $\hat{j}$  refers to the position that, along the trajectory, corresponds to the maximum value of the  $P_{batt}^{rs}$ .

In view of (4.5), (4.6), and (4.7), and by recalling that at cruising speed the capsule acceleration is null, the second term of the objective function, say  $T_2$  in (4.15), can be written as in (4.17).

$$\begin{aligned}
T_2 &= \frac{P_{batt}^{fs}(v_{max}^{fs})}{\max(P_{batt}^{fs})} \\
&= \frac{\frac{P_{tr}^{fs}(v_{max}^{fs})}{\eta_{LIM}}}{\frac{P_{tr,max}^{fs}}{\eta_{LIM}}} \\
&= \frac{P_{tr}^{fs}(v_{max}^{fs})}{P_{tr,max}^{fs}} \\
&= \frac{S_{fs}^{capsule} C_D^{fs}(v_{max}^{fs}) \rho_{fs} (v_{max}^{fs})^3}{\max(2m_{fs} a_{fs}(\hat{j}) v_{fs}(\hat{j}) + S_{fs}^{capsule} C_D^{fs}(v_{fs}(\hat{j})) \rho_{fs} v_{fs}^3(\hat{j}))}
\end{aligned} \tag{4.17}$$

Note that, in view of the above, the objective function presented in (4.15) is independent of both the VSI power-transfer efficiency  $\eta_{tr}$  and the LIM-to-traction power-transfer efficiency  $\eta_{LIM}$ , even if these two efficiencies are different in the FS and RS models.

Here, we apply (4.15) to determine the optimal scaling factor for a realistic hyperloop test case.

## 4.5 Application Example

### 4.5.1 Full-Scale Model Assumptions

#### Main Numerical Assumptions

In order to apply the proposed process for inferring the scaling factor, we refer to an FS hyperloop system whose characteristics have been determined with the last optimization problem in Chapter 3. More specifically, (4.18) provides a summary of the main parameter of such a system. Furthermore, Fig. 4.2 shows the FS model acceleration-time profile,  $a_{fs}(i)$ , where the maximum acceleration is slightly below  $1.5 \frac{m}{s^2}$ . Fig. 4.3 shows the reference FS model speed-time profile  $v_{fs}(i)$ , where the maximum (cruising) speed is equal to  $600 \frac{km}{h}$ . In Fig. 4.4, the FS model power-time profile of the traction and BESS, respectively,  $P_{tr}^{fs}(i)$  and  $P_{batt}^{fs}(i)$ , are also presented. The maximum value of  $P_{batt}^{fs}(i)$  along the trajectory is  $6MW$ . Note that the parameter  $C_D^{fs}$  was validated within the CFD simulation, at the given  $v_{max}^{fs}$  speed.

$$\left\{ \begin{array}{l} \eta_{LIM} = 0.65 \\ \eta_{tr} = 0.95 \\ L_{fs} = 500km \\ S_{fs}^{capsule} = 3.14m^2 \\ S_{fs}^{tube} = 12.56m^2 \\ p_{tube}^{fs} = 50.53mbar \\ m_{fs} = 21243.47kg \\ t_L^{fs} = 53.75minutes \\ v_{max}^{fs} = 594.4 \frac{km}{h} \\ C_D^{fs} = 0.51 \end{array} \right. \quad (4.18)$$

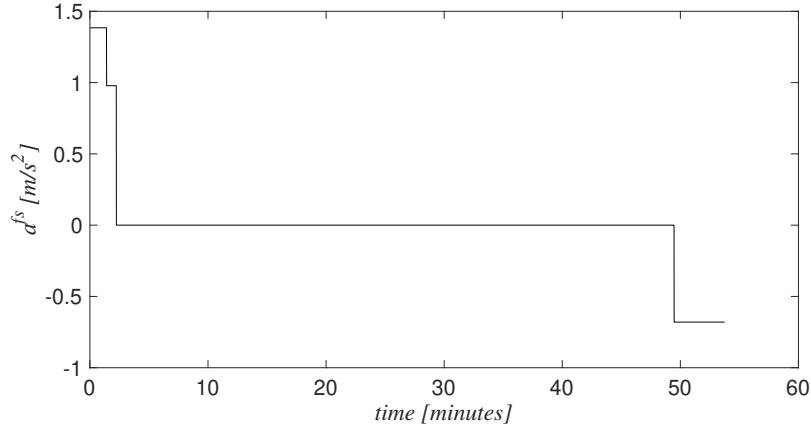


Figure 4.2: FS hyperloop model acceleration profile as a function of time,  $a_{fs}(i)$ , adapted from Chapter 3 for a hyperloop trajectory length  $L_{fs} = 500km$ .

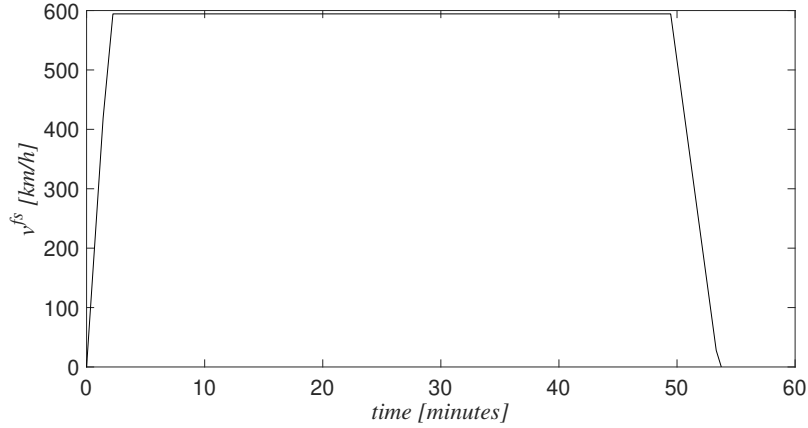


Figure 4.3: FS hyperloop model speed profile as a function of time,  $v_{fs}(i)$ , adapted from Chapter 3 for a hyperloop trajectory length  $L_{fs} = 500\text{km}$ .

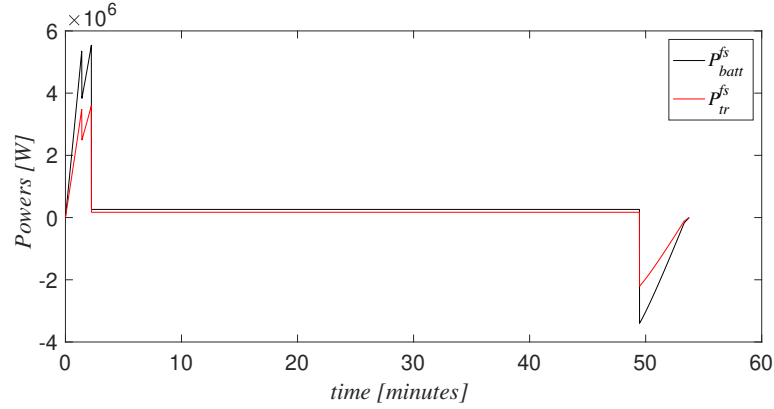


Figure 4.4: FS hyperloop model traction and BESS power profiles as functions of time,  $P_{tr}^{fs}(i)$  and  $P_{batt}^{fs}(i)$ .

#### 4.5.2 Reduced-Scale Model Assumptions

##### Aerodynamics

A hyperloop capsule aeroshell was specifically designed (note that this process is beyond the scope of this thesis) [93]. Its shape is shown in Fig. 4.5.

Specific CFD simulations were carried out with the following assumptions: (i) the simulation domain is composed of a half tube from which the capsule was subtracted (we take advantage of the model symmetry), and (ii) the simulation domain comprises air at  $T_0 = 293.15\text{K}$  ( $t_0 = 20^\circ\text{C}$ ) and  $p_{tube}^{rs} = 50.53\text{mbar}$ .

CFD simulations were carried out for various values of  $k$  to numerically infer the dependency  $C_D^{rs}(k, \frac{v_{max}^{fs}}{k})$ , where the imposed velocity of the air at the inlet of the simulation domain was

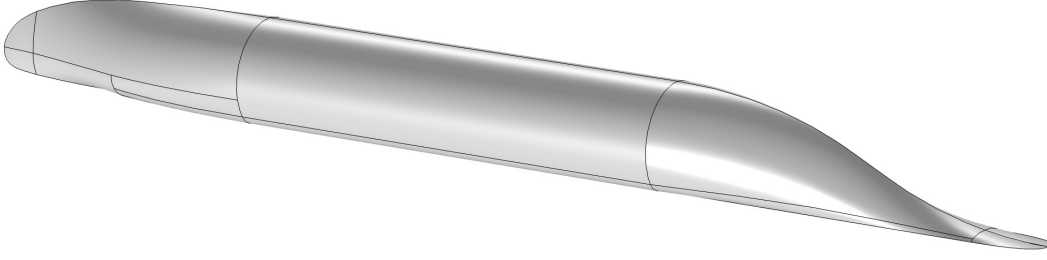


Figure 4.5: Aeroshell model

$k[-]$	$C_D^{rs}[-]$
4	0.4327
5	0.4189
6	0.4188
7	0.4139
9	0.4343
11	0.4668
12	0.5679
14	0.7834
16	0.9156
18	1.0397

Table 4.1: CFD-determined values of  $C_D^{rs}(k, \frac{v_{max}^{fs}}{k})$ .

adapted for each  $k$  as in (4.8). The value of the FS capsule cruising speed,  $v_{max}^{fs}$ , is the one reported in (4.18). The values of  $C_D^{rs}(k, \frac{v_{max}^{fs}}{k})$  for  $k = \{4, 5, 6, 7, 9, 11, 12, 14, 16, 18\}$  are given in Table 4.1. These discrete values of  $C_D^{rs}(k, \frac{v_{max}^{fs}}{k})$  were linearly interpolated as shown in Fig. 4.6. The sudden increase in drag coefficient, as a function of  $k$  for values larger than  $k = 11$ , can be interpreted as the transition to a laminar-flow field around the RS model. The skin-friction drag becomes predominant no matter the shape of the aeroshell, as it is an intrinsic limitation of the scaling process.

### 4.5.3 Results

The values of the objective function of the problem (4.15) are shown in Fig. 4.7. Any RS model with  $4 \leq k \leq 11$  can produce satisfactory results, with respect to the minimisation of the metric proposed in the paper.

The normalized-power profiles, as functions of time, are shown in Fig. 4.8 for different values of the scaling factor (the FS normalised power profile, i.e., for  $k = 1$ , is reported as well). In Fig. 4.9 and in Fig. 4.10 are presented the cross sections of the RS model, respectively the lengths of trajectory associated with the scaling factor,  $k$ .

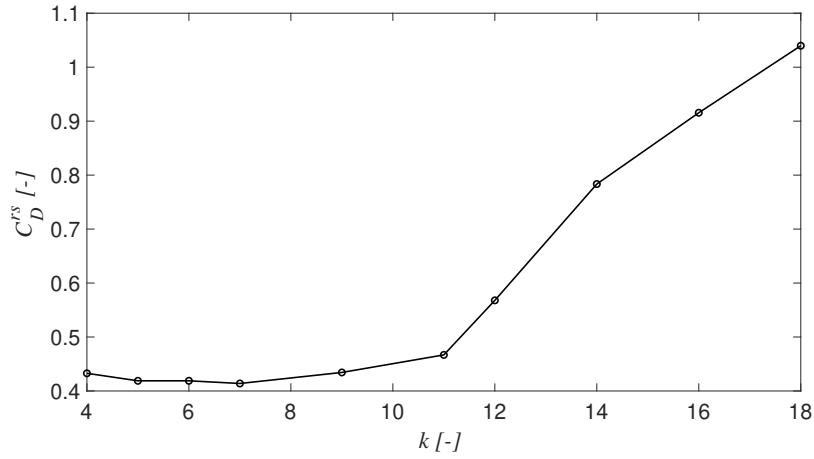


Figure 4.6: Interpolated values of  $C_D^{rs}(k, \frac{v_{max}^{fs}}{k})$  for various values of the scaling factor,  $k$ .

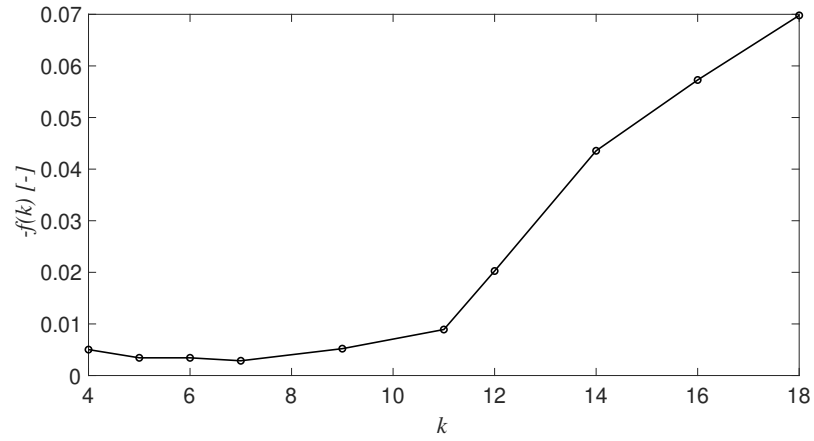
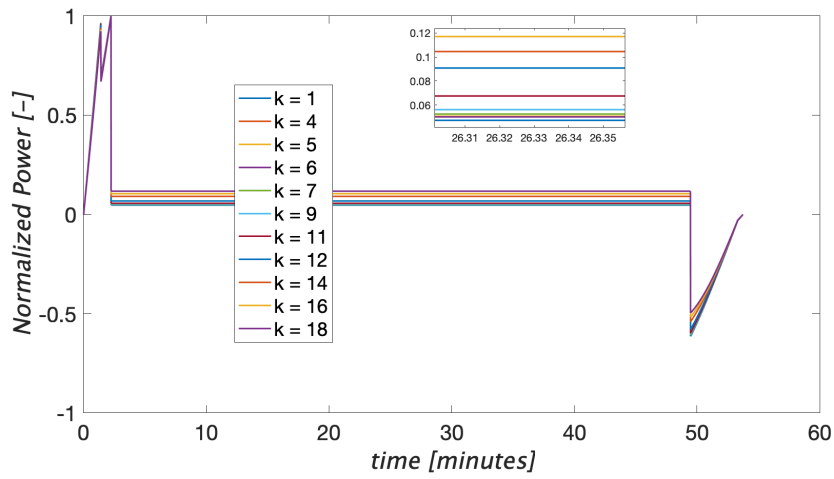


Figure 4.7: Values of the objective function of the problem (4.15) for various values of the scaling factor,  $k$ .

In the constant-speed zone, the proximity of the normalised powers for  $4 \leq k \leq 11$  with the FS one can be clearly seen. Fig. 4.11, shows the speed profiles (always as a function of time) for the same values of the scaling factor, whereas Fig. 4.12 and Fig. 4.13 show the acceleration and the non-normalised power profiles, respectively.

It is interesting to note that, for the selected values of the scaling factor, the RS model's maximum speeds vary between  $33 - 149 \frac{km}{h}$ , whereas the RS model's masses vary between  $3 - 332 kg$ , as shown in Table 4.2. The maximum power provided by the RS BESS models varies between  $3 - 5439 W$ . These values of speeds and BESS powers are certainly easy to handle by a dedicated RS hyperloop mockup.

$k[-]$	$m_{rs}[kg]$
4	331.92
5	169.94
6	98.34
7	61.93
9	29.14
11	15.96
12	12.29
14	7.74
16	5.18
18	3.64

Table 4.2: RS mass values,  $m_{rs}$  function of  $k$ .Figure 4.8: Normalized power profiles as functions of time of both FS and RS hyperloop models for the considered values of the scaling factor  $k$ .



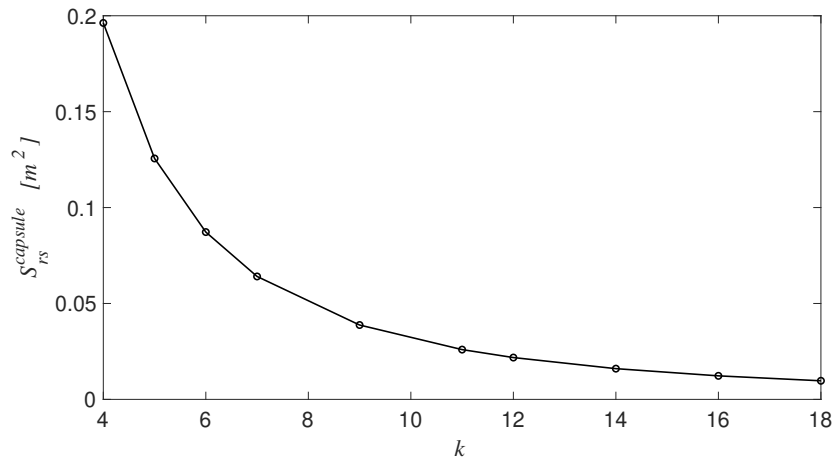


Figure 4.9: The cross sections of the RS model,  $S_{rs}^{capsule}$ , function of the scale factor,  $k$ .

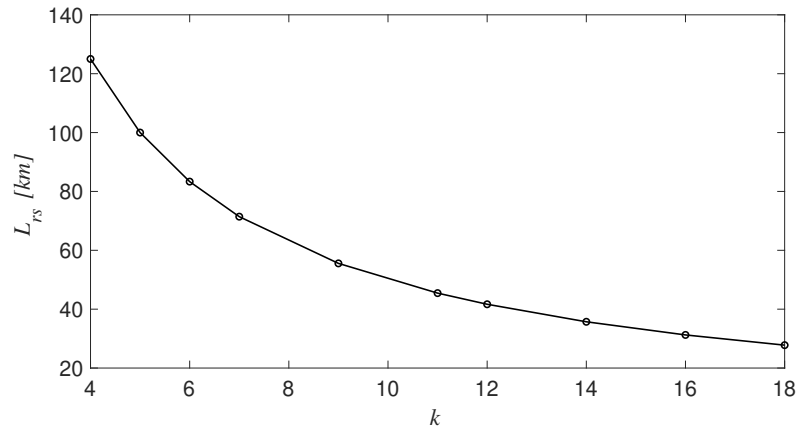


Figure 4.10: The lengths of trajectory,  $L_{rs}$ , function of the scale factor,  $k$ .

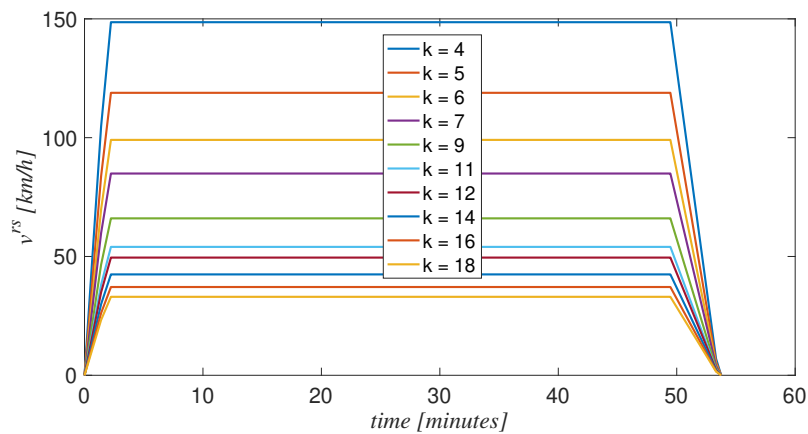


Figure 4.11: Speed profiles as functions of time of the hyperloop RS model for the various considered values of the scaling factor  $k$ .

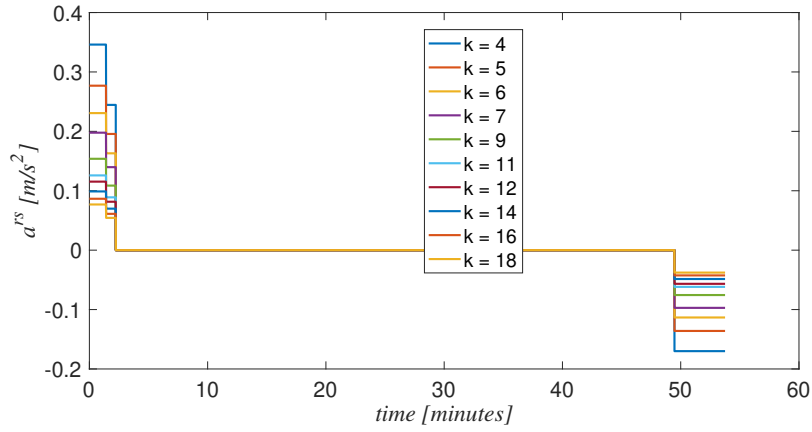


Figure 4.12: Acceleration profiles as functions of time of the hyperloop RS model for the various considered values of the scaling factor  $k$ .

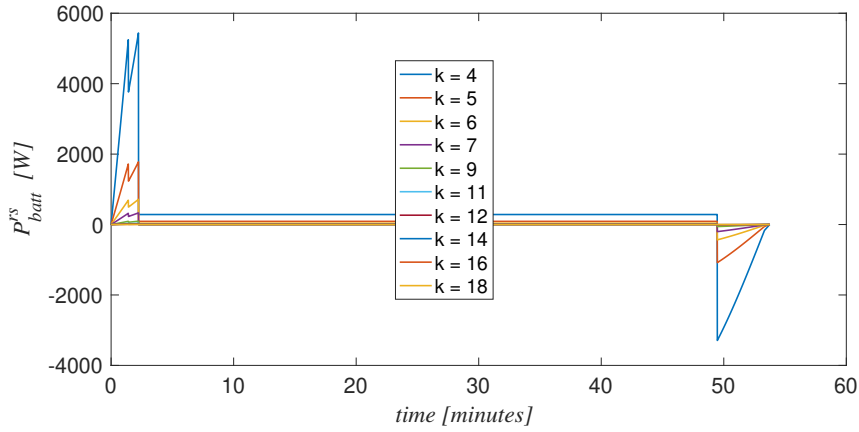


Figure 4.13: Power profiles as functions of time of the hyperloop RS model for the various considered values of the scaling factor  $k$ .

## 4.6 Conclusions

The development of an FS hyperloop prototype system is an expensive and time-consuming process that entails limited flexibility of the realised setup. In this respect, we have proposed a suitable framework that is capable of determining not only the scaling factor but also the main variables and parameters of a hyperloop mockup. More specifically, the proposed framework relies on the operating conditions of the hyperloop infrastructure and the models of the capsule's kinematics, BESS, PS and aerodynamics.

By introducing a suitable metric that takes into account both the energy and power demands of the hyperloop FS and RS capsules, we have shown how the above operating conditions and models can be used to optimally determine the scaling factor of the hyperloop RS model. Furthermore, we have discussed and assessed the importance of the hyperloop capsule's aerodynamics, with respect to the scaling process, and the means of integrating a numerical CFD analysis into the proposed framework.

By making reference to an FS hyperloop system whose characteristics were already determined in a previous study (i.e., capsule's maximum speeds of  $600\text{ km/h}$ , capsule's mass of  $22\text{ tons}$  and maximum BESS power of  $6\text{ MW}$ ), in the proposed framework, we have identified a range of values of the scaling factor, i.e.,  $4 \leq k \leq 11$ . Within such an interval, the objective function of the proposed framework does not exhibit substantial changes and gives an opportunity to the modeler to adopt the value of the scaling factor that is more convenient, as the maximum BESS power of the RS model vary between  $3 - 5439\text{ W}$  with speeds between  $33 - 149\text{ km/h}$ .

Future work will be focused on the construction of an RS hyperloop mockup by using the proposed framework. Such an RS hyperloop model will be used to study the viability of the various technical solutions of the FS hyperloop system in an efficient way, as it simplifies the fast prototyping of various components of the hyperloop capsules and infrastructure.



# 5 A Reduced-Scale Hyperloop Experiment

## 5.1 Introduction

Historically, most of the freight or passengers transportation systems have required complex regulations and standardization frameworks. They rely on creating a set of tests (or evaluations) that have to eventually validate a technology functioning under given constraints in order to maximize an objective represented by safety performance [94] [95]. However, before certifying a technology through standards and regulations, controlled experiments need to take place in order to benchmark the targeted technology. For instance, various countries have developed their own testing infrastructures to investigate the performances of ETs: Japan [96] [97], United States of America [98], Germany [99] or others. For EVs, each car manufacturer creates its own facility to test the vehicles performances. For example, Tesla created in Fremont, USA its testing track [100], while Daimler built its own facility in Immendingen, Germany [101] to test their vehicles in real conditions.

There have been already 2 operational testing facilities specifically developed for hyperloop systems. The first hyperloop testing facility was built by SpaceX in Hawthorne, USA in order to host a student competition [102] [103] [104]. The main objective of the contest was to reach the highest speed at the end of a pre-determined acceleration zone without crashing the hyperloop capsule prototype. This testing facility has the following characteristics.

- Length:  $1\text{ km}$
- Operating pressure:  $100 - 400\text{ mbar}$
- Diameter of the tube:  $\approx 1.8\text{ m}$
- Type of rail: "I" beam
- Material of the rail: aluminium
- Supported capsule's propulsion types: multiple (wheel propulsion, cold gas air, double sided linear induction motor, single sided linear induction motor.)

- Capsule guidance: mechanical (via wheels) or magnetic (via reaction plates)

The second hyperloop testing facility, which has been operational since 2019, was built by Virgin Hyperloop One in Nevada, USA in order to test their own hyperloop capsule [105]. This testing facility has the following characteristics.

- Length:  $300m$
- Operating pressure:  $1 - 10mbar$
- Diameter of the tube:  $\approx 2m$
- Type of rail: 2 reaction plates for levitation and 1 beam for propulsion
- Material of the rail: aluminium
- Propulsion: double sided linear induction motor
- Capsule guidance: mechanical via wheels

The objective of this test was to accelerate a vehicle at medium speeds up to approximately  $200 \frac{km}{h}$ . The presence of a coasting speed zone was not foreseen as the experiment is estimated to last for few seconds. In terms of the kinematics of the capsule, this experiment could eventually be considered similar with the tests that were ran in the SpaceX testing facility due to the short length of trajectory and, therefore, the absence of the coasting speed zone.

Note that none of the aforementioned testing facilities is conceived to carry out experiments addressing the hyperloop technological challenges associated to PS, BESS and thermal management for a relevant set of pressure levels and trajectories with realistic lengths. As shown in Chapters 2, 3, 4, hyperloop capsules maintain a constant high-speed for a relative long distance and, with respect to this specific aspect, a relevant FS or RS hyperloop experiment has not been designed yet. Additionally, as discussed in Chapter 3, the environmental operating conditions of the tube have a large impact of the design of the existing PS of a hyperloop capsule and its energy consumption. To the best of the author's knowledge, none of the existing experiments validated the expected performance of a hyperloop system (i.e., low energy consumption), the PS and its BESS for a large set of pressures and with respect to long trajectories (i.e., more than  $200km$ ).

In view of the above, in this Chapter a RS hyperloop experiment is proposed. It is composed by both an experimental testing infrastructure and an experimental capsule. The RS models can be used for fast prototyping of various components as well as for studying critical phenomena that take place in this peculiar transportation system without the need to develop complex and expensive full-scale setups.

The structure of this Chapter is the following: in Section 5.2, the objectives of the experiment are listed. In Section 5.3, we illustrate the design of the experimental tube and its characteristics, the rail geometry, the sensing, control and telecommunication system, and the depressurization system. In Section 5.4, we present the general characteristics of the experimental capsule, its mechanical components and the characteristics of the propulsion system. In Section 5.5, the design of the experiment is presented and in Section 5.6, we conclude the Chapter with expected future works.

## 5.2 Objectives

There are various advantages related to a hyperloop system: sustainability, energy efficiency, speed, reliability or even safety. With respect to this *Thesis*, as shown in Chapter 2, Chapter 3 and Chapter 4, the focus has been mainly based on the maximization of the energy efficiency.

The main objective of the experiments designed in this chapter is first to validate the energy efficiency of a FS capsule which is linked to given environmental conditions and operations (i.e., Chapter 3). As explained in Chapter 4, this can be obtained by testing the RS capsule that has the same normalized energy consumption of the BESS as its FS counterpart. Therefore, the objective is to validate the mathematical model of the energy needs of the BESS of a RS capsule, thus, the energy needs of a FS capsule. Regarding the RS model scaling factor choice,  $k = 12$ , it represents a reasonable trade-off between the targeted objective function (as shown in Chapter 4) and manufacturing challenges of the RS setup.

To fix ideas, by comparing the theoretical normalized power profile of a BESS RS capsule (i.e., Chapter 4) with the experimental normalized power profile of the BESS RS mockup, we will obtain the necessary results to validate or not the theoretical model of the FS capsule linked for a given set of environmental conditions and operations.

## 5.3 Overview of the Reduced-Scale Hyperloop Infrastructure

The proposed RS infrastructure has a circular shape (see Fig. 5.1) in order to reproduce generic trajectory lengths. The infrastructure is situated at EPFL campus in Lausanne, Switzerland.

### 5.3.1 Tube Geometry and Characteristics

The circular infrastructure has a diameter of approximately  $40m$ . The inner diameter of the circular cross section of the RS infrastructure is  $40cm$  whereas outer cross section diameter is  $41.5cm$ . It is composed by 60 sections, each covering an angle of  $6^\circ$ . Each of the 60 sections is composed by two halves where 5 ribs are integrated in order to accommodate generic rail design (see Fig. 5.2). Each subsection has an outer length of  $2.12m$  with an inner length of  $2.07m$ . The RS infrastructure is mounted on welded steel feet in order to have the axis of the



Figure 5.1: Overview of the EPFL RS hyperloop test infrastructure.

tube at about  $1.4m$  high relative to the tube's foundation.

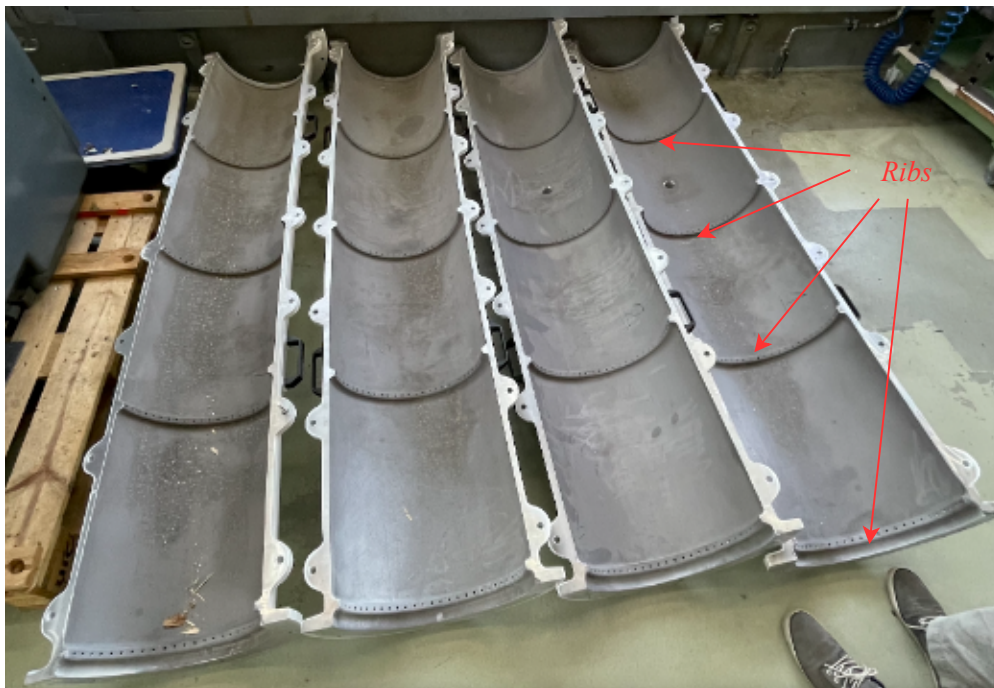


Figure 5.2: Ribs of the tube of the EPFL RS hyperloop test infrastructure

### 5.3.2 Rail Geometry

The geometry of the rail inside the RS infrastructure is shown in Fig. 5.3. It contains two circular rails on the sides in order to mechanically guide the capsule. The material of these circular rails is steel, and they are sustained by a support which is mechanically fixed on the



infrastructure's ribs. In the middle of the two circular steel rails there is a rectangular plate. The material of the rectangular plate is Aluminium and it serves as a reaction plate for the RS PS.



Figure 5.3: The rail design of the EPFL RS hyperloop test infrastructure.

It is worth mentioning that the first capsule prototype that will be tested on the current rail geometry does not present a contactless-stability system, nor a levitation system. A capsule embedding these features is expected to be built in the next iterations of the capsule's design.

### 5.3.3 Sensing, Control and Telecommunication

There are in total four digital pressure sensors and one analog pressure sensor. Two of the digital pressure sensors are located close to the depressurization system and the other two are located on the other two quarters of the RS infrastructure. Each of the 60 sections of the infrastructure contains a laser sensor detecting the presence of the capsule. The purpose of

these sensors is to detect where the capsule is situated along the trajectory.

The pumps are controlled by a groundstation system which is placed nearby the infrastructure. As shown in Chapter 3, the propulsion system is directly linked with the operations of the tube (i.e., with  $p_{tube}$ ). Therefore, in order to test the propulsion system for a large spectrum of pressures, a closed-loop pressure control system is needed. This is implemented in a dedicated control where the generic user can select the operating pressure inside the tube.

In order to ensure a reliable telecommunication between the capsule and the groundstation, a 5G system is used. One antenna is attached to the vehicle and 2 antennas on the RS infrastructure with an  $180^\circ$  positioning.

The entire sensing, control and telecommunication flowchart of the RS infrastructure is shown in Fig. 5.4.

### 5.3.4 Depressurization System

The depressurization system is composed by two pumps which are placed in opposed positions along the tube. In Fig. 5.5 one pump and its connections to the infrastructure are shown.

The model of the pump is called "Busch R5 RD 0360 A". The characteristics of the pump can be found in [106].

A depressurization experiment was carried out during this year targeting 3 different levels of pressure. Initially, a  $100\text{mbar}$  target pressure has been chosen, and approximately, after  $7\text{minutes}$ , the tube reached the desired pressure level. The second experiment reached  $50\text{mbar}$  and the third one reached  $30\text{mbar}$ .

## 5.4 Characteristics of the Capsule Mockup

The characteristics of the RS capsule are defined with the framework presented in Chapter 4. It is worth recalling that the objective of the RS capsule is to have the same normalized power profile as the FS one. It is worth mentioning that, with the actual design of the RS infrastructure, the RS capsule should be characterized by a scaling factor  $k = 12$  and  $L_{fs} = 500\text{km}$ . However, the computation has been done without considering the wheels in the design of the RS capsule because, as mentioned in Chapter 2 and Chapter 3, a FS capsule will eventually not need it. Therefore, additional drag will be added to the RS capsule due to the wheels friction with the rail. This aspect is taken into account when sizing various subsystems (i.e., the BESS).

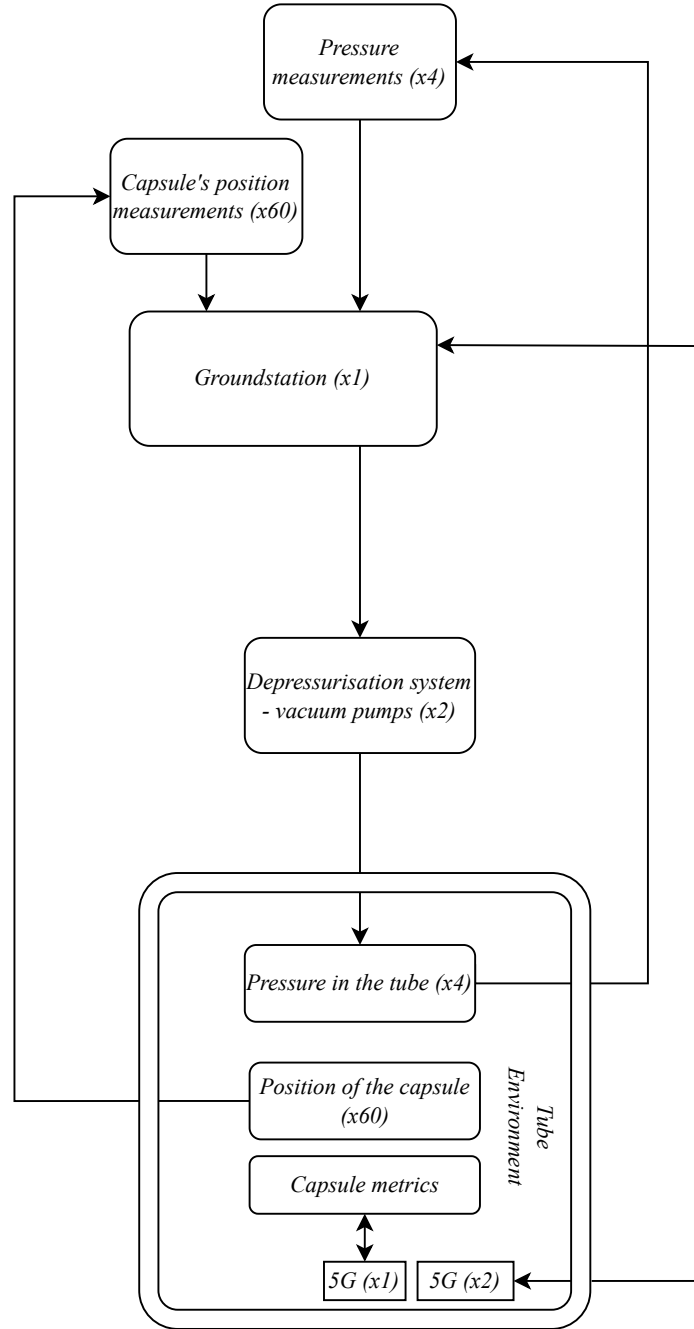


Figure 5.4: Sensing, control and telecommunication flowchart of the RS infrastructure.

#### 5.4.1 General Characteristics of the Capsule

The RS capsule mainly contains a PS and a BESS. For the guidance and stability, a wheels cluster is used. With the actual design, the capsule's pitch and yaw rotations are mechanically constrained. A LIM is actually propelling the capsule using the aluminium reaction plate in the middle of the two circular rails. To fix ideas, a block scheme of the RS capsule PS and its



Figure 5.5: One pump connected to the RS infrastructure.

kinematics is shown in Fig. 5.6. The chassis holds all the mechanical subsystems and it is optimized in order to safely save the weight of the capsule. The aeroshell of the capsule covers all the mechanical subsystems in order to ensure a specific aerodynamic drag. (see Chapter 4)

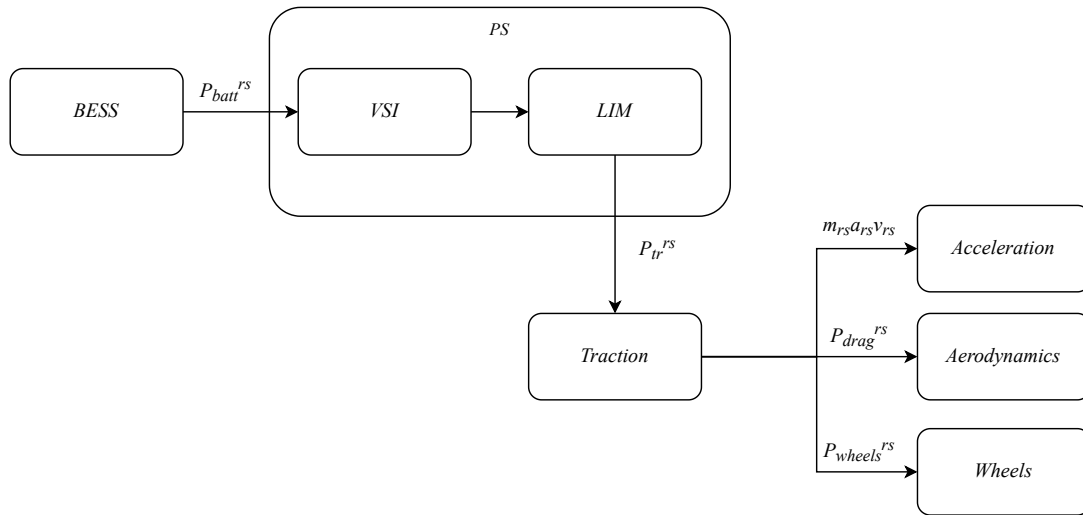


Figure 5.6: The block scheme of the RS capsule PS and its kinematics.

In the center of the capsule, a pressure vessel ensures normal environmental conditions (i.e.,  $p_{env} = p_0$ ), as it is designed to withstand a difference of pressure between the exterior and the interior environments. To fix ideas, the battery cells eventually inflate for an exposure to vacuum of more than few minutes and the electrolytic capacitors of the VSI may experience

the sudden evaporation of the electrolyte with a potential short circuit of the DC links. Inside the pressure vessel, the control system (i.e., a NI sbRIO-9637 and PCBs) is housed along with the VSI (i.e., DC/AC converter), BESS (i.e., battery cells, auxiliary battery, battery case, battery covers, compression tabs, solid state relays, BESS shunt, fuse) and the other electrical subsystems (i.e., temperature sensor, pressure sensor, wires and cables, 5G modem). The dimensions of the various components in the pressure vessel are shown in the Section 5.3.2.

The overview design of the capsule is shown in Fig. 5.7 and in Fig. 5.8. We can observe with in red the aeroshell of the capsule. Inside of the aeroshell, the chassis hosts all the subsystems (i.e., aeroshell, LIM, pressure vessel, capsule wheels) together. The placement of the LIM can be better observed in Fig. 5.8 and in Fig. 5.11.

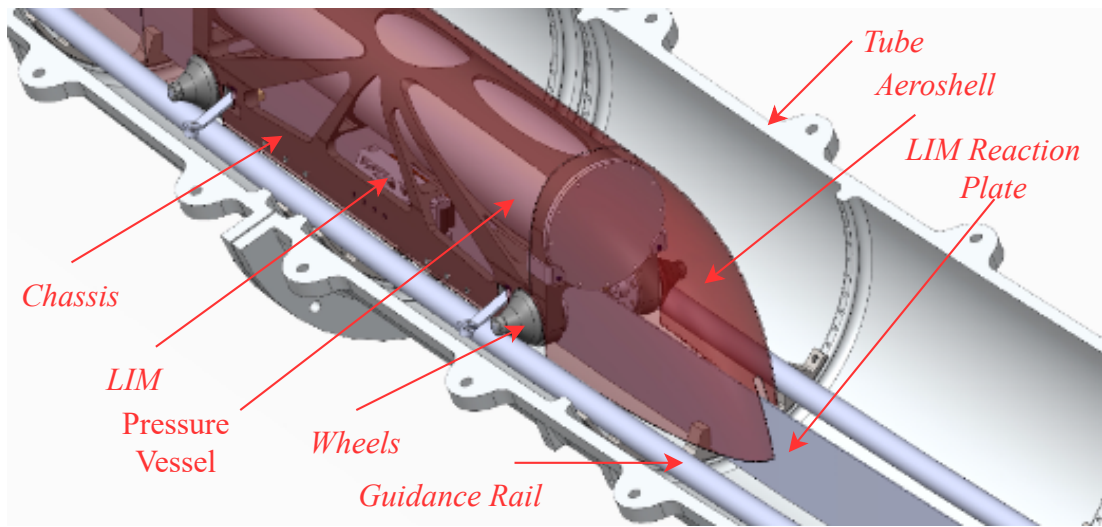


Figure 5.7: The RS capsule design.

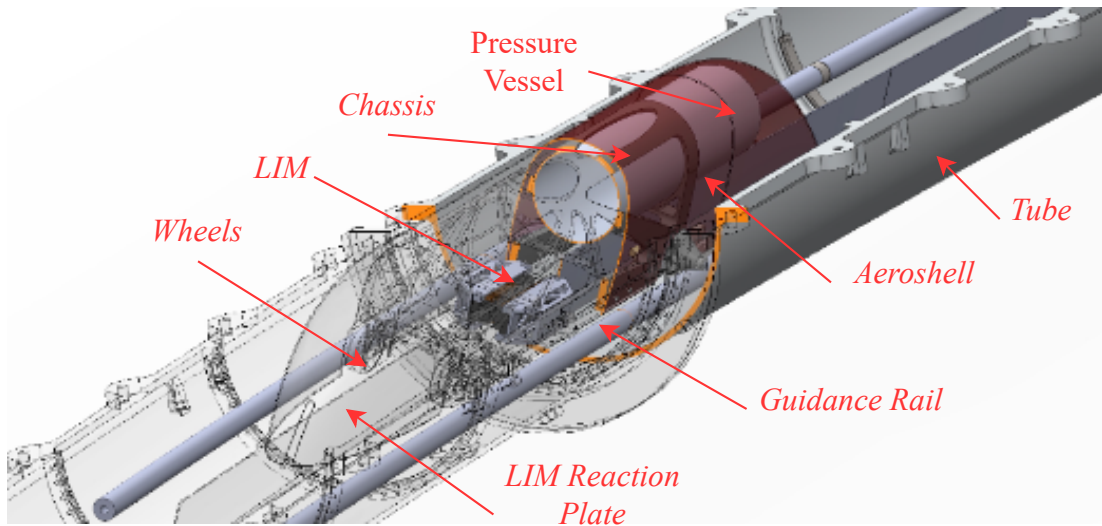


Figure 5.8: The RS capsule design.



As the trajectory of the vehicle is circular, it is worth noting that the capsule travels with an inclination of  $42^\circ$  as shown in Fig. 5.9. The inclination is optimized for the coasting speed zone of  $v_{rs} = 50 \frac{km}{h}$  which corresponds to  $k = 12$ .

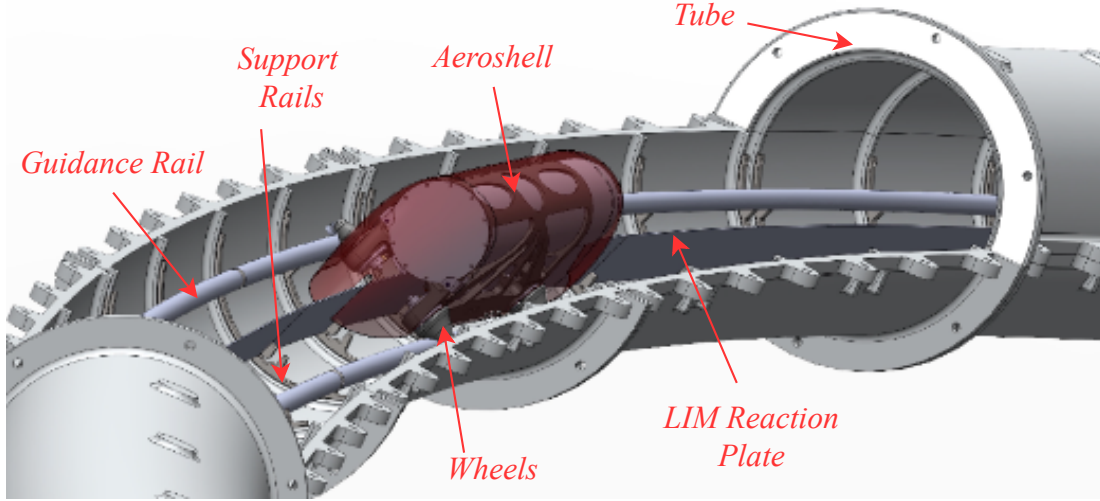


Figure 5.9: The inclination of the RS capsule.

As presented in Chapter 4, for  $k = 12$ , the theoretical mass of the capsule is  $m_{rs} = 12.29kg$ . The experimental mass of the capsule,  $m_{rs}^{exp}$  is calculated as the sum of all the subsystems. Therefore, the expected mass distribution of  $m_{rs}^{exp}$  is shown in Table 5.1.

Component	Mass [kg]
LIM, coils and wires	2.5
DC/AC converter	0.5
BESS (cells, case, aux. battery pack, safety, BMS)	2.6
Electrical subsystems(temperature and pressure sensors, cables, 5G Modem)	1
Control (sbRIO and PCBs)	1
Pressure vessel	2.2
Chassis	1.8
Aeroshell	0.3
Wheels	1

Table 5.1: Mass distribution of  $m_{rs}^{exp}$

The expected total experimental mass of the capsule is  $m_{rs}^{exp} = 12.9kg$ . The error between  $m_{rs}$  and  $m_{rs}^{exp}$  is approximately 5%.

#### 5.4.2 Mechanical Components

The dimensions of the main mechanical subsystems are shown in Table 5.2.

Subsystem	Dimension [mm]
Aeroshell length	1570
Chassis length	700
Chassis width	140
Pressure vessel length	900
Pressure vessel internal diameter	120

Table 5.2: Lengths of the various subsystems of the RS capsule.

The volume of the pressure vessel contains various subsystems presented in Section 5.3.1. The corresponding dimensions of the various subsystems in the pressure vessel are presented in Table 5.3.

Subsystem	Units [-]	Length [mm]	Width [mm]	Height [mm]
Kokam cell	6	140	43	11.6
BESS case	1	186	101	56
BESS total	1	186	101	74
Shunt	1	38	25	12
Contactator	3	57	44.5	31
Auxiliary battery	1	155	55	73
Motherboard	1	153	103	15
sbRIO	1	153	103	37
5G modem	1	105	105	21.5
Temperature sensor	1	66	22	22
Pressure sensor	1	53	22	22
VSI (DC/AC converter)	1	250	95	35

Table 5.3: Dimensions of the various subsystems in the pressure vessel.

The full mechanical fit check of the full assembly is shown in Fig. 5.10.

### 5.4.3 Propulsion System and Battery Energy Storage System

The BESS is built based on 6 cells in series. The cell model is presented in the Chapters 2 and 3. The open circuit voltage of the RS BESS for  $SoC = 100\%$  is  $25.2V$ .

The LIM is situated under the pressure vessel on the sides of the reaction plate. This is shown in Fig. 5.11.

The speed and acceleration profiles that need to be provided by the LIM are shown in Chapter 4 (for  $k = 12$ ). To fix ideas, in order to obtain the acceleration profile in the given time (thus, the speed profile), the required thrust is shown in Fig. 5.12.

It is worth mentioning that the added wheels friction is considered in the thrust profile as well as the aerodynamic drag. The maximum thrust to be provided by the LIM is  $5.75N$  for a

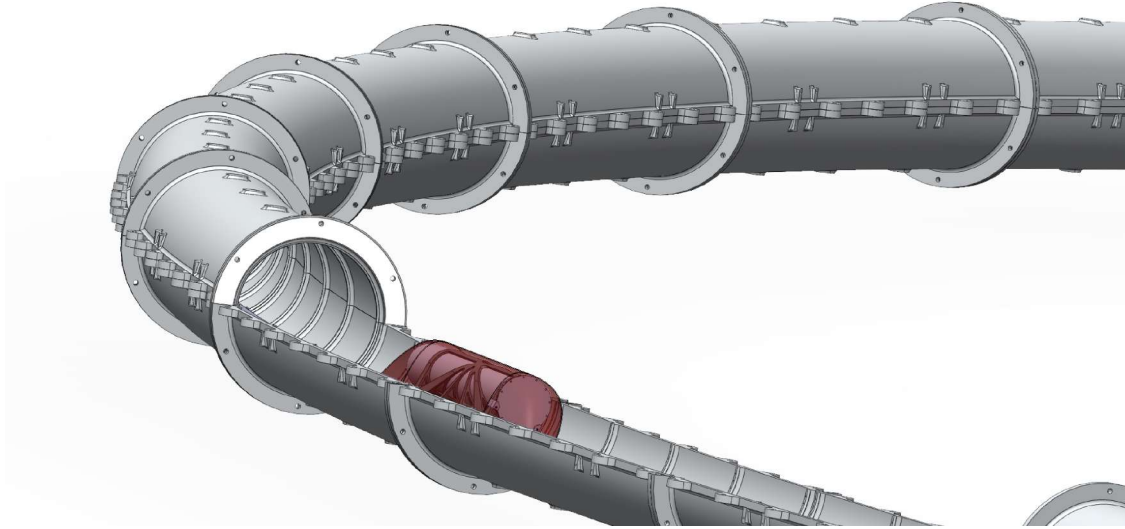


Figure 5.10: The the mechanical fit check overview of the RS infrastructure and RS capsule design.

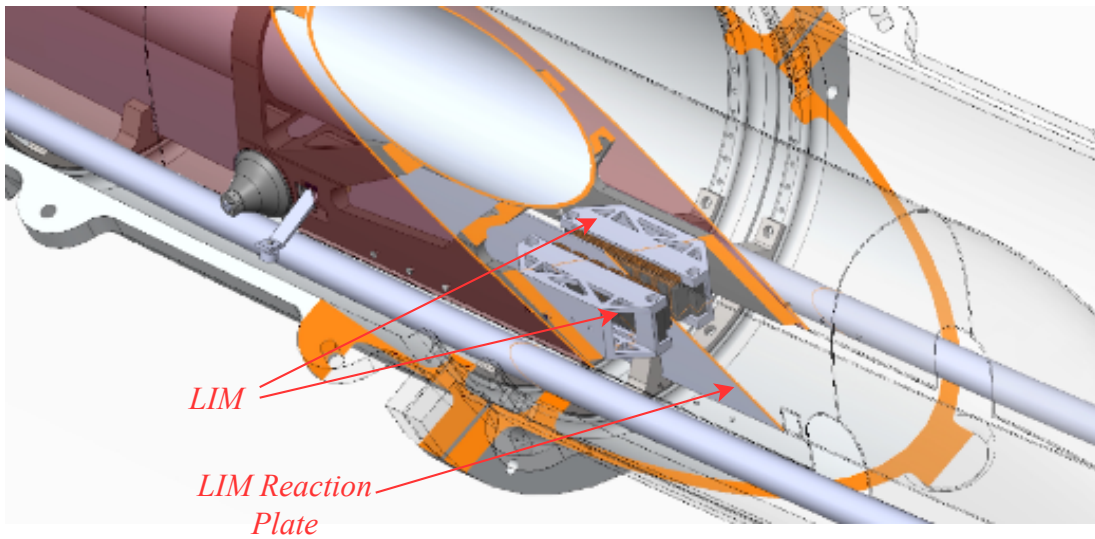


Figure 5.11: LIM position in the RS capsule.

maximum speed of  $v_{rs} = 50 \frac{km}{h}$ . The thrust for the coasting speed zone is  $4.75N$ .



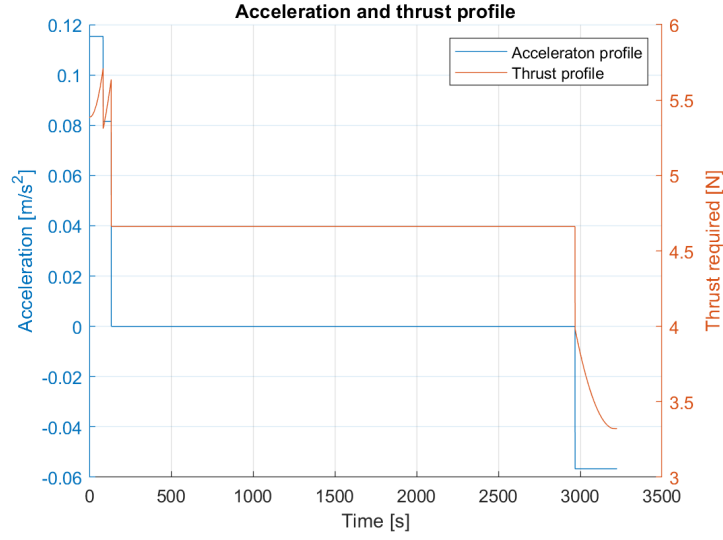


Figure 5.12: Acceleration and thrust profiles of the RS capsule.

## 5.5 First Experiment

As above-mentioned, the objective of this experiment is to benchmark the fundamental results obtained in this Thesis regarding the energy needs of a hyperloop capsule propulsion system. The propulsion system is represented by the VSI and the LIM main characteristics as shown in Fig. 5.6. Therefore, the VSI and the LIM are determined such that they can provide the necessary thrust for a given speed and acceleration profiles, and length of trajectory for the corresponding hyperloop FS model. As a consequence, the optimization of the PS plays a major role to satisfy the energy needs especially concerning its efficiency during the coasting speed zone. Before testing the PS on the RS infrastructure, it will be tested on a rotating test bench in order to characterize its performances [107].

The experiment is planned to take place at the end of 2022-beginning of 2023 and, in this respect, the construction of the infrastructure is close to be completed.

## 5.6 Conclusions

The presented RS infrastructure can serve for various reduced-scale experiments. As an initial step, the first objective of the actual RS infrastructure is to validate the energy needs of a hyperloop energy-autonomous capsule PS with its BESS considering given environmental operating conditions and length of trajectory. This experiment is expected to validate the findings of Chapter 4.

As a future development, the second objective of the proposed RS infrastructure is to serve for improved RS capsule designs that will contain a hybrid levitation, propulsion and stability system. The needs of such a solution are due to the increased magnetic drag of a passive

levitation system and the increased rolling resistance associated to the use of wheels (as shown in Chapters 3 and 5).

To the best of the author's knowledge, this RS infrastructure represents a first attempt to realize a hyperloop experiment that presents a realistic length of trajectory and operating conditions of this new mode of transportation.

## 6 Conclusions

The Thesis has addressed fundamental questions related to the development of the hyperloop system. It has proposed how to approach the design of a hyperloop capsule's BESS and PS in given environmental conditions and with respect to the tube's design and operations, and proposed a method to design a RS hyperloop mockup. Finally, it has also shown an overview at the system level of a RS experiment under construction in the EPFL campus.

Specifically, the Thesis presents an optimization framework to size the PS of energy-autonomous hyperloop capsules by using two different cell models of the BESS. The proposed framework quantitatively evaluates the energy and power requirements of the hyperloop PS in given operational environmental conditions. In addition, a sensitivity and a dominant solution analyses have been pursued. The proposed design method enables to compute energy consumption of the capsules PS between  $10$  to  $60 Wh/km/passenger$  depending on the assumptions, trajectory parameters and cell model. With the proposed architecture and sizing method, the chapter concludes that today's battery and power-electronics technologies present characteristics that are compatible with the hyperloop application, thus enable its development as a viable transportation solution.

Then, an operational-driven optimal-design framework of a hyperloop system is presented. The optimization problem links the operation of a network of hyperloop capsules, the model of the hyperloop infrastructure and its operational conditions, and the model of the capsules PS, BESS, aerodynamics and their kinematics. The proposed framework provided answers to fundamental questions such as: (i) what is the optimal operating pressure inside a hyperloop tube? (ii) What is the achievable global energy consumption of a hyperloop system? (iii) Is there a strong dependency between the infrastructure operation and capsule's PS design? (iv) Which is the impact of a passive magnetic levitation system on the energy consumption of the capsule? (v) Can a front-compressor increase the energy efficiency of a hyperloop system? (vi) How does the Kantrowitz Limit affect the design of a hyperloop system?

The proposed method has quantified the impact of the operational strategy of the hyperloop infrastructure on the energy consumption of the entire system. More specifically, for depres-

surization periods in the range of few days, the energy-per-passenger-per-km can reach high values (especially for long trajectories) with best values in the range of  $100 - 225 \frac{Wh}{passenger \cdot km}$ . Therefore, the first conclusion is to enforce depressurization periods  $\geq 21 days$  as, depending on the length of the trajectory, the energy-per-passenger-per-km can fall in the range between  $20 - 30 \frac{Wh}{passenger \cdot km}$ , thus making this transportation mode energy-competitive with respect to electric trains and intra-continental flights. The proposed framework has also allowed to determine the optimal pressures inside the tube to be in the range from  $2.82 mbar$  to  $76.92 mbar$  for a length of trajectory of  $226 km$ , from  $1.17 mbar$  to  $54.5 mbar$  for a length of trajectory of  $500 km$  and from  $1.14 mbar$  to  $17.25 mbar$  for a length of trajectory of  $1000 km$ . Note that, for the same value of depressurization period, the optimization problem determines larger tube operating pressures for longer trajectories. Furthermore, the proposed optimization has shown that the magnetic levitation drag is responsible of a dramatic increase the capsule's masses, energy needs as well as peak power requirements. Therefore, it is quite clear from these results that hyperloop capsules have to rely on drag-less magnetic levitation solutions especially if the energy reservoir is embedded in the capsule. On the same note, we have shown that carrying an on-board compressor will dramatically increase the power consumption of the BESS. Furthermore, a comparison with the EVs and ETs show that the obtained solutions enable hyperloop to be an energy-efficient and high-speed transportation solution representing a potential alternative for the transportation sector. However, it is important to underline that the values of several key parameters influence the obtained results. Therefore, different sensitivity analyses have been carried out. The most important parameters that influence the results are: capsule's passive mass, number of capsules launched per unit of time, permeability of the tube's material, efficiencies of the propulsion system and aerodynamic drag coefficient of capsules.

The next aspect assessed by the Thesis has been the scaling factor of a hyperloop system. The purpose of this assessment is to design a RS hyperloop experiment in order to validate the findings of Chapters 2 and 3. The objective function of this method is to minimize the difference between the normalized power profiles of the BESSs associated with the RS and FS models of a hyperloop capsule traveling along a pre-defined trajectory and with a pre-determined speed profile. More specifically, the proposed framework relies on the operating conditions of the hyperloop infrastructure and the models of the capsule's BESS, PS, aerodynamics and kinematics. By referencing to a FS hyperloop system determined in Chapter 3, thanks to the proposed process, we have identified a range of optimal values of the scaling factor, i.e.,  $4 \leq k \leq 11$ . Within such an interval, the objective function of the proposed process does not exhibit substantial changes and gives an opportunity to the modeler to adopt the value of the scaling factor that is more convenient, as the maximum BESS power of the RS model vary between  $3 - 5439 W$  with speeds between  $33 - 149 km/h$ . Such a RS hyperloop model can be used to study the viability of the various technical solutions of the FS hyperloop system in an efficient way, as it simplifies the whole process by fast prototyping various hyperloop subsystems.

Finally, based on Chapter 4 results, a circular 40-meters-diameter RS experimental infrastruc-

ture has been illustrated along with an experimental RS capsule. The main objective of the experiment designed in this chapter is to firstly validate the energy efficiency of a FS capsule which is linked to given environmental conditions and operations. This can be obtained by benchmarking the RS capsule presenting the same normalized energy consumption of the BESS as its FS counterpart. We choose the scale factor  $k = 12$  as it represents a reasonable trade-off between the targeted objective function and the manufacturing challenges of the RS setup. As a second objective, the proposed RS infrastructure serves for improved RS capsule designs that will also contain a levitation subsystem, as well as a contactless stability subsystem. This RS infrastructure represents a first attempt to realize a hyperloop experiment that presents a realistic length of trajectory and operating conditions.



## Bibliography

- [1] European Environment Agency, "Greenhouse gas emissions from transport in Europe," Online Report, <https://www.eea.europa.eu/data-and-maps/indicators/transport-emissions-of-greenhouse-gases/transport-emissions-of-greenhouse-gases-12>, December 2019.
- [2] European Environment Agency, "Transport White paper 2011," Online Report, <https://www.eea.europa.eu/policy-documents/transport-white-paper-2011>, 2011.
- [3] J. Becker, T. Nemeth, R. Wegmann and D. U. Sauer, "Dimensioning and Optimization of Hybrid Li-Ion Battery Systems for EVs," in *World Electric Vehicle Journal* June 2018.
- [4] B. Bilgin et al., "Making the Case for Electrified Transportation," in *IEEE Transactions on Transportation Electrification*, vol. 1, no. 1, pp. 4-17, June 2015.
- [5] Y.F. Wang, K.P. Li, X.M. Xu, Y.R. Zhang, "Transport energy consumption and saving in China," in *Renewable and Sustainable Energy Reviews* 29 (2014) 641–655.
- [6] K. Ruangjirakit, Y. Laoonual, A. Charadsuksawat, V. Kiattikomol and S. Sridan, "A Study of Grid-to-Wheel Energy Consumption of Electric Vehicle on Real Road Tests in Bangkok," 2018 IEEE Transportation Electrification Conference and Expo, Asia-Pacific (ITEC Asia-Pacific), Bangkok, 2018, pp. 1-5.
- [7] The International Council on Clean Transportation, "Effects of battery manufacturing on electric vehicle life-cycle greenhouse gas emissions," Technical Report, [online] [www.theicct.org](http://www.theicct.org), February 2018.
- [8] E. Andersson, P. Lukaszewicz, "Energy consumption and related air pollution for Scandinavian electric passenger trains," Technical Report, [online] [https://www.kth.se/polopoly\\_fs/1.179879.1397142793!/Menu/general/column-content/attachment/Energy\\_060925\\_full\\_pdf.pdf](https://www.kth.se/polopoly_fs/1.179879.1397142793!/Menu/general/column-content/attachment/Energy_060925_full_pdf.pdf), 2006.
- [9] International Union of Railways, "Technologies and Potential Developments for Energy Efficiency and CO<sub>2</sub> Reductions in Rail Systems," Technical Report, [online] [https://uic.org/IMG/pdf/\\_27\\_technologies\\_and\\_potential\\_developments\\_for\\_energy\\_efficiency\\_and\\_co2\\_reductions\\_in\\_rail\\_systems\\_uic\\_in\\_colaboration.pdf](https://uic.org/IMG/pdf/_27_technologies_and_potential_developments_for_energy_efficiency_and_co2_reductions_in_rail_systems_uic_in_colaboration.pdf), December 2016.

- [10] SpaceX, "Hyperloop Alpha," Technical Report, [online] [https://www.spacex.com/sites/spacex/files/hyperloop\\_alpha-20130812.pdf](https://www.spacex.com/sites/spacex/files/hyperloop_alpha-20130812.pdf), August 2013.
- [11] SpaceX, "SpaceX Hyperloop Pod Competition Rules," January 2016.
- [12] V. Madonna, P. Giangrande and M. Galea, "Electrical Power Generation in Aircraft: Review, Challenges, and Opportunities," in *IEEE Transactions on Transportation Electrification*, vol. 4, no. 3, pp. 646-659, Sept. 2018.
- [13] F. Akar, Y. Tavlasoglu and B. Vural, "An Energy Management Strategy for a Concept Battery/Ultracapacitor Electric Vehicle With Improved Battery Life," in *IEEE Transactions on Transportation Electrification*, vol. 3, no. 1, pp. 191-200, March 2017.
- [14] B. Sarlioglu and C. T. Morris, "More Electric Aircraft: Review, Challenges, and Opportunities for Commercial Transport Aircraft," in *IEEE Transactions on Transportation Electrification*, vol. 1, no. 1, pp. 54-64, June 2015.
- [15] R. C. Kroeze and P. T. Krein, "Electrical battery model for use in dynamic electric vehicle simulations," 2008 IEEE Power Electronics Specialists Conference, Rhodes, 2008, pp. 1336-1342.
- [16] K. Wipke, T. Markel and D. Nelson, "Optimizing Energy Management Strategy and Degree of Hybridization for a Hydrogen Fuel Cell SUV," in *Proceedings of 18th Electric Vehicle Symposium*, Berlin, 2001.
- [17] K. Dominik, H. Chris and R. Aymeric, 2008, "Impact of Component Size on Plug-In Hybrid Vehicle Energy Consumption Using Global Optimization", *The World Electric Vehicle Journal*, vol.2, no.2.
- [18] A. González-Gil, R. Palacin, P. Batty, J.P. Powell, "A systems approach to reduce urban rail energy consumption," in *Energy Conversion and Management* 80 (2014) 509–524.
- [19] D. Zhao, R. Stobart, G. Dong and E. Winward, "Real-Time Energy Management for Diesel Heavy Duty Hybrid Electric Vehicles," in *IEEE Transactions on Control Systems Technology*, vol. 23, no. 3, pp. 829-841, May 2015.
- [20] Huilong Yu, F. Castelli-Dezza and F. Cheli, "Optimal powertrain design and control of a 2-IWD electric race car," 2017 International Conference of Electrical and Electronic Technologies for Automotive, Torino, 2017, pp. 1-7.
- [21] A. González-Gil, R. Palacin, P. Batty, "Optimal energy management of urban rail systems: Key performance indicators," in *Energy Conversion and Management* 90 (2015) 282–291.
- [22] Y. Cao, R. C. Kroeze and P. T. Krein, "Multi-timescale Parametric Electrical Battery Model for Use in Dynamic Electric Vehicle Simulations," in *IEEE Transactions on Transportation Electrification*, vol. 2, no. 4, pp. 432-442, Dec. 2016.



- [23] J. Park, Y. L. Murphey and M. Abul Masrur, "Intelligent Energy Management and Optimization in a Hybridized All-Terrain Vehicle With Simple On–Off Control of the Internal Combustion Engine," in *IEEE Transactions on Vehicular Technology*, vol. 65, no. 6, pp. 4584-4596, June 2016.
- [24] B. Y. Liawa, G. Nagasubramanianb, R. G. Jungstc, D. H. Doughtyb, "Modeling of lithium ion cells—A simple equivalent-circuit model approach," in *Solid State Ionics* 175 (2004) 835–839.
- [25] G. Joos, M. de Freige and M. Dubois, "Design and simulation of a fast charging station for PHEV/EV batteries," 2010 IEEE Electrical Power and Energy Conference, Halifax, NS, 2010, pp. 1-5.
- [26] S. Santhanagopalan, Q. Guo, P. Ramadass, and R. E. White. "Review of models for predicting the cycling performance of lithiumion batteries," in *Journal of Power Sources*, 156(2):620–628, 2006.
- [27] M. R. Jongerden and B. R. Haverkort. "Which battery model to use?," in *IET software*, 3(6):445–457, 2009.
- [28] M. Einhorn, F. V. Conte, C. Kral and J. Fleig, "Comparison, Selection, and Parameterization of Electrical Battery Models for Automotive Applications," in *IEEE Transactions on Power Electronics*, vol. 28, no. 3, pp. 1429-1437, March 2013.
- [29] D. W. Dees, V. S. Battaglia and A. Bélanger, "Electrochemical modeling of lithium polymer batteries," in *Journal of Power Sources* 110 (2002) 310–320.
- [30] C. Zhao, H. Yin, Z. Yang and C. Ma, "Equivalent Series Resistance-Based Energy Loss Analysis of a Battery Semiactive Hybrid Energy Storage System," in *IEEE Transactions on Energy Conversion*, vol. 30, no. 3, pp. 1081-1091, Sept. 2015.
- [31] E. E. Dudnikov, "Advantages of a new Hyperloop transport technology," 2017 Tenth International Conference Management of Large-Scale System Development (MLSD), Moscow, 2017, pp. 1-4.
- [32] W. Ji, G. Jeong, C. Park, I. Jo and H. Lee, "A Study of Non-Symmetric Double-Sided Linear Induction Motor for Hyperloop All-In-One System (Propulsion, Levitation, and Guidance)," in *IEEE Transactions on Magnetics*, vol. 54, no. 11, pp. 1-4, Nov. 2018, Art no. 8207304.
- [33] H. Cho, Y. Liu and K. A. Kim, "Short-Primary Linear Induction Motor Modeling with End Effects for Electric Transportation Systems," 2018 International Symposium on Computer, Consumer and Control (IS3C), Taichung, Taiwan, 2018, pp. 338-341.
- [34] A. E. Hodaib, S. F. A. Fattah, "Conceptional Design of a Hyperloop Capsule with Linear Induction Propulsion System," *World Academy of Science, Engineering and Technology International Journal of Aerospace and Mechanical Engineering* Vol:10, No:5, 2016.

- [35] T. Nemeth, A. Bubert, J. N. Becker, R. W. De Doncker and D. U. Sauer, "A Simulation Platform for Optimization of Electric Vehicles With Modular Drivetrain Topologies," in *IEEE Transactions on Transportation Electrification*, vol. 4, no. 4, pp. 888-900, Dec. 2018.
- [36] Liversage, P., and Trancossi, M., "Analysis of triangular sharkskin profiles according to second law," *Modelling, Measurement and Control B*. 87(3), 188-196, September 2018.
- [37] İ. Şengör, H. C. Kılıçkiran, H. Akdemir, B. Kekezogcaronlu, O. Erdinç and J. P. S. Catalão, "Energy Management of a Smart Railway Station Considering Regenerative Braking and Stochastic Behaviour of ESS and PV Generation," in *IEEE Transactions on Sustainable Energy*, vol. 9, no. 3, pp. 1041-1050, July 2018.
- [38] S. Heydari, P. Fajri, M. Rasheduzzaman and R. Sabzehgar, "Maximizing Regenerative Braking Energy Recovery of Electric Vehicles Through Dynamic Low-Speed Cutoff Point Detection," in *IEEE Transactions on Transportation Electrification*, vol. 5, no. 1, pp. 262-270, March 2019.
- [39] Byrd, R. H., J. C. Gilbert, and J. Nocedal. "A Trust Region Method Based on Interior Point Techniques for Nonlinear Programming." *Mathematical Programming*, Vol 89, No. 1, 2000, pp. 149–185.
- [40] Byrd, R. H., Mary E. Hribar, and Jorge Nocedal. "An Interior Point Algorithm for Large-Scale Nonlinear Programming." *SIAM Journal on Optimization*, Vol 9, No. 4, 1999, pp. 877–900.
- [41] YALMIP : A Toolbox for Modeling and Optimization in MATLAB, Löfberg, J., In *Proceedings of the CACSD Conference*, Taipei, Taiwan, 2004.
- [42] Bombardier CRJ-1000 Aircraft, "CRJ Series," Technical Report, [online] [https://commercialaircraft.bombardier.com/themes/bca/pdf/Bombardier\\_CRJ\\_Series\\_Brochure.pdf](https://commercialaircraft.bombardier.com/themes/bca/pdf/Bombardier_CRJ_Series_Brochure.pdf), 2017.
- [43] Max M. J. Opgenoord and Philip C. Caplan, "Design of the Hyperloop Concept," *AIAA Journal* 2018 56:11, 4261-4270.
- [44] "IEC 60850:2014 International Electrotechnical Commission–Railway applications - Supply voltages of traction systems," November 2014.
- [45] J. Sears, D. Roberts and K. Glitman, "A comparison of electric vehicle Level 1 and Level 2 charging efficiency," 2014 IEEE Conference on Technologies for Sustainability (SusTech), Portland, OR, 2014, pp. 255-258.
- [46] K. Knezović, S. Martinenas, P. B. Andersen, A. Zecchino and M. Marinelli, "Enhancing the Role of Electric Vehicles in the Power Grid: Field Validation of Multiple Ancillary Services," in *IEEE Transactions on Transportation Electrification*, vol. 3, no. 1, pp. 201-209, March 2017.

- [47] R. Xie, W. Wei, M. E. Khodayar, J. Wang and S. Mei, "Planning Fully Renewable Powered Charging Stations on Highways: A Data-Driven Robust Optimization Approach," in *IEEE Transactions on Transportation Electrification*, vol. 4, no. 3, pp. 817-830, Sept. 2018.
- [48] A. Rufer, "Energy Storage Systems and Components", Northwestern U.S.A.: CRC Press, Taylor and Francis Group, 2018, pp. 68-70.
- [49] G. Bohn and G. Steinmetz, "The electromagnetic levitation and guidance technology of the 'transrapid' test facility Emsland," in *IEEE Transactions on Magnetics*, vol. 20, no. 5, pp. 1666-1671, September 1984.
- [50] B. Sands, "The German Magnetic Levitation Train (Transrapid," in *Built Environment (1978-), 1993, Vol. 19, No. 3/4, The Age of the Train (1993)*, pp. 244-256.
- [51] A. Cassat and M. Jufer, "MAGLEV projects technology aspects and choices," in *IEEE Transactions on Applied Superconductivity*, vol. 12, no. 1, pp. 915-925, March 2002.
- [52] R. Hellinger and P. Mních, "Linear Motor-Powered Transportation: History, Present Status, and Future Outlook," in *Proceedings of the IEEE*, vol. 97, no. 11, pp. 1892-1900, Nov. 2009.
- [53] L. Miller and M. Wackers, "Transrapid maglev system technical readiness and corridors of application," in *Journal of Advanced Transportation*, vol. 27, no. 1, pp. 49-64., January 2010.
- [54] D. Patil, M. K. McDonough, J. M. Miller, B. Fahimi and P. T. Balsara, "Wireless Power Transfer for Vehicular Applications: Overview and Challenges," in *IEEE Transactions on Transportation Electrification*, vol. 4, no. 1, pp. 3-37, March 2018.
- [55] B. J. Limb et al., "Economic Viability and Environmental Impact of In-Motion Wireless Power Transfer," in *IEEE Transactions on Transportation Electrification*, vol. 5, no. 1, pp. 135-146, March 2019.
- [56] M. Ceraolo, "Modeling and Simulation of AC Railway Electric Supply Lines Including Ground Return," in *IEEE Transactions on Transportation Electrification*, vol. 4, no. 1, pp. 202-210, March 2018.
- [57] Y. He et al., "Multiobjective Co-Optimization of Cooperative Adaptive Cruise Control and Energy Management Strategy for PHEVs," in *IEEE Transactions on Transportation Electrification*, vol. 6, no. 1, pp. 346-355, March 2020.
- [58] C. Wu, S. Lu, F. Xue, L. Jiang and M. Chen, "Optimal Sizing of Onboard Energy Storage Devices for Electrified Railway Systems," in *IEEE Transactions on Transportation Electrification*, vol. 6, no. 3, pp. 1301-1311, Sept. 2020.
- [59] Feser J.P., Prasad A.K., Advani S.G., "Experimental characterization of in-plane permeability of gas diffusion layers," in *Journal of Power Sources* 162, pp. 1226-1231, 2006.

- [60] Hou, Yi. (2012). Experimental characterization and modeling of the permeability of fibrous preforms using gas for direct processes application, [Article].
- [61] Paulini, Peter, A LABORATORY AND ON-SITE TEST METHOD FOR AIR PERMEABILITY OF CONCRETE, Conference Paper: 2nd International Symposium on Service Life Design for Infrastructure, 4-6 October 2010, Delft, The Netherlands.
- [62] H. Heller, D. Hall, "Design and Production of Concrete Tubes for Vacuum Transportation Infrastructure," Technical Report, December 2018.
- [63] J. Oh, T. Kang, S. Ham, K. S. Lee, Y. J. Jang, H. S. Ryou and J. Ryu, "Numerical Analysis of Aerodynamic Characteristics of Hyperloop System," in *Energies* 12(3):518, February 2019.
- [64] Virgin Hyperloop One, "Capsule Technical Specification", Technical Report [online] <https://virginhyperloop.com/>.
- [65] Transpod, "Reduced Scale Facility," Technical Report, [online] <https://www.transpod.com/test-facility/>, October 2018.
- [66] Wu, W. Tunnelling and tunnel mechanics—a rational approach to tunnelling by Dimitrios Kolymbas. *Acta Geotech.* 1, 75–76 (2006).
- [67] P. Huovinen, "Air-Permeability of Concrete," *Nordic Concrete Research* 1, 1-17, December 1982.
- [68] Girrens SP, Farrar CR. Air Permeability in a Seismically Loaded Shear Wall. *Earthquake Spectra.* 1992;8(4):555-572.
- [69] Olufemi, F.S., "Effect of Supplementary Cementitious Materials on the Air-Permeability of Concrete," Research Paper, *JOURNAL OF MATERIALS AND ENGINEERING STRUCTURES* 4, (2017), 51–61.
- [70] Busch Vacuum Solutions, "Cobra NC 2500 B," Technical Report, [online] <https://www.buschvacuum.com/global/en/products/cobra-industry/cobra-nc/cobra-nc-2500-b>.
- [71] Transpod, "The Pod," Technical Report, [online] <https://www.transpod.com/the-pod/>, 2020.
- [72] "EN 50163: Railway applications—Supply voltages of traction systems," February 2013.
- [73] C. Grover, I. Knight, F. Okoro, I. Simmons, G. Couper, P. Massie, B. Smith, "Automated Emergency Brake Systems: Technical requirements, costs and benefits, Prepared for the European Commission standards, DG Enterprise," Technical Report, [online] [https://circabc.europa.eu/sd/a/3ab87fdc-5715-4733-af50-c3608034ca56/report\\_aebs\\_en.pdf](https://circabc.europa.eu/sd/a/3ab87fdc-5715-4733-af50-c3608034ca56/report_aebs_en.pdf), April, 2008.
- [74] Flankl, Michael; Wellerdieck, Tobias; Tüysüz, Arda; Kolar, Johann Walter: 'Scaling laws for electrodynamic suspension in high-speed transportation', *IET Electric Power Applications*, 2018, 12, (3), p. 357-364.

- [75] Fritz E., Blow L., Kluhspies J., Kircher R., Witt M.H. Energy consumption of track-based high-speed trains: maglev systems in comparison with wheel-rail systems // *Transportation Systems and Technology*. - 2018. - Vol. 4. - N. 3 suppl. 1. - P. 134-155.
- [76] International Electrotechnical Commission IEC (2019) "International Standard IEC 60193: Hydraulic turbines, storage pumps and pump-turbines - model acceptance tests", Edition 3.0, 2019-04.
- [77] W. Yossri, S. Ben Ayed and A. Abdelkefi, "Three-dimensional computational fluid dynamics investigation on size effect of small-scale wind turbine blades", *AIAA Scitech 2021 Forum*, 11–15 and 19–21 January 2021.
- [78] T. Revaz, M. Lin and F. Porté-Agel, "Numerical Framework for Aerodynamic Characterization of Wind Turbine Airfoils: Application to Miniature Wind Turbine WiRE-01", *Energies* 2020, 13, 5612.
- [79] M. Bastankhah and F. Porté-Agel, "A New Miniature Wind Turbine for Wind Tunnel Experiments. Part I: Design and Performance", *Energies* 2017, 10, 908.
- [80] M.-C. Gauffre, H. Neau, O. Simonin, R. Ansart, N. Meyers and S. Petitot, "Numerical Simulation of Dome Filling in an Experimental Rocket Engine Mockup", *Journal of Propulsion and Power*, Vol. 30, No. 3, May–June 2014.
- [81] V. Zubanov, V. Egorychev, L. Shabliy, "Design of Rocket Engine for Spacecraft Using CFD-Modeling", *Procedia Engineering*, Volume 104, 2015, Pages 29-35.
- [82] H. Nagata, T. Uematsu, K. Ito, "CAMUI Type Hybrid Rocket as Small Scale Ballistic Flight Testbed", *Transactions of the Japan Society for Aeronautical and Space Sciences, Aerospace Technology Japan*, 2012, Volume 10, March 2012.
- [83] A. Casaburo, G. Petrone, F. Franco, and S. De Rosa, "A Review of Similitude Methods for Structural Engineering", *ASME. Appl. Mech. Rev.* May 2019; 71(3): 030802.
- [84] Lee, J.; You, W.; Lim, J.; Lee, K.-S.; Lim, J.-Y. "Development of the Reduced-Scale Vehicle Model for the Dynamic Characteristic Analysis of the Hyperloop", *Energies* 2021, 14, 3883.
- [85] Yang Sui, Jiqiang Niu, Qiuju Yu, Yanping Yuan, Xiaoling Cao, Xiaofeng Yang, "Numerical analysis of the aerothermodynamic behavior of a Hyperloop in choked flow", *Energy*, Volume 237, 2021, 121427, ISSN 0360-5442.
- [86] T. Morizane, K. Tsujikawa, and N. Kimura, "Control of Traction and Levitation of Linear Induction Motor Driven by Power Source With Frequency Component Synchronous With the Motor Speed," *IEEE Transactions on Magnetics*, vol. 47, no. 10, pp. 4302–4305, Oct. 2011, Conference Name: IEEE Transactions on Magnetics.
- [87] S. Nakatani, D. Okamori, T. Morizane, and H. Omori, "Dynamic Characteristics Verification of Linear Induction Motor by Simultaneous Propulsion and Levitation Control," in

- 2020 22nd European Conference on Power Electronics and Applications (EPE'20 ECCE Europe), Sep. 2020, P1–P10.
- [88] S. Nakatani, K. Sannomiya, D. Okamori, T. Morizane, N. Kimura, and H. Omori, "Experimental Confirmation of Speed and Air Gap Control with Only Linear Induction Motor for Levitation," in 2019 12th International Symposium on Linear Drives for Industry Applications (LDIA), Jul. 2019, pp. 1–5.
- [89] S. Nakatani, D. Okamori, and T. Morizane, "Verification of Control Performance when Driving Linear Induction Motor with Superimposed Frequency," in 2020 International Conference on Electrical Machines (ICEM), ISSN: 2381-4802, vol. 1, Aug. 2020, pp. 1246–1250.
- [90] Joseph R. Chambers, "The Role of Dynamically Scaled Free-Flight Models in Support of NASA's Aerospace Programs," NASA SP 2009-575.
- [91] Gang Wang, Minghui Zhang, Yujin Tao, Jie Li, Dong Li, Yizhe Zhang, Changsheng Yuan, Weimin Sang, Binqian Zhang, "Research on analytical scaling method and scale effects for subscale flight test of blended wing body civil aircraft," *Aerospace Science and Technology*, Volume 106, 2020, 106114, ISSN 1270-9638.
- [92] Gary Weaks, "Weight and flight performance of scale models," Technical Report [online], <https://bit.ly/37akCyi>.
- [93] Tony Govoni, Malicia Leipold, "Aerodynamic and CFD of an hyperloop reduced scale model", Master Thesis EPFL, June 2021.
- [94] EASA,. (2011). Presentation of EASA Research Activities.
- [95] Fischer, C.. (2007). The European Railway Agency (ERA). 58. 59-65.
- [96] Kanoshima, Emiko. (2002). Development of the Tokaido Shinkansen Railway-Axles in 1950s-1960s and Risk Management. *Journal of the Japan Institute of Metals*. 66. 1236-1245.
- [97] Nishijima, Shigehiro and Eckroad, Steven and Marian, Adela and Choi, Kyeongdal and Kim, Woo and Terai, Motoaki and Deng, Zigang and Zheng, Jun and Jiasu, Wang and Umemoto, Katsuya and Du, Jia and Febvre, Pascal and Keenan, Shane and Mukhanov, Oleg and Cooley, Lance and Foley, Catherine and Hassenzahl, William and Izumi, Mitsuru. (2013). Superconductivity and the environment: A Roadmap. *Superconductor Science and Technology*. 26. 113001.
- [98] Quanan, Huang and Jian, Song and Lei, Li. (2011). Research on Rapid Testing Platform for TCU of Automated Manual Transmission. *Measuring Technology and Mechatronics Automation, International Conference on*. 3. 67-70.
- [99] Jimenez-Redondo, Noemi and Escriba, Sergio and Benitez, Francisco and Cores, F and Caceres, Noelia. (2014). Towards automated and cost-efficient track maintenance. Final developments of the ACEM-Rail project.

- [100] Aslan, Yigit. (2021). Analysis of Tesla Inc. Entering German Market from the United States.
- [101] Schoener, Hans-Peter and Imdahl, Reiner. (2018). Daimler's New Proving Ground in Immendingen: Designed for Testing Autonomous Vehicles.
- [102] Seydoux, Martin and Riva, Nicolò and Rametti, Simone and Benedetti, Lorenzo and Dimier, Theophane and Bollier, Nicolas and Hodder, André. (2019). Design and manufacturing of a Linear Induction Motor for the 2019 EPFLoop prototype in the framework of the SpaceX Hyperloop competition.
- [103] Opgenoord, Max and Merian, Chris and Mayo, John and Kirschen, Philippe and O'Rourke, Colm and Izatt, Gregory and Monahan, Greg and Paxson, Derek and Wheeler, Charlie and Zhang, Shawn and Zhang, Chuan and Sakhibova, Nargis and Vancea, Georgiana and Aggarwal, Raghav and Ball, Sabrina and Caplan, Philip and Chamberlain, Peter and Chen, Josh and Chen, Stephanie and Vaish, Sarthak. (2017). MIT Hyperloop Final Report.
- [104] Nikolaev, Ruslan and Idiatullin, Rinat and Nikolaeva, Dinara. (2018). Software system in Hyperloop pod. *Procedia Computer Science*. 126. 878-890.
- [105] Armağan, Kemal. (2020). The fifth mode of transportation: Hyperloop.
- [106] Busch Vacuum Solutions, "R5 RD 0360 A," Technical Report, [online] <https://bit.ly/3KM0qpW>.
- [107] Jérémie Arthur Maurice Pochon, "Design and build of a test bench for the characterisation of a Linear Induction Motor (LIM) applied to a hyperloop propulsion system," Master Thesis at DESL-EPFL on Energy Sciences and Technologies, June 2022.





# Denis Tudor

☎ +41 77 975 73 32 | 🏠 1994 | ✉ denis.tudor@epfl.ch | 🌐 <https://people.epfl.ch/denis.tudor> | 📍 Lausanne, Switzerland

## Education

### Swiss Federal Institute of Technology Lausanne

Lausanne, Switzerland

PhD in EE, Title: Optimal Design Strategies of a Hyperloop System, Supervisor: Prof. Mario Paolone

Mar. 2018 - present

### Politehnica University of Bucharest

Bucharest, Romania

BS in Electronics and Telecommunication, Valedictorian, GPA: 9.78/10, Engineering Grade: 10/10, Supervisor: Prof.

Mar. 2013 - Jun. 2017

Mircea Bodea

## Publications

- [1] **Denis Tudor**, Mario Paolone, "Optimal Design of the Propulsion System of a Hyperloop Capsule," in *IEEE Transactions on Transportation Electrification*, vol. 5, no. 4, pp. 1406-1418, Dec. 2019.
- [2] **Denis Tudor**, Mario Paolone, "Influence of Battery Models on the Optimal Design of the Propulsion System of a Hyperloop Capsule," in *2019 IEEE Vehicle Power and Propulsion Conference (VPPC)*, 2019, pp. 1-7.
- [3] **Denis Tudor**, Mario Paolone, "Operational-driven optimal-design of a hyperloop system," in *Transportation Engineering*, Volume 5, 2021, 100079, ISSN 2666-691X.
- [4] **Denis Tudor**, Mario Paolone, Tony Govoni, Malicia Leipold, "Design of a Hyperloop System MockUp," in *IEEE International Conference on Intelligent Transportation Systems (ITSC)*, 2022, (accepted, but not yet published).

## Awards and Honors

Jan. 2016	Contest: First Prize for the "Best Design" at "SpaceX Hyperloop Pod Competition" - Non-Student Team	Texas
Jan. 2017	Contest: First Prize for "Innovation" at "SpaceX Hyperloop Pod Competition"	LA
Jun. 2017	Contest: "Valedictorian" at Politehnica University of Bucharest	Buc.
Jul. 2018	Contest: Third Prize for "Speed" at "SpaceX Hyperloop Pod Competition"	LA

## Volunteer Services

### IEEE Transactions on Transportation Electrification Journal

Peer Reviewer

Oct. 2019 - Present

### Transportation Engineering Journal

Peer Review

Oct. 2021 - Present

### Rail Transport Planning and Management Journal

Peer Review

Jun.2022 - Present